DESIGN, ANALYSIS AND VALIDATION OF A TWIST REFLECTOR MONOPULSE ANTENNA SYSTEM WITH RADOME

Tamara Louise Sheret

February 2017

Submitted in partial fulfillment of the requirements
of the Degree of Doctor of Philosophy.

Queen Mary University of London

STATEMENT OF ORIGINALITY

I, Tamara Louise Sheret, confirm that the research included within this thesis is my own work or that where it has been carried out in collaboration with, or supported by others, that this is duly acknowledged below and my contribution indicated. Previously published material is also acknowledged below.

I attest that I have exercised reasonable care to ensure that the work is original, and does not to the best of my knowledge break any UK law, infringe any third partys copyright or other Intellectual Property Right, or contain any confidential material.

I accept that the College has the right to use plagiarism detection software to check the electronic version of the thesis.

I confirm that this thesis has not been previously submitted for the award of a degree by this or any other university.

The copyright of this thesis rests with the author and no quotation from it or information derived from it may be published without the prior written consent of the author.

Signature: Tamara Sheret

Date: 01/02/2017

Details of collaboration and publications:

I performed all scientific tasks, data collection, analysis and writing. Details of publications from the work contained in this thesis can be found in Table 8-A. Co-authors provided adice during meetings and comment on manuscripts.

.

ABSTRACT

This thesis presents a new approach to the hardware test environment for a twist reflector monopulse antenna system with a radome extending current measurement practice. New research is presented on the optimisation of the design of a twist reflector monopulse antenna system with a radome, significantly improving the design and the design process.

A unique extension to current measurement practice, for single channel antennas, is presented to determine the best practice method on phase stable measurements of a multi-channel antenna on a moving positioner. A novel axis transform for a 3 axis positioner system located within an anechoic chamber is derived. It allows for true performance measurement of a twist reflector antenna with a radome. This progresses the field of antenna measurement as, uniquely, this axis transform allows the aberration caused by the antenna radome to be measured and included.

Design improvements have been made on polarisation selective grids, the matched thickness of the radome and a new software method that removes the need for a comparator and increases the robustness of the antenna system. Polarisation selective grids, constructed from a set of parallel conductors, have a wide range of uses in antenna systems. This thesis shows that the depth of a copper grid line can be reduced to 15 μm and still provide better than -25 dB cross-polar isolation. This is contrary to current understanding at 30 times the skin depth. A new combined approach to radome thickness optimisation is presented that reduces the time taken to calculate the optimal thickness by over 3 orders of magnitude and the computer memory by over 2 orders of magnitude without compromising accuracy. The use of a digital comparator is described and leads to a novel method to compensate for a failed feed element, verified in both simulation and anechoic chamber measurements.

ACKNOWLEDGEMENTS

Thanks to everyone who has supported me, in whatever way, in the long journey to finishing a PhD. All my work collegues, my dancing and gym buddies, my university and school friends - you know who you are. I would like to mention the support of Anritsu for the never ending supply of Stanley bears in a range of exciting outfits.

I would particularly like to extend my deepest gratitude to Clive, Ben and Bernard. Without your help and support this thesis would not exist. An industrial part time PhD is not a sensible thing to do, but you have made it an enjoyable and fulfilling experience.

To Ian, and my family for everything.

LIST OF CONTENTS

LIST OF FIGURES

LIST OF TABLES

LIST OF ABBREVIATIONS

’	Rotated axis frame
2D	2-Dimensional
2DRTM	2D Ray Tracing MATLAB Model
A	Monopulse Channel A
α	Angle (^{o})
Aberration Angles	Movement in the Commanded Beam Frame (^{o})
AC	Anechoic Chamber
Acceleration	Acceleration of an axis of the positioner (ms^{-2})
Angular Error	Angular error on position of source (^{o})
A_P	Physical area of antenna (m^2)
AT	Axis Transform
AUT	Antenna Under Test
AUT_G	Gain of AUT (dB)
$AUT1_G$	Gain of AUT 1 (dB)
$AUT2_G$	Gain of AUT 2 (dB)
$AUT3_G$	Gain of AUT 3 (dB)
AUT_M	Measured gain of AUT (dB)
$AUT1to2_M$	Measured gain of AUT 1 to 2 (dB)
$AUT1to3_M$	Measured gain of AUT 1 to 3 (dB)
$AUT2to3_M$	Measured gain of AUT 2 to 3 (dB)
AZ	Azimuth (^{o})
B	Commanded Beam Frame
B	Monopulse Channel B
BToT	Commanded Beam frame to the True Beam frame
C	Chamber Beam Frame
C	Monopulse Channel C
C	Von Kármán scaling factor. $\mathbf{C} = 0$ gives the LD-Haack shape

CPU	Computer Processing Unit
CToS	Chamber Beam frame to System Body Frame
d	Diameter of antenna (m)
D	Monopulse Channel D
δ	Skin Depth (m)
Δ	Difference (dB)
ΔAZ	Difference Azimuth (dB)
$\Delta AZ/\Sigma$	Difference Azimuth Divided by Sum
ΔEL	Difference Elevation (dB)
$\Delta EL/\Sigma$	Difference Elevation Divided by Sum
Δ_S	Difference scaled (dB)
Δ_{US}	Difference un-scaled (dB)
δf	Change in focal length (m)
$\Delta\phi$	Phase Change (^{o})
Δ/Σ	Difference Divided by Sum
δy	Allowable change in height of parabolic reflector (m)
Distance Travelled	Angular distance travelled by an axis on the positioner (^{o})
E	Electric Field (Vm^{-1})
EL	Elevation (^{o})
EM	Electromagnetic
EMR	Electromagnetic Radiation
ϵ_r	Relative Permittivity or Dielectric Constant
Euler 321 Angles	Orientation of the position within the reference frame for an AT
f	Frequency (Hz)
f	Focal Length (m)
FSL	Free Space Loss (dB)
G	Gain (dB)
GL	Metallic Grid Line on a PSG
GLD	Depth of grid line on a PSG (m)
GLG	Gap between grid lines on a PSG (m)

GLP	Pitch of grid line on a PSG (m)
GLW	Width of grid line on a PSG (m)
H	Magnetic Field (Am^{-1})
Height of Unit Cell	Height of unit cell model for reflector definition (m)
$_i$	Incident Ray
I	Unit vector of incident ray's direction
I	Current (A)
Image Rotation	Image Rotation caused by the mirror in a TRMAS
Ku	K - under microwave band (12 to 18 GHz)
L	Length of radome (m)
λ	Wavelength (m)
L_{AUT}	Additional hardware losses for the AUT (dB)
λ_m	Wavelength in material (m)
λ_o	Wavelength in free space(m)
L_P	Perpendicular length of a pyramidal horn (m)
L_R	Measured Loss through the AC (dB)
L_{RX}	Loss through receive cables (dB)
L_S	Slant length of a pyramidal horn (m)
L_{SGH}	Additional hardware losses for the SGH (dB)
L_{TX}	Loss through transmit cables (dB)
$\mathbf{M_{ij}}$	Matrix element notation, $_\mathbf{i}$ row number, $_\mathbf{j}$ column number
μ_o	Permeability of free space
μ_r	Relative permeability
n	Integer
n	Refractive Index
N	Surface normal unit vector
NMT	Nominal matched Thickness (m)
η_a	Aperture efficiency (%)
P	Power (W)
ϕ	Rotation around the x axis (^{o})

ψ	Rotation around the z axis (^{o})
Polarisation Loss Factor	Loss of Gain due to depolarisation (dB)
Positioner Angles	Angle the positioner is pointing to (^{o})
P_S	Power received by SGH (W)
PSG	Polarisation Selective Grid
P_T	Power received by AUT (W)
Q	Cross Difference (dB)
$_r$	Refracted ray
R	Radius of radome (m)
R	Resistance (Ω)
RAM	Radar Absorbent Material
RD	Reflector depth (m)
RF	Radio Frequency
R_L	Resistance Load (Ω)
RL	Range Length (m)
RMS	Root Mean Square
RMT	Radome Matched Thickness (m)
R_S	Resistance Source (Ω)
S	System Body Beam Frame
σ	Conductivity (Sm^{-1})
Σ	Sum (dB)
S_{11}	Scattering parameter input return loss (dB)
S_{21}	Scattering parameter transmission (dB)
SDC	Software defined Combination
SGH	Standard Gain Horn
SGH1	Standard Gain Horn 1
SGH2	Standard Gain Horn 2
SGH3	Standard Gain Horn 3
SGH_C	Calibrated gain of SGH (dB)
SGH_M	Measured gain of SGH (dB)

SToB	System Body frame to Commanded beam frame
STTE	Special To Type measurement Equipment
Σ_S	Sum Scaled (dB)
Σ_{US}	Sum Un-Scaled (dB)
System Angles	Movement in the System Body Beam frame (^{o})
^{T}	Transpose
T	True Beam Frame
θ	Rotation around the y axis (^{o})
Target Angles	Movement in the True Beam frame (^{o})
$\tan\delta$	Loss Tangent
Time Taken	Time taken for an axis on the positioner to move (seconds)
Tracking Slope	The gradient of the Δ/Σ as a function of angle (V V^{-1} $^{o-1}$)
TRMAS	Twist Reflector Monopulse Antenna System
TToC	True Beam frame to the Chamber Beam frame
θ_v	Angle in a Von K*árm*án (radians)
Unit Cell Width	Unit cell width for PSG definition (m)
V	Voltage (V)
$\mathbf{v_C}$	Column vector in C frame
velocity	Speed in a given direction on the positioner (ms^{-1})
$\mathbf{v_S}$	Column vector in the S frame
V_S	Voltage source (V)
$\mathbf{v_T}$	Column vector in the T frame
VNA	Vector Network Analyser
x	Distance along the length of radome (m)
x	x axis
y	y axis
y_{max}	Maximum height deviation allowed on parabolic reflector (m)
y_{min}	Minimum height deviation allowed on parabolic reflector (m)
y Value of First Grid Line	y value of first grid line on a PSG (m)
z	z axis

Chapter 1

INTRODUCTION

The focus of this thesis is to present research on the improved hardware test of a Twist Reflector Monopulse Antenna System (TRMAS) and the optimised design of constituent parts. The improved hardware test procedure for a TRMAS, when established in this thesis, will be used to aid the optimisation of the design of a TRMAS with radome. The optimisation of the TRMAS will be completed through a combination of full field Electromagnetic (EM) simulation, mathematical simulation and hardware test.

This thesis is split into two main sections which allows research and development into the design and test of a TRMAS.

- Firstly the improved hardware test of a TRMAS will be investigated. This work is of importance to further the field of antenna test. Traditional test facilities typically integrate an antenna with one output signal. When multiple signals are used additional procedures have to be followed for accurate testing. The improved hardware test findings in the first section are used to complete the hardware testing in the second section of the design optimisation.

- Secondly the design improvement of a TRMAS will be investigated. To further the field of TRMAS design three components, which are not well represented in the literature, have been selected for research: the Polarisation Selective Grid (PSG), the radome and the compensation for a failed feed element in a digital comparator.

1.1 OUTLINE STRUCTURE OF THESIS

Chapter 2 presents a critical review of the literature that is of importance to the work in this thesis.

1.1.1 IMPROVED HARDWARE TEST OF A TRMAS

- Chapter 3 develops the test methodology for measuring a TRMAS in an Anechoic Chamber (AC).
- Chapter 4 develops an Axis Transform (AT) suitable to measure a TRMAS on a multi-axis positioner.

1.1.2 DESIGN IMPROVEMENT OF A TRMAS

- Chapter 5 develops an improved design for a PSG for minimum cross-polar isolation loss.
- Chapter 6 develops an improved design and design process of a radome for minimum transmission loss.
- Chapter 7 develops the software combination for channels of a TRMAS without the use for a comparator and with the compensation for a failed feed element.

1.2 RESEARCH OBJECTIVES

My research objectives are:

- To define an accurate AC chamber calibration procedure for the measurement of a TRMAS.
- To define a measurement technique to perform phase stable measurements of a TRMAS.

- To derive an AT to accurately measure a TRMAS on a 3 axis positioner.
- To design a functioning PSG at the -25 dB cross-polar isolation level to be used in a TRMAS.
- To improve the design process to calculate the optimised thickness of a radome for minimum transmission loss to be used in a TRMAS.
- To successfully recover the Sum (Σ) and Difference (Δ) signals from a TRMAS if one feed element has failed.

This introduction will now go on to discuss reflector antenna systems, specifically concentrating on a TRMAS with a radome, and their current test procedures.

1.3 REFLECTOR ANTENNA SYSTEMS

A reflector antenna is an antenna where there are Radio Frequency (RF) reflective surfaces that reflect the Electromagnetic Radiation (EMR) [1]. There are many types of reflector antennas: Front fed, Offset feed, Cassegrain, Gregorian and Twist Reflector. The main advantage for using a reflector antenna system is the feed and electronics can be located behind the dish. Cassegrain and Twist Reflector antenna systems are discussed below.

1.3.1 CASSEGRAIN ANTENNAS

A true Cassegrain reflector antenna [2], as shown in Fig. 1.1, has a feed horn located at the vertex of the parabola and a hyperbolic sub-reflector at the focal point [3] [4]. A Cassegrain reflector antenna is a popular choice for airborne and ground based antenna systems [5].

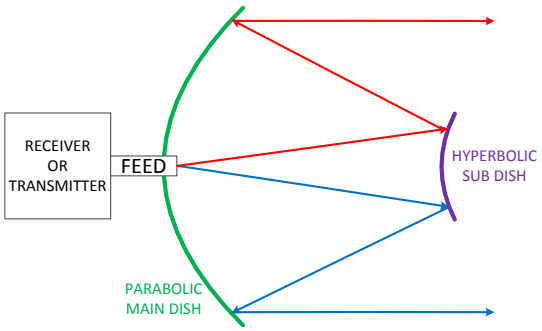

Figure 1.1: Structure of a Cassegrain antenna.

Cassegrain antennas have many advantages over other reflector antenna systems. The sub-reflector shaping gives amplitude and phase control of the aperture illumination, spill over from the sub-reflector is directed out into space and long transmission lines to the feed are eliminated. Cassegrain antennas have limited beam scanning ability without incurring significant beam deformation. It is possible to scan the whole Cassegrain, but mechanically this can be challenging and reduces the aperture size of the antenna. These limitations have led to development of this traditional Cassegrain system into a twist Cassegrain system where the hyperbolic secondary mirror is replaced by a PSG.

A PSG is a set of parallel metal Grid Lines (GL) which allow the transmission or the reflection of RF radiation depending on the polarisation. When the polarisation of the Electric Field (**E**) field is parallel to the GL the **E** field induces a current in the GL and the grid is seen as an RF mirror. When the polarisation of the **E** field is perpendicular to the GL no current is induced and the EMR passes through the grid. This thesis will investigate the formation and structure of a PSG.

This design concept of a twist Cassegrain can be further simplified by altering the configuration and shape of the two reflecting surfaces into a twist reflector antenna, which improves the gain, efficiency and beam.

1.3.2 TWIST REFLECTOR ANTENNAS

A polarisation selective scanning twist reflector antenna is a way of reducing aperture blockage in systems that operate in only one linear polarisation [2] [6]. The introduction

of a scanning flat plate increases the angular width of radiation that can be accepted by the antenna. A Twist reflector [7] [8] is shown in Fig. 1.2 and has:

- A paraboloid PSG. Depending on the polarisation of the incident radiation the parabolic reflector either allows transmission or reflection [9].
- A twist reflector mirror which rotates the polarisation of the incident radiation by 90^o upon reflection [10] [11] [12].
- The twist reflector mirror is articulated allowing the beam to be scanned.
- A monopulse feed horn.

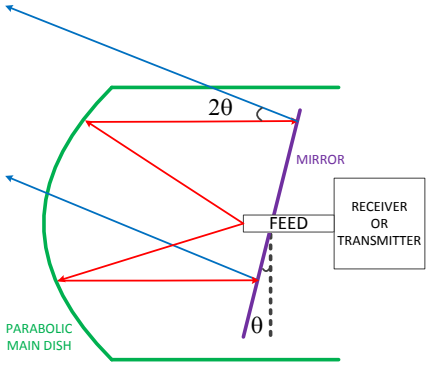

Figure 1.2: Structure of a Twist Reflector Antenna System.

Twist reflector antennas have several advantages over traditional Cassegrain systems as they have good beam scanning capabilities with limited impact on beam patterns and are compact designs which maximise aperture usage. They can be found in a wide range of applications, for example in ground based, airborne, space [13] and unfurlable satellite communication antennas [14]. Twist reflector antennas can have either a single or a multiple channel feed.

1.4 MONOPULSE FEED HORN ANTENNA

A feed horn is an antenna which transmits the EM signal between the transmitter or receiver and the reflector. It is polarisation selective in a TRMAS. A feed horn can work in both transmit and receive modes as passive antennas are reciprocal. The following

discussion is given in the transmit sense, but is equally applicable for receive.

A monopulse antenna is an antenna array which is symmetrical about boresight, Fig. 1.3. The feed horn is constructed from four feed elements: A, B, C, D [15]. Typically, for an amplitude-comparison monopulse antenna system [16], there is a focusing element in front of the feed horn at the focal length. In this thesis the focussing element is a parabolic reflector, but a lens can also be used [17], Fig. 1.4.

Overlapping beams are produced by the feed elements from which the Σ and Δ signals can be calculated in Azimuth (AZ) and Elevation (EL), as shown in Fig. 1.5, and analysed by the use of a comparator attached to the feed horn. Σ maximises the signal at the centre of the antenna beam. Δ produces a null at the centre of the antenna beam and has an amplitude related to the angular distance between the object and boresight in AZ (ΔAZ) and EL (ΔEL), where there is a sign inversion with respect to the Σ phase. A difference at 45^o to the AZ and EL axes can be created (Q), which may be used to help detect jamming signals or improve angular estimates, but is not of significant use and is typically terminated and unused in waveguide based comparator systems [18].

Advantages of monopulse systems over a single antenna include: accurate AZ and EL target position estimation in one transmission; and the ability to detect jamming which make it a very popular choice for tracking radar. Other uses of monopulse antennas include reflector antenna systems, satellite communications, radio astronomy and sonar [18].

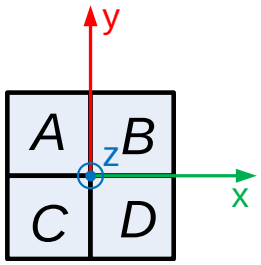

Figure 1.3: Feed element nomenclature of the antenna looking into the feed horn cluster.

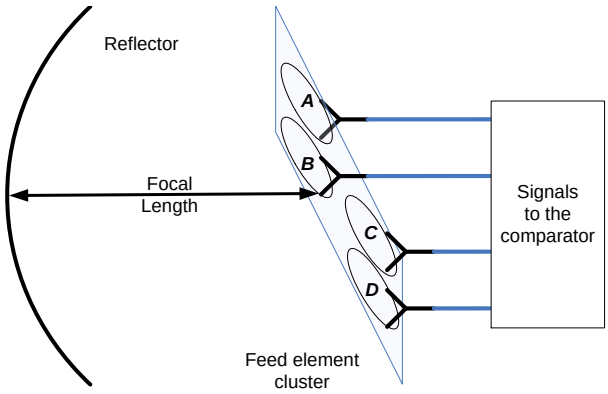

Figure 1.4: Feed element cluster and relationship to the reflector.

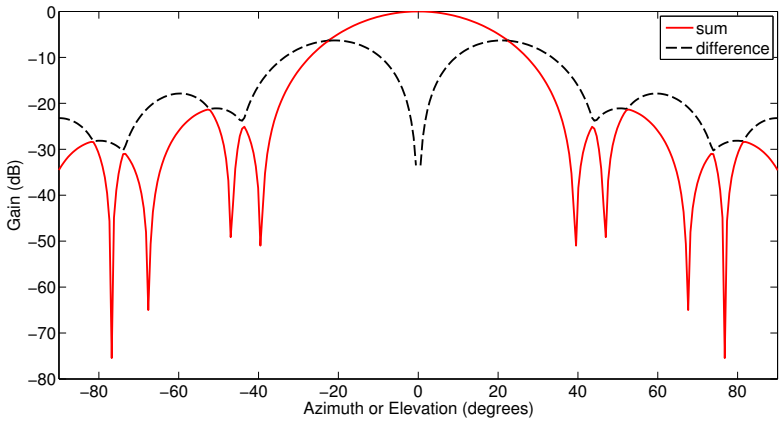

Figure 1.5: Simulated Σ and Δ radiation patterns for a monopulse antenna.

1.5 HARDWARE COMPARATOR

Traditionally tracking monopulse radars use a waveguide based RF network, known as a comparator [19], connected to the feed elements [20]. This comparator forms linear combinations of the signals received by each feed element, to produce Σ and Δ signals [21].

A comparator is a collection of dividers, combiners and waveguide; the exact choice of each item is dependent on the requirements of the system [22]. An example is shown in Fig. 1.6. It is important that no phase or amplitude errors are introduced by the comparator, so the four ports need to be highly symmetrical and the phase shift introduced by the symmetry requirements taken into account.

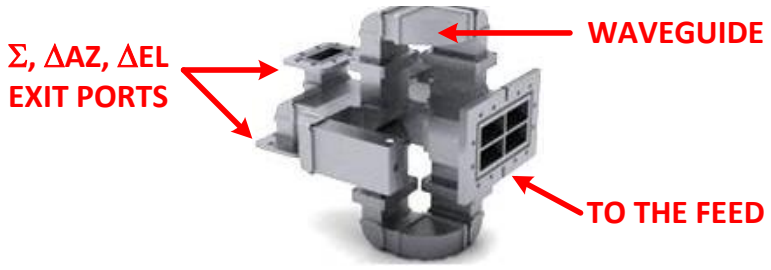

Figure 1.6: Jitai Tech hardware monopulse waveguide comparator (www.jittc.com).

Comparators have the advantage of being passive, reciprocal and stable, however they are spatially large, expensive to manufacture, have high mass and introduce signal loss to the system. In airborne radar the penalty paid for the addition of loss and a large mass and space budget is often very high. This thesis will verify a method by which the comparator can be removed and replaced by a digital comparator which is further developed to offer recovery of the system if a channel fails.

1.6 RADOME

Radomes are structures that cover an antenna providing environmental protection whilst by design have limited effect on the performance of the antenna. The external profile, robustness and material of the radome vary greatly depending on its purpose. The introduction of a radome to an antenna system will increase transmission and receive losses, distort the pattern and polarisation of the antenna pattern and cause errors in boresight measurements [23].

1.6.1 PURPOSE AND REQUIREMENTS OF A RADOME

For an antenna to successfully operate environmental protection, by means of a radome, is often required. This radome will cause a refraction of the EM signal being detected by the antenna, resulting in an apparent movement of the source, aberration [24]. Often, due to the operational requirements of the system, the radome cannot be a hemisphere and has to be an aerodynamic shape such as a Von Kármán, meaning the refraction caused

by the radome changes as a function of scan angle of the antenna. This aberration has to be compensated for during measurement of the target [25].

1.6.2 TYPICAL MATERIAL AND SHAPE OF RADOMES

The material choice is a compromise between RF and mechanical performance. The radome has to be as transparent as posible to RF, but strong enough to cope with the environmental conditions that the antenna will be exposed to. As radomes are often mounted in aerospace systems they have to be able to withstand the launch stresses and the environmental heating. Ceramic and composite materials are common choices for radomes to perform in aerospace systems.

External profiles of radomes range from hemispherical and geodesic through ogive and conical to very pointed Von K*árm*án profiles depending on the purpose of the antenna. If the antenna is land based then a more RF performance friendly hemisphere can be used. However, if the antenna system is for aerospace purposes then the radome will become more pointed to aid aerodynamics [26].

This thesis will look at improving the design process of a single walled aerospace radome to calculate the matched thickness for the radome which gives minimal transmission loss.

1.7 HARDWARE ASSESSMENT OF A TRMAS

There are many different types of test ranges used to measure the performance of an Antenna Under Test (AUT): open air range, slant range, compact range, AC, semi-AC and near-field measurement systems [27]. Measurements taken on test ranges can then be compared to those from EM simulation to advance the design tools and the AUT being characterised. Test ranges have to be carefully designed to meet the requirement of the AUT and the measurement programme.

Indoor RF test facilities are designed to mimic an outdoor range. Being indoors means the test procedure is simpler as you do not have to deal with working outdoors and the health and safety implications of working with RF radiation are more easily addressed. However,

the additional challenge to design a range that mimics the outdoors is introduced.

1.7.1 ANECHOIC CHAMBERS

ACs are rooms designed to absorb the reflections of EMR [28] and to minimise interfering energy disturbances from external spurious sources [29]. Such ACs are used to measure the performance of the AUT, in particular gain and pattern characteristics.

Typically, the AC wall construction is a Faraday cage which prevents external signals entering the AC, interfering with measurements. It also prevents test signals escaping from the AC, which may interfere with external devices and be a potential health risk [30]. The interior of an AC is lined with Radar-Absorbent Material (RAM) [31] with construction and lay-out to provide RF signal absorption across the required frequency (f (Hz)) band and to produce the quiet zone. The quiet zone is the volume in which the AUT is placed and where the EM reflections are at a minimum. The reflectivity of the RAM is dependent on angle of incidence of the radiation. Therefore the RAM reflectivity needs to be considered when designing the RAM lay out in the AC as this creates quiet zone. The measurement system requires a transmit signal source of RF energy in the correct frequency range and a receive system that is capable of measuring the signal received by the AUT, Vector Network Analyser (VNA).

If a low power measurement is to be taken it is possible to use the VNA as the transmit power source and the receive measurement system. The RF transmit signal produced in the VNA can be routed via co-axial cables to a transmit Standard Gain Horn (SGH). The signal is then received by the AUT and the receive signal routed to the VNA for measurement via co-axial cables. If a higher power source is needed, additional amplifiers may be required in the RF path before the transmit SGH. Alternatively, the transmit power source could be changed to a solid state power amplifier or travelling-wave tube with additional hardware to ensure phase stabilisation between the transmit power source and the receiving VNA.

1.7.2 USE OF POSITIONING SYSTEMS

A positioning system is required in the AC to hold and to move the AUT with respect to the incoming plane wave and hence determine the antennas spatial radiation pattern. The positioning system has the required number of degrees-of-freedom to complete the desired measurements on the AUT [32]. These positioning systems are manufactured from metal and therefore have to be covered in RAM to avoid spurious reflections. There are many possible designs of positioner systems which is dependent on the AUT being measured.

Cables have to be run from the positioning system to the VNA. Consequently, the cables will move as the positioner moves. It is well known that if an RF cable is moved, the magnitude and phase of the measurement will be liable to change.

The main uses of a three axis positioner in an AC is to produce antenna patterns, an AZ and an EL cut to be completed and the gain at each position measured. These cuts need to be taken in the True Beam Frame (T) to ensure they are true AZ and EL, so the step size is consistent across the sweep and that they do not suffer depolarisation. Therefore an AT is required for the positioning system.

Rather than taking the antenna pattern as a series of positions it is possible to move the positioner in a sweep, taking data as the positioner is moving. This will require the AT to allow the movement of the positioner to occur whilst keeping the **E** vector of the AUT upright. If the AT is not used the measurements will suffer significant depolarisation.

1.7.3 AXIS TRANSFORM

To move in the T frame of an AUT, a series of AT are required to transform the movement of the positioner from the Chamber Beam frame (C) to the T frame. When this AT is included, the positioner can be programmed to move in a manner that describes a linear cut in the T frame of the AUT co-ordinate frame and true AZ and EL cuts can be taken. If an AT is not used the AUT prescribes a great circle, therefore the AUT cut will not have equal sized steps and will suffer significant linear depolarisation during the plot as the **E** vector of the AUT will rotate with respect to the transmit horn. This leads to incorrect

antenna patterns and gain profiles being measured.

1.8 KEY FINDINGS OF THIS THESIS

The key findings of this thesis are summarised below:

- Definition of an accurate anechoic chamber calibration procedure for measurement of a twist reflector monopulse antenna system.
- Definition of a measurement technique to perform phase stable measurements of a twist reflector monopulse antenna system.
- Derivation, simulation and hardware confirmation of an axis transform to measure a twist reflector monopulse antenna system and radome on a 3 axis positioner.
- Through theoretical modelling and experimental testing the grid line depth of a polarisation selection grid is required to be at minimum 30 times the skin depth for the polarisation selection grid to function at the -25 dB level.
- Derivation of a new method to calculate the optimised thickness of a radome for minimum transmission loss reducing time overheads by 3 orders of magnitude.
- Successful recovery of sum and difference patterns if one feed element of the twist reflector monopulse antenna system fails.

1.9 SUMMARY OF THESIS

Chapter 2 discusses existing research in the areas of interest and explains how the research presented in the following chapters extends this existing knowledge.

The technical work in this thesis is split into two sections: the hardware test set up and methodology for a TRMAS; the design improvement of a TRMAS with radome for performance and robustness.

Two chapters discuss the hardware test set up and methodology to accurately test a TRMAS. Chapter 3 develops the best practice for use of an AC to measure a TRMAS. It investigates and experimentally proves the optimal procedure to conduct phase stable measurements on a moving positioner. Chapter 4 derives and proves with simulation and hardware test an AT that allows correct testing of a TRMAS.

Three chapters discuss the design improvement of a TRMAS with a radome for performance and robustness by the optimisation of component parts. Chapter 5 defines the optimal grid and reflector construction for minimising the isolation performance of a PSG by EM simulation and hardware test. Chapter 6 defines the optimal thickness of a radome for minimised transmission loss by mathematical and EM simulation with hardware test. Chapter 7 replaces the use of a hardware comparator with the addition of the signals in software, tested by mathematical simulation and hardware test. It then derives and defines a process to form the monopulse Σ and Δ signals if one of the channels fails with mathematical simulation and hardware testing.

Chapter 8 details the main contributions, conclusions and further work.

This thesis is approved by MBDA's Technical Writing Scheme submission number TWS512. The individual chapter contents and published papers are approved by MBDA's Technical Writing Scheme submission numbers TWS424, TWS461, TWS468, TWS471, TWS494 and TWS513.

Chapter 2

CRITICAL LITERATURE REVIEW

This chapter presents a critical review of the literature that is of importance to the work in this thesis. The technical work in this thesis is split into two overall themes: the hardware test set up and methodology for the test of a TRMAS, and the design improvement of a TRMAS with radome for performance and robustness.

2.1 HARDWARE TEST SET UP AND METHODOLOGY FOR A TRMAS

This section describes the current research and practices for measuring a TRMAS in an AC. In Chapter 3 the test methodology will be developed and extend to take phase stable measurements with a multi-channel antenna system as references could not be found to cover this knowledge. References that clearly describe how to calculate an AT for a multi-axis positioner could not be found. Therefore Chapter 4 addresses this gap in the published literature, with a derivation and test of an AT for a TRMAS. These sections will be discussed in more detail.

2.1.1 ANECHOIC CHAMBERS

2.1.1.1 PROS AND CONS OF USING ANECHOIC CHAMBERS

ACs are used for convenience over open air ranges. Taking measurements in an AC is logistically easier than an outdoor range as the site is smaller, contained within an existing building with amenities and its functionality is independent of weather. In addition it is easier to measure the AUTs phase with respect to the reference signal as the distances

involved are smaller. The AC also helps to minimise the health and safety impact of working with high power RF radiation under the Occupational Exposure to Non-Ionizing Radiation guidelines from the National Radiological Protection Board [30] as transmissions are contained.

However, because ACs simulate an outdoor range and can only minimise spurious RF reflections, the performance of the AC has to be properly assessed [33]. Range effects, such as spurious reflections, can be identified by measuring the AUT at different rotational orientations, antenna effects are reflection features in the pattern that rotate with the AUT, range effects stay in the same location.

There are alternatives to ACs which can be used to measure AUTs [27]. To reduce construction costs it is possible to use a semi-AC, where not all of the walls of the chamber have RAM installed [34], however the issues raised are still applicable for this kind of chamber. Open air ranges, which minimise spurious reflections, can be used but these are large, expensive and difficult to work on. Slant ranges [35] can be used, but tend to also be outside and suffer the same drawbacks as open air ranges. Rather than using a simple transmit and receive AC, a compact range [35] could be used which helps to minimise the size of the AC. However, this is a more complicated construction and has detrimental effects on cross polar measurements. If power measurements alone are required, a 'RAM dump' could be used, which is a RAM lined metal box which absorbs incident RF radiation. For certain antennas it is possible to measure the near field of an antenna and transpose this into the far field [36]. This is a complicated process and measurements need to be taken with great care. Devices such as the EMSCAN RFxpert can make this process more robust to get real-time near-field measurements for electrically small antennas [37]. Electrically large antennas can be measured in near field systems using either planar, cylindrical or sperical nearfield scanning, for example NSI-MI.

2.1.1.2 CALIBRATION OF AN ANECHOIC CHAMBER

To measure an AUT, the path losses and phase changes in the measurement system must be determined and their effects calibrated out. To measure this calibration in a far-field AC,

a SGH is measured on the positioner in the AC. These results can be used to measure the loss and the phase change through the AC and therefore provide input for AC calibration.

A TRMAS is an AUT with more than one input and output channel. It is important that each channel of the AUT is measured without a magnitude or phase imbalance being introduced between channels due to differences or movement in measurement hardware. The acceptable level of error between measurements in the magnitude and phase will be defined by the requirements of the individual AUT. Traditional AC calibration methods are designed to cope with only one channel, therefore a calibration method needs to be defined for a multi-channel AUT. This thesis presents the correct procedure to calibrate a multi-channel AUT [38]. For a multi-channel AUT the absolute magnitude and relative phase of each channel of the TRMAS has to be measured. Therefore the magnitude and phase of each channel's total RF path needs to be measured for the calibration.

When measuring a single channel AUT there is a single output from the AUT, routed via a co-axial cable, to a VNA for measurement. There is no opportunity for magnitude and phase errors to occur between measurements as only a single measurement is taken. However, when measuring a TRMAS the necessity arises for multiple co-axial cables and or a multiplexer to be introduced for measurement purposes. These differences in the RF paths introduce additional sources of error. Magnitude and phase errors will be introduced with different cables being used; during movement of the positioner when the cables will move independently and different hardware in the RF path. In addition the channels cannot be measured simultaneously and this allows atmospheric changes, measurement errors and cable movement to introduce errors between the measurements. The errors of the chosen system and measurement procedure need to be investigated and understood so they can be taken into account. This thesis defines the correct procedure to carry out phase stable measurements in an AC [39].

2.1.2 AXIS TRANSFORM

A three-dimensional co-ordinate frame uses 3 mutually orthogonal planes where a unique position is defined by a signed distance from the origin on each of the planes. An AT is

a directional cosine matrix that describes a rotation, defined by the cosine of the angle between the two vectors, between different co-ordinate frames. These can be multiplied together to give a single mathematical operation that describes changes between multiple axes sets [40].

2.1.2.1 MEASUREMENT ERROR CAUSED BY THE RADOME

The radome covering a TRMAS will cause several effects on the antenna. There will be an increase in reflected energy and a degredation in antenna patterns [41]. Of most interest to this thesis there is also a refraction of the EM signal being detected by the antenna, resulting in an apparent movement of the source. This apparent movement of the source caused by the aberration effects of the radome has to be compensated for during measurement [25]. This thesis shows the derivation of an AT for use on a 3 axis positioner and how compensation for the aberration of the radome can be included in the AT during the measurement phase [32]. *Euler 321 Angles* will be used to describe the orientation of the position within the reference frame [42] [43].

2.2 DESIGN IMPROVEMENT OF A TRMAS

This section describes the current researches and practices for the design of components of a TRMAS. Firstly the current understanding of the GL structure on a reflector will be discussed. Chapter 5 challenges the current understanding and with simulation and hardware test develops the new requirement to manufacture a working PSG. Secondly, the current research on methods to determine the matched thickness of a radome is presented. Chapter 6 discusses how these methods are improved by reducing the required time and computational power to calculate the radome thickness, results are verified by hardware measurements. Finally, the current use of a comparator is shown. Chapter 7 develops this into a software combination of the channels, thus allowing removal of the comparator. It goes onto develop algorithms to allow the TRMAS to continue to function after the failure of a feed element.

2.2.1 REFLECTOR

2.2.1.1 FACTORS AFFECTING A POLARISATION SELECTIVE GRID

Regardless of the specific use, PSGs have been traditionally manufactured with metal wire tracks, usually copper, on a dielectric substrate [44]. Typically, grids have a mark space ratio of 1:1, so 50 % of the surface of the grid is covered in metal. The spacing between the GLs has to be small relative to the wavelength of EM radiation in question for plane polarised waves that are parallel to the GLs to reflect [45]. Suitable GLs can now be manufactured with metal deposition and photolithography masking techniques [46], the Grid Line Depth (GLD) is now a parameter that can be investigated as it is possible to manufacture with a well-controlled thickness. This has in turn allowed a change in potential substrate materials and thicknesses.

2.2.1.2 USES OF POLARISATION SELECTIVE GRIDS

PSGs are used in antenna systems for many different applications. For example: inverse Cassegrain antennas where the PSG reflects or transmits linearly polarised radiation [47], twist reflector antennas where the PSG reflects or transmits linearly polarised radiation, polarisation selective antennas where the PSG is used to select the required polarisation [48] [49] or as a RF mirror [50]. This thesis will define new requirements to manufacture a working PSG using EM simulation and hardware test [9].

2.2.2 RADOME

This thesis presents an improved and novel process to define the optimised thickness of a radome. Traditional methods are time consuming and expensive often requiring iterations of hardware manufacture. They are based around complex equation approximations [51], complex ray tracing [52] [53] or electrically large EM simulations. The approach described in this thesis uses a 2D ray tracing method written in MATLAB [54] and a unit cell HFSS [55] simulation which optimises the thickness of the radome in a more time efficint manner and without compromising on accuracy.

Radomes can be made from a single electrically thin dielectric layer [56] or a sandwich, which has two dielectric layers with an alternative material between them as a core at its simplest [57]. This thesis will investigate a single layer radome as they are more commonly used in the aerospace industry due to operational requirements.

2.2.2.1 TRADITIONAL RADOME DESIGN TECHNIQUES

Radomes are carefully tuned to be a matched thickness for the frequency of EMR being used [58]. The matched thickness condition occurs when reflections are reduced and therefore least power is lost through the radome and there is least phase disturbance. The Nominal Matched Thickness (NMT) for a radome can be calculated from Equations (2.1) and (2.2) where λ_m is the wavelength in the material, λ_o is the wavelength in free space of the EMR and ϵ_r is the relative permittivity, and n is an integer. Equation (2.2) is independent of radome geometry and angle of incidence of the EMR. A form of this equation can be used, which is dependent on angle of incidence (α_i (^{o})), Equation (2.3) [59]. Before the common use of EM simulations to calculate the Radome Matched Thickness (RMT (m)) a radome would be manufactured over-thick by several mm, RF tested, the thickness reduced, RF tested and iterated until the optimal thickness was found. However this can be significantly improved on with EM simulation tools and other angles of antenna scan can be considered.

$$\lambda_m = \frac{\lambda_0}{\sqrt{\epsilon_r}} \tag{2.1}$$

$$NMT = \frac{n\ \lambda_m}{2} \tag{2.2}$$

$$NMT = \frac{n\ \lambda_0}{2\sqrt{\epsilon_r - \sin^2 \alpha_i}} \tag{2.3}$$

2.2.2.2 RAY TRACING METHODS

Ray tracing methods calculate the path of the RF wave through the radome system. It uses idealised narrow beams, rays, and calculates their propagation by known physical interactions at medium boundaries. They can be conducted as 2- or 3-Dimensional simulations. Snell's Law is used to define the refraction of a wave at a medium border, Equation (2.4),

where α is the angle and n is the refractive index. The subscript $_i$ denotes the incident ray data and $_r$ denotes the refracted ray data.

$$\frac{sin\alpha_i}{sin\alpha_r} = \frac{n_r}{n_i} \tag{2.4}$$

2.2.2.3 RADOME TEST TECHNIQUES

If the radome under test is a large structure that is made in several pieces it is possible to complete panel testing on each unit to measure the RF performance of the radome [60]. However, for monolithic radomes, the interaction of the radome with the antenna is greater and panel testing will therefore only be useful for understanding the RF performance of the radome material. AC testing of the antenna and radome system should be carried out to characterise the radome [61]. This will also allow a measurement of the aberration caused by the radome. A radome is polarisation sensitive, this thesis only considers single polarisation systems.

2.2.2.4 ELECTROMAGNETIC SIMULATION

EM simulation packages discretely solve Maxwell's equations for an EM wave interacting with a physical structure using finite element method or method of moments. There are commercially available EM simulation packages such as: HFSS, CST, FEKO and Momentum.

This thesis uses HFSS, which is a full wave EM simulation package. The radome structure can be optimised by creating a full EM model of the antenna and radome. However, these models are electrically very large and may be prohibitively difficult to run from both a time and computational requirement perspective. This thesis develops a method to calculate the thickness of a radome with minimal time and computational overheads [62].

2.2.3 COMPARATOR

Traditionally a comparator is used to create the Σ and Δ signals. However, particularly for airborne systems, the large mass and volume of a comparator is an issue. This section will look at the formation of the Σ and Δ signals without the use of a comparator. The removal of a waveguide comparator and use of 4 receivers for the individual channels has not been found in the open literature.

2.2.3.1 FORMATION OF Σ AND Δ WITHOUT A COMPARATOR

Equations (2.5), (2.6), (2.7) and (2.8) [59] show how the signals are combined by a comparator to produce Σ, ΔAZ, ΔEL and Q as shown in Fig. 2.1.

$$\Sigma = A + B + C + D \tag{2.5}$$

$$\Delta\ AZ = (A + C) - (B + D) \tag{2.6}$$

$$\Delta\ EL = (A + B) - (C + D) \tag{2.7}$$

$$Q = (A + D) - (B + C) \tag{2.8}$$

For angle tracking comparison the quantities $\Sigma/\Delta AZ$ and $\Sigma/\Delta EL$ lead to an estimate of the angle of the target within the beam according to Equation (2.9), where the angle is measured in ^{o}. The *Tracking Slope* (V V^{-1} $^{o-1}$) is the gradient of the Δ/Σ as a function of angle.

$$Target\ Angle = \frac{\frac{\Delta}{\Sigma}}{Tracking\ Slope} \tag{2.9}$$

To combine the 4 feed element signals in software, Equations (2.10), (2.11), (2.12) and (2.13) should be followed [18]. This thesis will derive a mathematical proof and hardware validation of these equations.

$$\Sigma = \frac{A + B + C + D}{2} \tag{2.10}$$

$$\Delta AZ = \frac{(A + C) - (B + D)}{2} \tag{2.11}$$

$$\Delta EL = \frac{(A + B) - (C + D)}{2} \tag{2.12}$$

$$Q = \frac{(A + D) - (B + C)}{2} \tag{2.13}$$

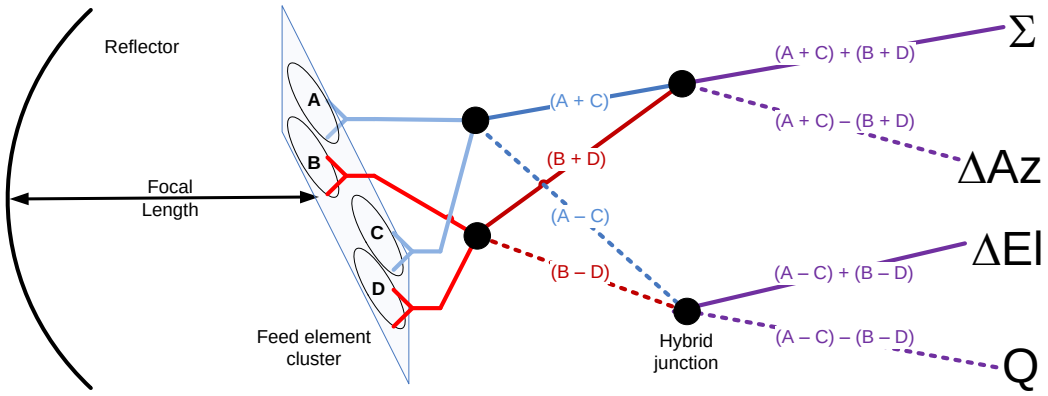

Figure 2.1: Four feed elements of a monopulse antenna combined within a comparator to produce Σ and Δ signals.

2.2.3.2 COMPENSATION FOR A FAILED FEED ELEMENT

If a feed element fails then a system with a traditional comparator is no longer able to function. There is no ability to compensate for this failure as the individual feed element data is not recorded.

This thesis presents simulation and hardware measurements to show how a failed feed element in a TRMAS can be compensated for [63]. Monopulse beams can be formed from large arrays containing up to many hundreds of elements with Σ and Δ signals being formed [64] [65] [66]. However, there are many differences between a four port monopulse feed plus reflector antenna and an array being used to produce monopulse signals. In a four port monopulse antenna beam steering and shaping [67], power synthesis and power taper are not implemented as they are not required. Work has been reported on the

compensation of failed elements in array monopulse systems, and includes improving the reliability of identification of failed elements [68] and compensation for the variability between elements [69]. When a small percentage of the antenna elements have failed the element weights can be corrected to compensate for the failed channels and recover the antenna pattern [65] [66]. However, these compensations are not applicable when 25 % of the array fails, as is the case with a monopulse antenna.

2.3 CHAPTER SUMMARY

This chapter has presented the published material relevant to the topics discussed in this thesis. The following chapters will build on and develop this existing knowledge and to fill identified gaps. A procedure for conducting phase stable measurements in an AC will be presented. An AT that gives accurate measurements for a TRMAS will be derived and tested in simulation and hardware. The GL structure of a PSG will be defined by simulation and proved by hardware test. The procedure to define the thickness of a radome will be developed to reduce the time and computational requirements. An algorithm to allow the continual function of a TRMAS with a failed channel will be developed and proved in simulation and hardware. The next chapter starts to investigate the hardware test set up and measurement methodology for a TRMAS, and details the procedure to take phase stable measurements in an AC.

Chapter 3

ANECHOIC CHAMBER PHASE STABLE MEASUREMENT TECHNOLOGY

3.1 INTRODUCTION

This chapter describes the hardware set-up in a full AC, which uses a VNA as the RF signal source and measurement unit. The work is novel because it describes the new procedure to measure multi-channel antenna systems. The process of measurement and calibration would also be applicable to other types of ranges.

This chapter also describes the optimal measurement procedure for accurate antenna measurement of multi-channel antennas. It assesses measurement procedures for phase stable measurement procedure.

To assess the performance of a multi-channel antenna system, the gain as a function of frequency and the Σ and Δ radiation patterns are measured. Simulated examples of these can be found in Fig. 1.5. To complete measurement of the Σ and Δ radiation patterns, movements are required on the positioning system. Therefore repeatability of measurements at the same position, after a movement of the positioner, is of paramount importance to reduce measurement errors.

3.2 ANECHOIC CHAMBER POSITIONING SYSTEM

Fig. 3.1 shows the schematic for the AC designed for AUT testing. The site is divided into three sections: transmit room; chamber; control room, all of which are screened rooms. The control room contains the control system for the range and is fully automated via PC

control with custom written MATLAB scripts. The VNA produces the transmitted signal, routed to the transmit horn via a co-axial cable, and analyses the received signal via a co-axial cable attached to the AUT. In the AC the positioner holds and orientates the AUT to measure plots in AZ and EL and produce full antenna patterns. The positioning system is a ROLL-over-EL-over-AZ three axis positioner [32]. The metal structure of the positioner is covered in RAM to prevent unwanted RF reflections. The transmit room allows the safe transmitting of the amplified VNA signal which can then be received by the AUT on the positioner without exposing users. It has a transmit positioner, which holds the transmit horn, and provides the main lighting for the chamber.

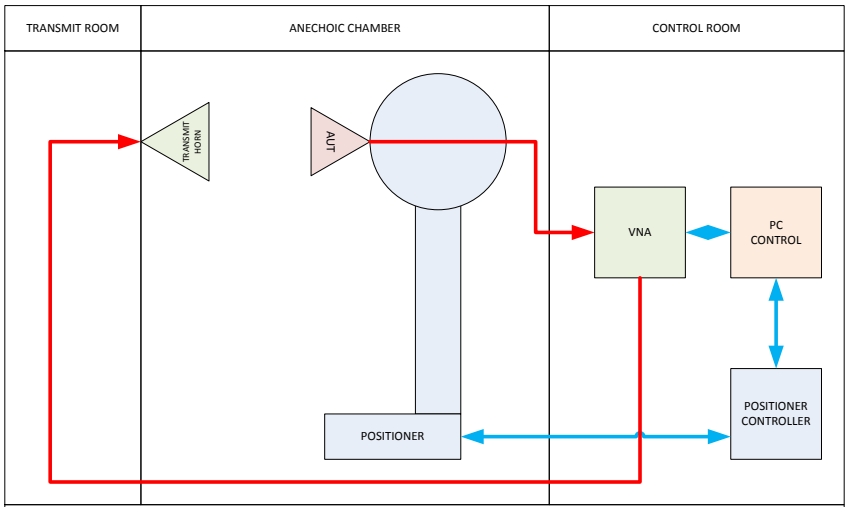

Figure 3.1: Schematic representation of AC used for antenna measurement.

Additional hardware has to be introduced to allow the measurement of multiple channels; this can be of the form of a multiplexer behind the TRMAS and a single channel VNA, or multiple cables coming from the back of the TRMAS into a multi-channel VNA. The multiplexer is formed by a series of loaded terminated RF switches and is PC controlled.

3.3 SIZE OF AN ANECHOIC CHAMBER

As an AC provides an environment to simulate free-space testing, the internal size of the chamber is of paramount importance. To ensure there is no undue interference from the

walls of the chamber, the distance to the structure forming the ceiling, floor and side walls from the AUT should be greater than the Rayleigh distance and the distance to the transmit horn should be greater than twice the Rayleigh distance [70]. The Rayleigh distance defines the far-field of an antenna based on its diameter (d (m)) and the wavelength of operation (λ (m)), Equation (3.1). If the AC used to measure the performance of an AUT is too small the measurements will be taken in the near-field and the results disturbed, thus the true far-field antenna performance is not measured. However, if the AC is too large there is no degradation to the measurement, apart from received signal levels due to increased path loss. But, there is an increase in manufacture costs, running costs and real estate requirements. In some measurement techniques it is possible to correct for near-field effects; these will not be discussed in this thesis.

$$Rayleigh\ Distance\ =\ \frac{2\ d^2}{\lambda} \tag{3.1}$$

For example, from Equation (3.1), an AUT with diameter 150 mm working at f = 15 GHz has a Rayleigh Distance of 2.37 m. Therefore the minimum chamber dimensions are 4.74 m wide by 4.74 m + distance from the front of the positioner to the back wall of the chamber by 4.74 m high. Measurements should be taken from the tips of the largest pyramidal RAM.

3.3.1 SIMULATIONS TO DETERMINE THE DISTANCE BETWEEN THE TRANSMIT HORN AND AN AUT IN AN AC

To illustrate the effect of measuring an AUT in a chamber of the incorrect dimensions a HFSS simulation was set up of a conical horn, as shown in Figs. 3.2 and 3.3 [27] [23] [8]. The simulation is split along two symmetry planes using perfect **E** and Magnetic Field (**H**) boundaries to reduce the electrical size of the model. The horn has $d = 150$ mm, with optimal perpendicular length (L_P (m)) of 388 mm to give maximum gain and minimum reflection, as calculated from Equation (3.2) [71] at 15 GHz. L_P is calculated from the slant length of the side of the horn (L_S (m)) using $\frac{d}{2}$ and Pythagoras' theorem.

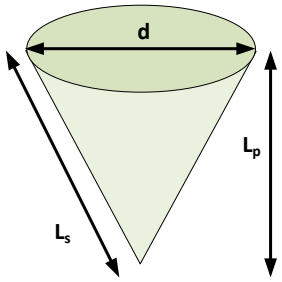

Figure 3.2: Dimensions of the conical horn to be simulated.

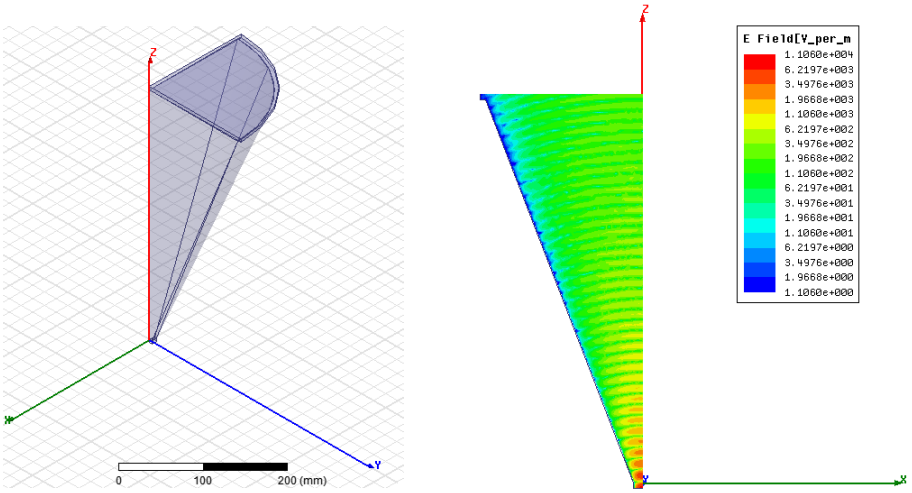

Figure 3.3: HFSS simulation set up of the conical horn and the simulated fields inside.

$$d = \sqrt{3\,\lambda\,L_S} \tag{3.2}$$

The fields inside the horn can be seen in Fig. 3.3. The external fields of this horn were sampled at the following distances:

- Quarter the Rayleigh Distance = 0.59 m
- The Rayleigh Distance = 2.37 m
- True far-field = infinity

The normalised pattern results are shown in Fig. 3.4. It can be seen that the ideal patterns are shown by the true far-field, and distances smaller than that as calculated by

the Rayleigh Distance show significant disturbance.

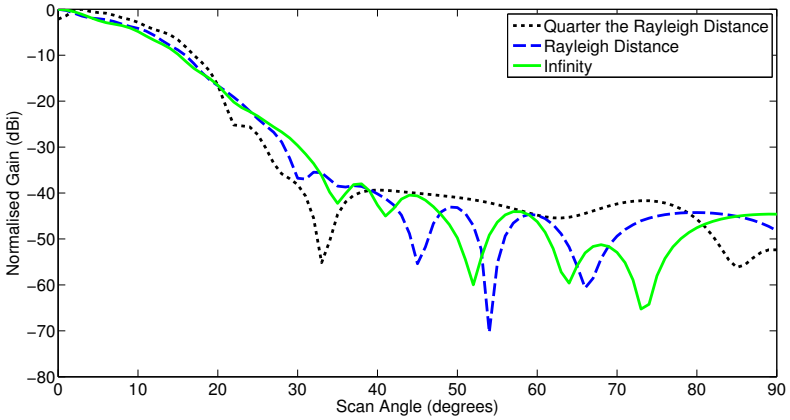

Figure 3.4: Normalised simulated fields at 0.59 m, 2.37 m and infinity from a conical horn with the same aperture size as the AUT.

3.4 CALIBRATION OF LOSSES IN AN AC

When an AC is used to measure the absolute gain of an AUT, the losses through the AC need to be measured and characterised so that they can be calibrated out of the measurement. This includes all cable, connection, instrumentation and free space losses.

The measurement of the SGH in the AC, SGH_M, gives the calibration of the AC by measuring the losses through the AC range and all connections, L_R, as shown in Equation (3.3). The AC losses should be measured by using a calibrated SGH (SGH_C (dB)) that has been tested and characterised professionally. As identical SGH are being used for this calibration the attachment of the cables to the measurement systems are the same in each case.

$$L_R = \frac{SGH_M}{10^{\frac{SGH_C}{10}}} \tag{3.3}$$

This calibration process is suitable for a single channel AUT. If a multi-channel AUT is measured then the RF path for each channel must be individually measured and calibrated. The RF path for each channel will be unique as the measurement of a TRMAS requires the addition of a multiplexer and additional cables to enable the measurement of multiple channels. All measurements should be taken in magnitude and phase.

3.5 ANTENNA GAIN CALIBRATION

There are 3 methods that can be used to measure the gain of an AUT: gain transfer, 2 horn calibration and 3 horn calibration. An equation approximation is also available. This section will investigate each method for accuracy and suitability to calculate the gain of a TRMAS and identify the most suitable method.

3.5.1 ANTENNA GAIN CALIBRATION PREPARATION

All testing will take place in the AC and for this trial 3 identical SGH will be used: SGH1, SGH2 and SGH3. This allows the results of the methods to be verified against the known calibration of the AUT. The testing will be carried out over the frequency range of the SGH, 12 to 18 GHz. One SGH will be placed at the transmit horn location and one SGH at the AUT location as described in Fig. 3.1 for the gain calibration.

To correctly carry out the calibration care has to be taken during the measurements. The SGH at the transmit and receive ends have to be carefully aligned. This is managed in the AC by accurate jigging and laser alignment to place the SGH in the correct location mechanically. This means that the mechanical alignment of the SGH is accurate and repeatable. To ensure measurement of the peak signal and hence electrical alignment the SGH are aligned using the -6 dB radiation points in AZ and EL multiple times. The electrical alignment is not preserved between each change of the SGH, so this has to be re-found each time one of the SGH is changed.

3.5.2 CALIBRATED VERSUS CALCULATED GAIN

If it is not possible to use a calibrated SGH then the gain of a SGH can be estimated from its collecting area as a function of frequency, as shown in Equation (3.4). Here G (dB) is the calculated gain of the antenna, A_P (m^2) is the physical area of the antenna and η_a (%) is the aperture efficiency of the antenna type in question. The aperture efficiency describes how efficient the antenna is at absorbing or emitting incoming plane waves at the wavelength in question and is a general term that includes aperture illumination efficiency,

spill over losses, phase-error, blockage, and depolarisation.

$$G_{dB} \;=\; 10\ log_{10}\ (\ 4\ \pi\ \frac{A_P}{\lambda^2}\ \eta_a) \tag{3.4}$$

For example, from Equation (3.4), the gain of a SGH with an aperture of 54 x 74 mm at 15 GHz with a typical aperture efficiency of 74 % is calculated to be 20.13 dBi. However, knowledge of the aperture efficiency is critical here and so needs to be determined either analytically (e.g. for a rectangular horn) or using EM modelling software. The difference between the calculated (manufacturing error quoted as 0.3 dBi) and calibrated performance of this SGH as a function of frequency can be seen in Fig. 3.5. The maximum deviation from the calibrated value is 0.226 dB and the RMS value 0.117 dB, which is within calibration tolerances. Therefore using the calculated values will introduce small errors at some frequencies, so the manufacturer's calibrated values should be used if at all possible.

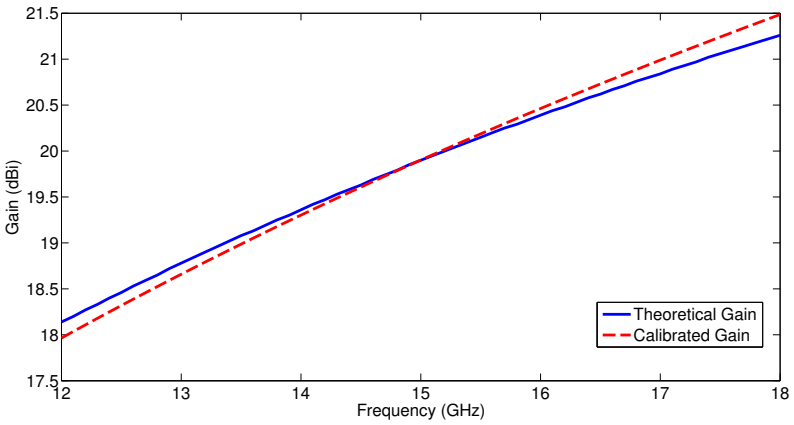

Figure 3.5: Theoretical and calibrated gain for SGH.

3.5.3 GAIN TRANSFER METHOD

To directly measure the gain of an AUT, it is usual practice to compare the measurement of the AUT received power to the measurement of a SGH received power when located at the same position as the AUT, Equation (3.5), as derived from the Friis equation [35]. Where AUT_M (dB) is the measured gain of the AUT, P_T (W) is the power received by

the AUT and P_S (W) is the power received by the SGH when measured in the AC.

$$(AUT_M)_{\,dB} \;=\; (SGH_C)_{\,dB} \;+\; 10\,\log_{10}\frac{P_T}{P_S} \tag{3.5}$$

Fig. 3.6 shows the results for the gain transfer for calculating SGH gain. SGH1 was used as the transmit horn, and SGH3 as the measured SGH when mounted on the AUT location as described in Fig. 3.1. Therefore the gain of SGH3, the AUT, is to be calculated. It can be seen that the results are very close to that of the calibrated value. For SGH1 the maximum deviation from the calibrated value is 0.024 dB and an RMS value of 0.024 dB. For SGH2 the maximum deviation from the calibrated value is 0.006 dB and an RMS value of 0.006 dB. For SGH3 the maximum deviation from the calibrated value is 0.067 dB and an RMS value of 0.048 dB.

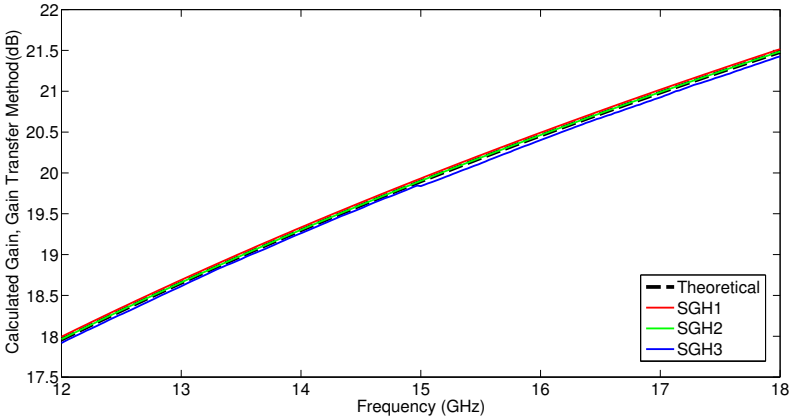

Figure 3.6: Calculated gain of the SGH from the gain transfer method for SGH3.

3.5.4 TWO HORN CALIBRATION

If both of the AUTs that need to be calibrated are the same, then the 2 horn calibration method can be used. This method uses the fact that the AUTs are the same, so transmit and receive losses are balanced; therefore the gain calculated is the gain of either AUT. It is not required to know the gain of one of the AUTs. One AUT is placed at the transmit horn location and the other is placed at the AUT location as described in Fig. 3.1. There are losses in this set up that need to be measured and accounted for:

- Transmission loss between the two horns, the Free Space Loss (FSL (dB)) as defined in Equation (3.6). Range Length (RL (m)) is the distance between the apertures of the two SGHs in the AC.
- Loss through the transmit cables, that run from the VNA to the transmit AUT (L_{TX} (dB)).
- Loss through the receive cables, which run from the receive AUT to the VNA (L_{RX} (dB)).

$$FSL \;=\; -\;20\;log_{10}\;\frac{4\;\pi\;RL}{\lambda} \tag{3.6}$$

$AUT1_G$ (dB) is the measured gain of $AUT1$, $AUT2_G$ (dB) is the measured gain of $AUT2$ and $AUT3_G$ (dB) is the measured gain of $AUT3$. An example transmitting from $AUT1$ and receiving on $AUT2$ is shown in Equation (3.7).

$$AUT1_G \; or \; AUT2_G \;=\; -\;0.5\;(\;FSL\;-AUT_M\;-\;L_{TX}\;-\;L_{RX}) \tag{3.7}$$

Fig. 3.7 shows the results for the 2 horn method for calculating SGH gain. The first named SGH was used as the transmit horn, and the second named SGH as the receive horn. All permutations of the available SGH were measured.

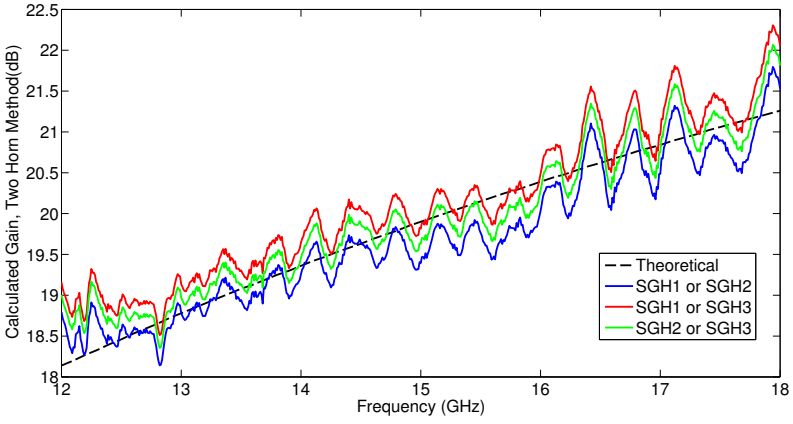

Figure 3.7: Calculated gain of the SGH from the 2 horn method.

It can be seen that there is much more variation in these measurements than for the gain transfer method. This is to be expected as the calibration of the long transmit and receive

cables cannot be carried out in their measurement position increasing the error. However, it can be clearly seen that the trend of the values match well and this is a valid method for gain calculation. For SGH1 or SGH2 the maximum deviation from the calibrated value is 0.835 dB and the RMS value 0.359 dB. For SGH1 or SGH3 the maximum deviation from the calibrated value is 1.199 dB and the RMS value 0.424 dB. For SGH2 or SGH3 the maximum deviation from the calibrated value is 1.048 dB and an RMS value of 0.337 dB.

3.5.5 THREE HORN CALIBRATION

In the 3 horn calibration method 3 AUTs are required and a transmission of all permutations between each of the AUT must be conducted. It is not required to know the gain of one of the AUT. A transmission occurs between two of the AUT, $AUT1to2_M$, and the gain can be calculated from Equation (3.8). Again, there is no loss included in Equation (3.8) as an AC calibration. Therefore this has to be included in the form of the *FSL* as defined in Equation (3.6) and the additional losses of L_{TX} and L_{RX}. The measurement is then repeated for *AUT1to3* and *AUT2to3* forming a set of simultaneous equations, Equation (3.8).

$$\begin{aligned} AUT1to2_G &= (\ FSL\ - AUT1to2_M\ -\ L_{TX}\ -\ L_{RX}) \\ AUT2to3_G &= (\ FSL\ - AUT2to3_M\ -\ L_{TX}\ -\ L_{RX}) \\ AUT1to3_G &= (\ FSL\ - AUT1to3_M\ -\ L_{TX}\ -\ L_{RX}) \end{aligned} \tag{3.8}$$

Solving these simultaneous equations gives the indiviual gain of each AUT, Equation (3.9).

$$\begin{aligned} AUT1_G &= \frac{AUT1to2_G\ +\ AUT1to3_G\ -\ AUT2to3_G}{2} \\ AUT2_G &= \frac{AUT1to2_G\ -\ AUT1to3_G\ +\ AUT2to3_G}{2} \\ AUT3_G &= \frac{-\ AUT1to2_G\ +\ AUT1to3_G\ +\ AUT2to3_G}{2} \end{aligned} \tag{3.9}$$

Fig. 3.8 shows the results for the 3 horn method for calculating SGH gain. The first named SGH was used as the transmit horn located at the transit horn, and the second named SGH as the receive horn. All permutations of the available SGH have to be measured. It can be seen that there is much more variation in these measurements than for the gain transfer method, and slightly more than the 2 horn method. This is to be expected as the calibration of the transmit and receive cables cannot be carried out in their measurement position so there are unwanted reflections in the measurement from the different bends in the cables, attenuation was used to try and minimise the effects. However, it can be clearly seen that the trend of the values match well and this is a valid method for gain calculation. The best fit for the calibrated value is SGH1, with a maximum deviation from the calibrated value of 0.987 dB and an RMS value of 0.322 dB. For SGH2 the maximum deviation from the calibrated value is 1.061 dB and the RMS value 0.477 dB. For SGH3 the maximum deviation from the calibrated value is 1.441 dB and the RMS value 0.606 dB.

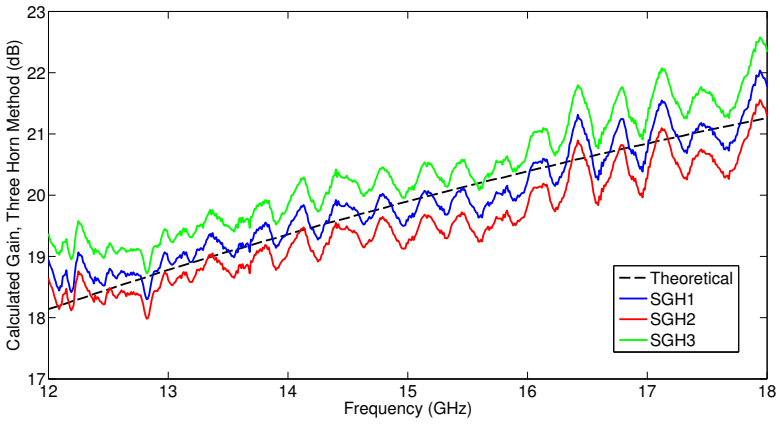

Figure 3.8: Calculated gain from the 3 horn calibration.

3.5.6 ANTENNA GAIN CALIBRATION FOR A TRMAS

From Table 3-A it can be seen that all methods to calculate the gain can give a viable RMS difference from the theoretical value. The lowest deviation from the theoretical value comes from the gain transfer method. The gain transfer method is the simplest calibration to perform, and as it gives good results this will be chosen as the preferred method, particularly as it has to be repeated for each channel of the TRMAS. In this environment the most accurate measurement method is the gain transfer method. However, this will not

be applicable to every range. Indeed in dedicated calibrated ranges the 3 horn calibration method is found to be the most accurate when averaged over many measurements.

Ideally, this involves taking measurements of the antenna and the SGH at the same time and with the same experimental set up. In reality, the measurements have to be taken sequentially and the losses of the additional hardware taken into account in the calculation. This accounts for any variations in the range with time and ensures these are not attributed to the antenna behaviour. The measurement is typically taken as a function of frequency and calculated using amplitudes only. The SGH should be illuminated by a plane wave of the same polarisation as the AUT.

METHOD	**STANDARD GAIN HORN MEASURED**	**MAX DEVIATION FROM GAIN (dB)**	**RMS (dB)**
CALCULATED GAIN	SGH1, SGH2, SGH3	0.23	0.12
GAIN TRANFER METHOD	SGH1	0.02	0.02
	SGH2	0.01	0.01
	SGH3	0.07	0.05
2 HORN CALIBRATION	SGH1 or SGH2	0.84	0.36
	SGH1 or SGH3	1.20	0.42
	SGH2 or SGH3	1.05	0.34
3 HORN CALIBRATION	SGH1	0.99	0.32
	SGH2	1.06	0.48
	SGH3	1.44	0.61

Table 3-A: Comparison of results from gain calibration methods.

3.6 CALIBRATION OF AN ANECHOIC CHAMBER FOR MEASUREMENT OF A MULTI-CHANNEL ANTENNA

3.6.1 EQUATIONS TO CALIBRATE AN ANECHOIC CHAMBER

To complete a true measurement of losses in an AC for a TRMAS, all measurements should be vectors and calculations completed as phasors. The measurement of a SGH, (SGH_M) as a complex gain in dimensionless units relative to an isotropic radiator, allows a range calibration and the gain of the AUT to be calculated. This measurement quantifies the losses through the range (L_R (dB)) if SGH_C is known and the additional hardware losses for the SGH are measured on a VNA (L_{SGH} (dB)), as shown in Equation (3.10). The additional hardware should be added at a matched plane so reflection losses can be minimised. If this is not possible then it is possible to use isolators or attenuators at either side of the split plane to achieve this result. It should be remembered that all losses have a negative value and all gains a positive value.

$$|SGH_M| \ = \frac{10^{\frac{|SGH_C|}{10}}}{|L_{SGH}|} \ |L_R| \tag{3.10}$$

Once this calibration is completed the SGH can be swapped for the AUT and its AUT_M measured. From these values the gain and phase of the AUT (AUT_G (dB)) can be calculated as shown in Equation (3.11).

$$AUT_G \ = \ 10 \ log_{10} \ \frac{|AUT_M| \ |L_{AUT}| \ |L_{SGH}|}{|L_R|} \tag{3.11}$$

Equations (3.10) and (3.11) can be combined as shown in Equation (3.12) to directly calculate the gain of an AUT measured in an anechoic chamber by comparison to a SGH.

$$AUT_G \ = \ 10 \ log_{10} \ \frac{|AUT_M| \ |L_{AUT}| \ 10^{\frac{|SGH_C|}{10}}}{|SGH_M|} \tag{3.12}$$

Since a TRMAS is being measured this calibration process needs to be repeated for the RF path for each channel to be measured and will be presented in the next section.

3.6.2 AC CALIBRATION FOR A MULTI-CHANNEL AUT

A SGH, whose calibration can be seen in Fig. 3.5, was mounted in the positioner and a measurement taken for each of the four RF paths used to measure a TRMAS. This gives the SGH_M for each of the individual channels. These results are shown in Fig. 3.9. It can be seen that each path is unique; in this particular case this is due to the use of a multiplexer and short hand-formable semi-rigid coax cables to connect the TRMAS to the measurement path. Therefore, to avoid errors, it is important that each channel is calibrated individually.

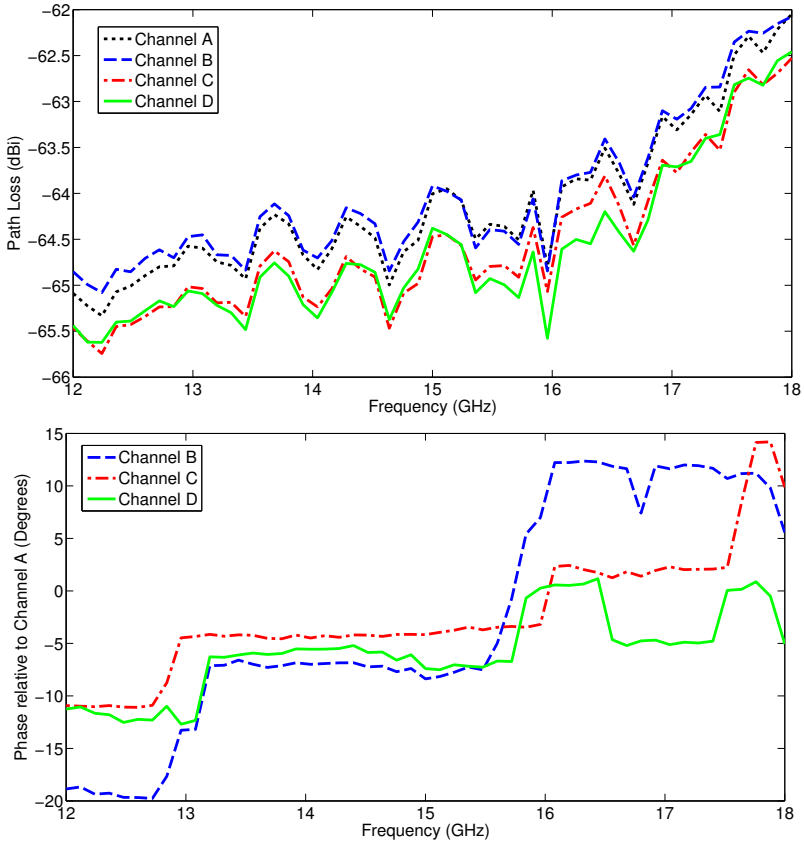

Figure 3.9: SGH_M for the 4 RF paths measured in the AC.

In addition to the losses through the RF measurement path, additional hardware is required to connect the SGH to the measurement system. This additional hardware is a cable, loss measured as a function of frequency, L_{SGH}, as shown in Fig. 3.10. Reflections seen in this figure are due to bends in the cables and the connectors. In this case the additional hardware occurs in the common RF path for each channel, a single measurement can be used for all channels.

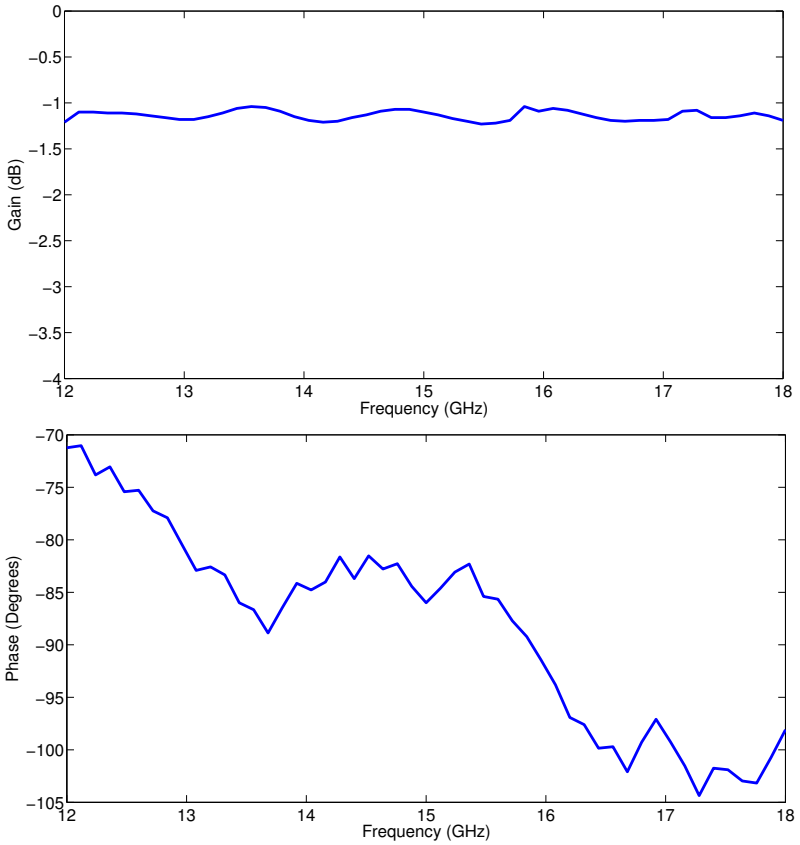

Figure 3.10: L_{SGH}.

Next the SGH is replaced with the TRMAS and the measurement repeated through each RF channel, giving AUT_M, as shown in Fig. 3.11. It can be seen that each channel performs differently as a function of frequency. This is in part due to the different hardware path for each channel and in part inherent with the TRMAS.

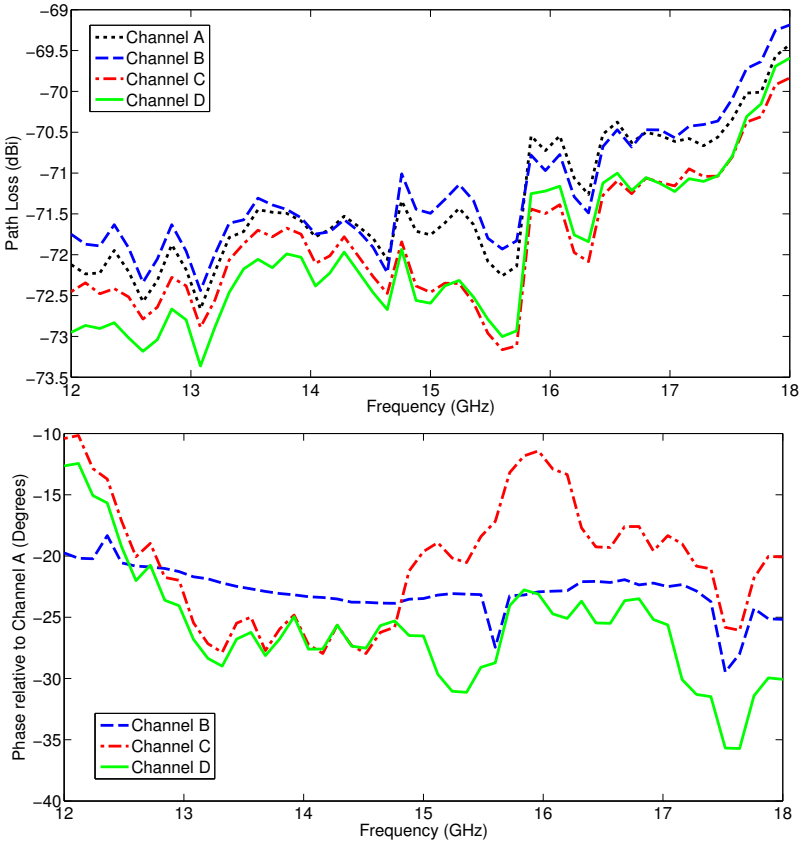

Figure 3.11: AUT_M for the 4 RF paths measured in the AC.

When these results are combined as shown in Equation (3.12) the AUT_G for each channel of the TRMAS can be plotted as shown in Fig. 3.12. The variation of gain as a function of frequency is due to the physical structure of the TRMAS. The average standard deviation over frequency for the gain is 0.38 dB, and the phase is 12.02^o.

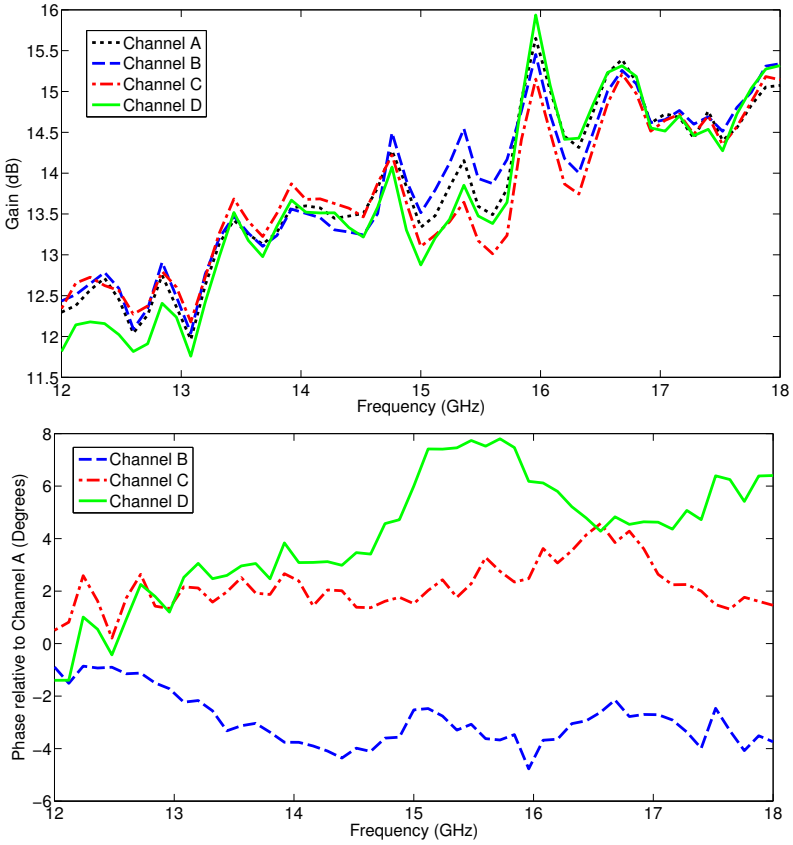

Figure 3.12: Calibrated AUT_G for the 4 RF paths measured in the AC.

As can be seen, the four different channels of the TRMAS inherently perform differently as a function of frequency. If a single calibration had been applied to all channels this variation would still be present, as shown earlier, but there would be an additional difference due to the hardware set up that was not accounted for. The average standard deviation over frequency for the gain is 0.19 dB, and the phase is 3.14^o. This is a significant improvement over the non-calibrated results.

Calculations should be completed as phasors as the phase varies between channels and this difference needs to be accounted for to remove additional sources of error.

These four channels can now be combined together using a comparator or software combination to calculate the true Σ pattern gain of the multi-channel AUT.

3.7 PHASE STABLE MULTI-CHANNEL AUT PATTERN MEASUREMENTS ON A MOVING POSITIONER

3.7.1 POSITIONING SYSTEM USED FOR DATA COLLECTION

The positioning system has specific cable routing attachments that minimise the movement of the cables when the positioner is moving. The AUT is mounted on the positioner and focussed so the position of the phase centre of the AUT does not move as the positioner rotates.

3.7.2 MULTI-CHANNEL ANTENNA MEASUREMENT OPTIONS

There are two different measurement scenarios for a TRMAS:

- **Point-to-point measurement.** The positioner is moved to its first measurement position and the data for all channels is taken. The positioner is then moved to its next data collection point where the measurement process is repeated. This process is repeated as a stepped scan until the required data set has been collected.
- **Swept measurement.** The positioner prescribes an angular sweep through its desired data collection movement, taking data as it moves without stopping. The rate of sweep and data collection are kept the same so scans will have the same data set. A single channel's data could be collected each sweep. Therefore this movement of the positioner would then have to be repeated for each channel in turn. Or, with higher specification multi-channel VNA or Special To Type Equipment (STTE) it would be possible to collect data on multiple channels simultaneously if 4 cables were used. Collected RF data would then have to be synchronised to the angular pick off data from the positioner.

In addition to the measurement scenario there are two hardware configurations that could be implemented to measure a TRMAS:

- **Multi-channel VNA.** The use of a multi-channel VNA and multiple RF cables running from the TRMAS to the VNA as shown in Fig. 3.13.
- **Multiplexer.** The use of an RF switch mechanism (multiplexer) mounted directly behind the TRMAS, and a single RF cable running from the multiplexer to a single receive channel network analyser as shown in Fig. 3.14.

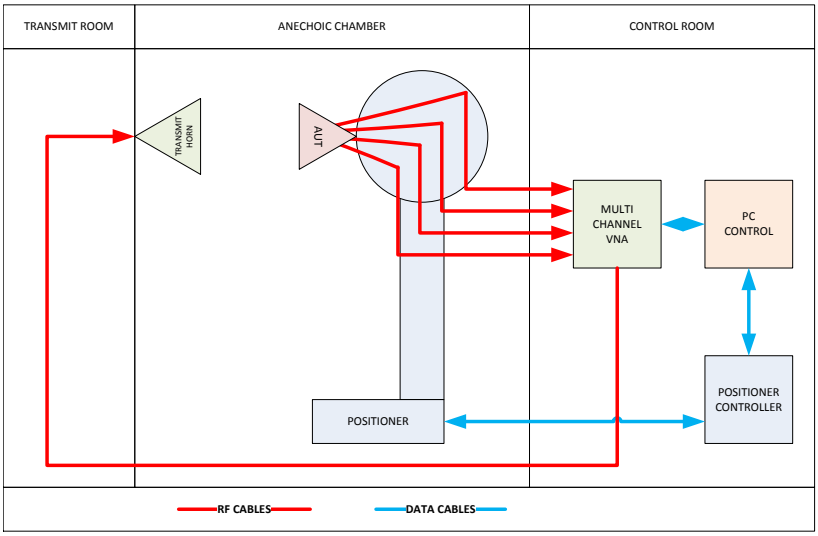

Figure 3.13: AC for TRMAS measurement with four RF cables and a multi-channel VNA.

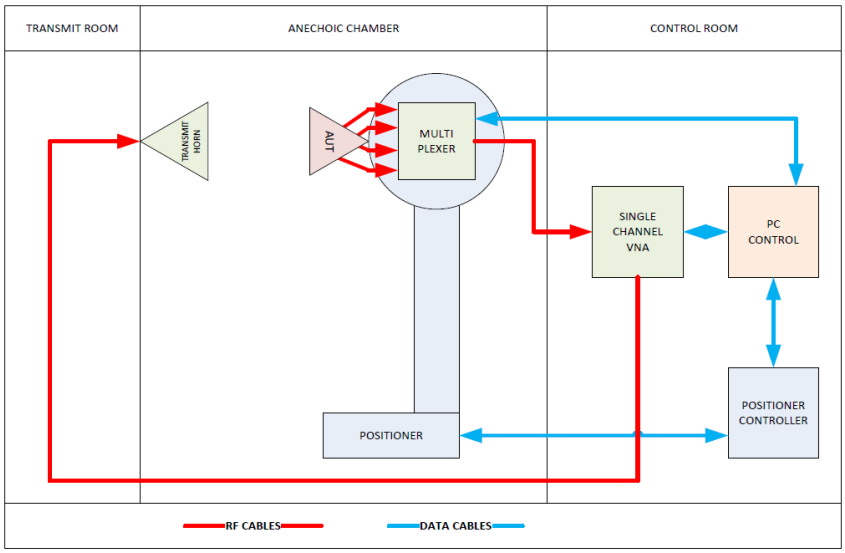

Figure 3.14: AC for TRMAS measurement with a multiplexer and a single channel VNA.

To assess the level of error introduced by moving cables, the existing measurement positioning system inside the AC was used as a measurement test case. Multiple 10 m phase stable RF cables were run along the cable routing system of the positioner from the head of the TRMAS to the VNA. 10 m is the shortest length of cable to allow the full movement of the positioner and to allow connection to the VNA in the control room. The cable quality used will have an impact on the measurements. In this thesis the cables used have an insertion loss of 0.049 dBm^{-1} at 12 GHz and the two way S_{11} with straight connectors as seen in Fig. 3.15. The VNA was used to measure the S_{11} return loss of the cable as the positioner was moved, the cable being terminated at the AUT end with a 50 Ω load. Averages of 10 repeat measurements for each movement type will be presented. Before measurement, to ensure phase stability, the cable should be measured [72] and calibrated [38].

3.7.3 IMPACT OF CABLE MOVEMENT ON MEASUREMENTS

To assess the impact of movement type on magnitude and phase results, measurements were taken to represent the point-to-point and swept measurement movement.

3.7.3.1 ASSESSMENT OF MEASUREMENT STABILITY

10 repeat measurements were taken at a positioner angle of Azimuth = 0^o, Elevation = 0^o and Roll = 0^o without a movement of the positioner in between measurements. Fig. 3.15 shows the results of each measurement. Considerable variation in the S_{11} amplitude is seen across the frequency band, demonstrating the change in match resulting from the bending of the 10 m cable.

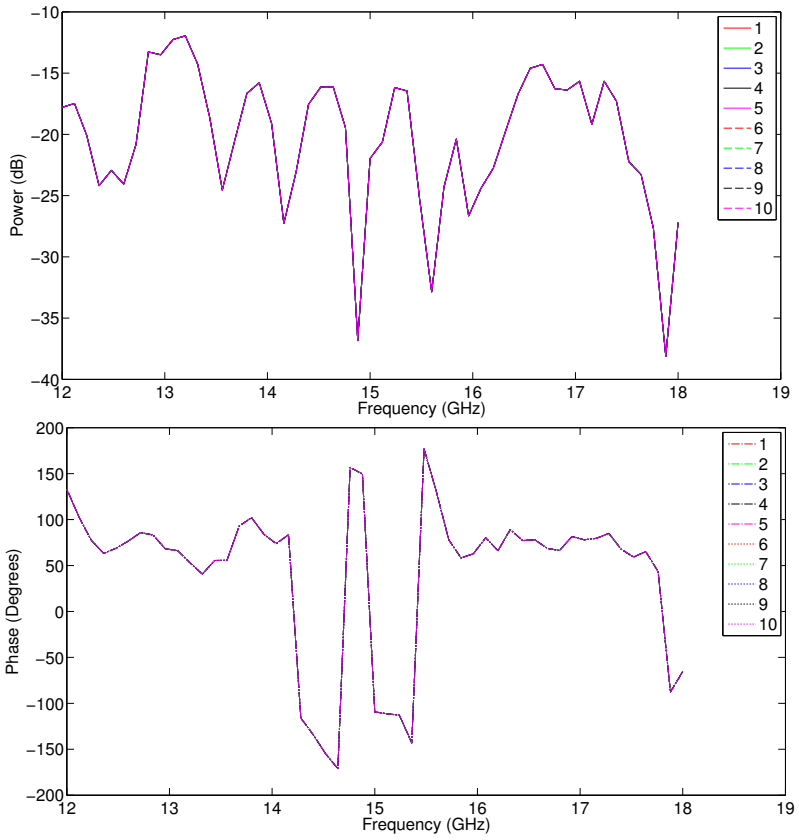

Figure 3.15: 10 repeat measurements for a single non-moving cable.

Fig. 3.16 shows the results more clearly as a difference from the mean value of the 10 repeat measurements as a function of frequency for both the magnitude and phase. For future measurements of this type only the difference graphs will be shown. It can be seen that the magnitude variation is stable with a maximum deviation from the mean of 0.022 dB and a standard deviation of 0.003 dB. The phase measurement has a higher maximum deviation from the mean value of 0.160^o, and a standard deviation of 0.027^o for the non-moving cable. In a monopulse system this level of magnitude and phase variation leads to a change in Σ pattern gain of 0.066 dB and in phase of 0.002^o as calculated by using the model presented in Chapter 7.

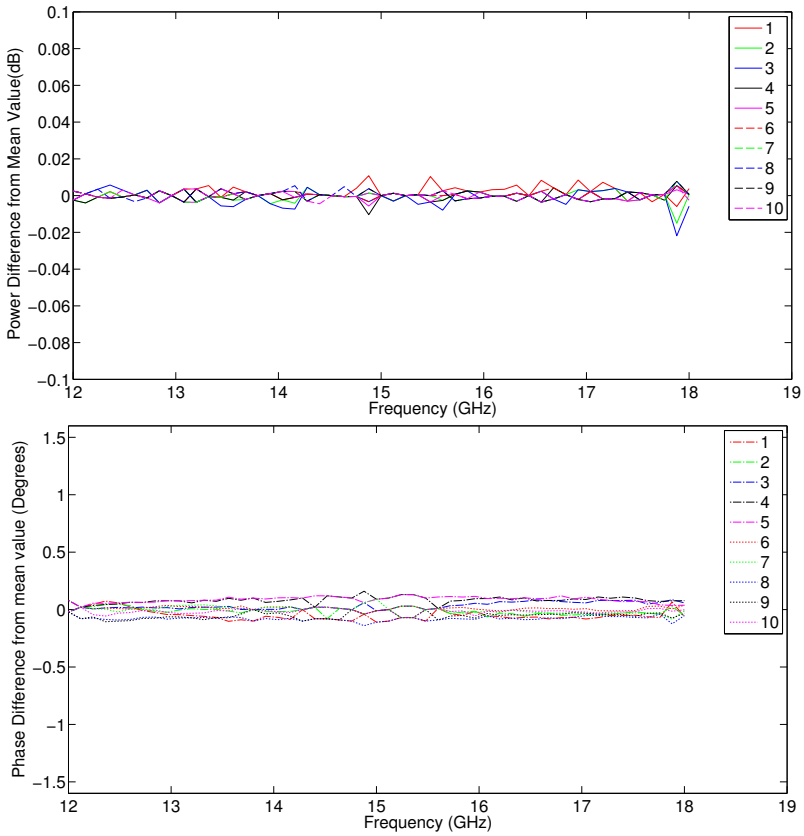

Figure 3.16: Difference from mean value of 10 repeat measurements for a non-moving cable.

3.7.3.2 ASSESSMENT OF MOVEMENT BETWEEN MEASUREMENTS IN THE SAME POSITION ON MEASUREMENT STABILITY

10 repeat measurements were then taken at the same positioner angle. However, this time there had been a movement of the positioner of 1^o in all axes before returning to the start position. Fig. 3.17 shows the results as a difference from the mean value as a function of frequency. The magnitude variation is a maximum deviation from the mean value of 0.028 dB, with a standard deviation of 0.005 dB. The phase variation is a maximum deviation from the mean value of 0.399^o, with a standard deviation of 0.068^o. In a monopulse system this level of magnitude and phase variation leads to a change in Σ pattern gain of 0.085 dB and in phase of 0.005^o. As you would expect these values are higher than that of a non-moving system as they include the accuracy of the positioner and the cables to return to exactly the same start position.

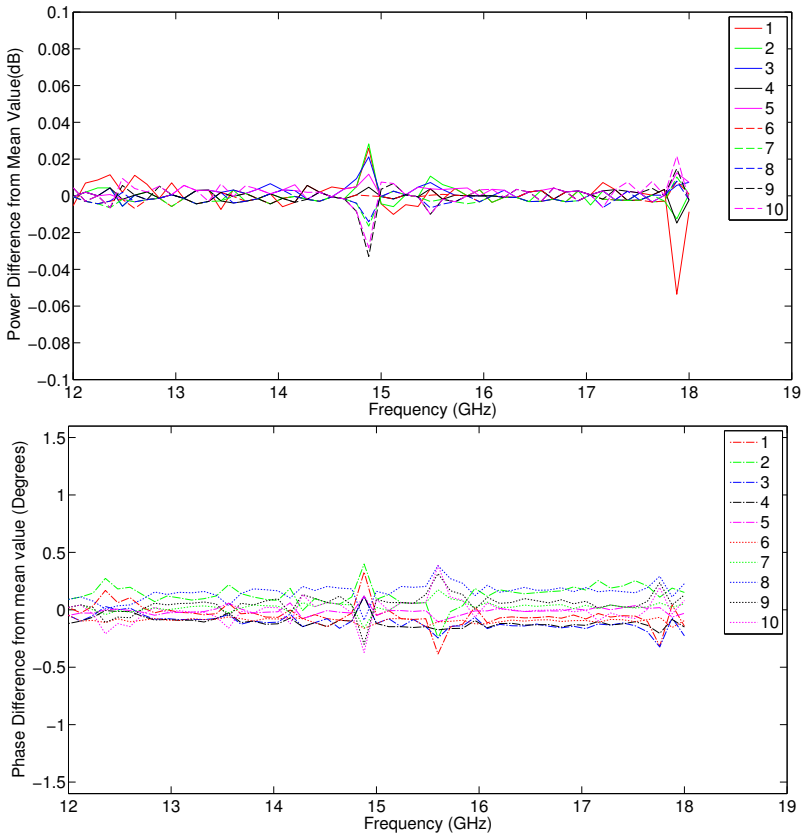

Figure 3.17: Difference from mean value of 10 repeat measurements for cable moved between measurements and returned to start position.

3.7.3.3 ASESSMENT OF SMALL MOVE ON MEASUREMENT STABILITY

10 repeat measurements were then taken starting at the same positioner angle followed by a movement of the positioner of 1^o in all axes. 1^o was chosen as this is a typical step size for an antenna pattern measurement. Fig. 3.18 shows the results as a difference from the mean value as a function of frequency. The magnitude variation is a maximum deviation from the mean value of 0.054 dB, with a standard deviation of 0.006 dB. The phase variation is a maximum deviation from the mean value of 0.589^o, with a standard deviation of 0.088^o. In a monopulse system this level of magnitude and phase variation leads to a change in Σ pattern gain of 0.162 dB and in phase of 0.008^o.

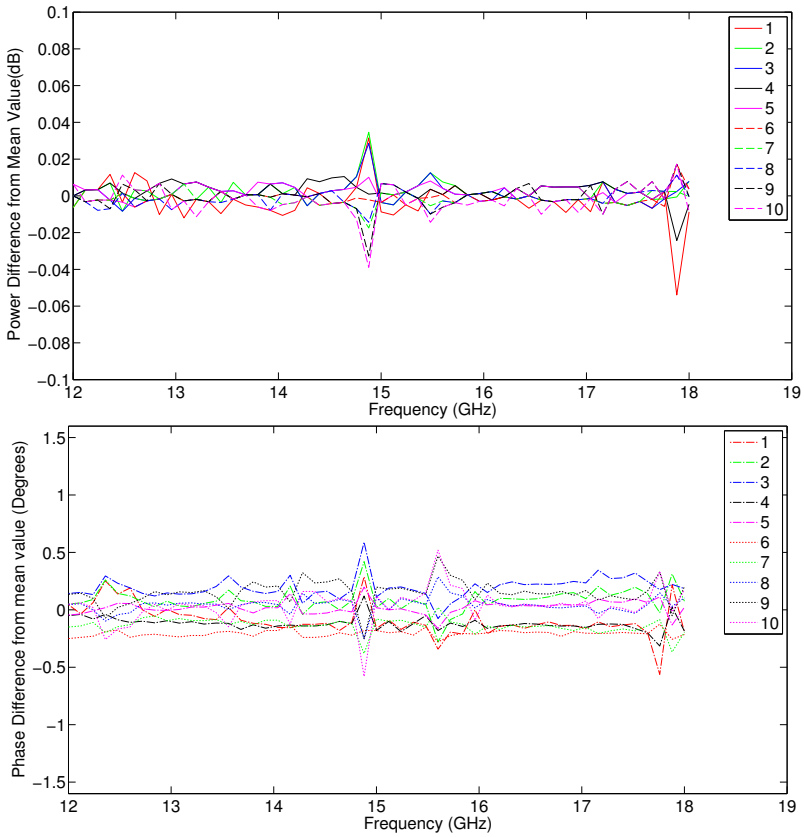

Figure 3.18: Difference from mean value of 10 repeat measurements for a cable that was moved 1^o between measurements.

3.7.3.4 ASSESSMENT OF A LARGE MOVE ON STABILITY

10 repeat measurements were then taken at the same positioner angle followed by a movement of the positioner of 40^o in all axes. Fig. 3.19 shows the results as a difference from the mean value as a function of frequency. The magnitude variation is a maximum deviation from the mean value of 0.055 dB, with a standard deviation of 0.010 dB. The phase variation is a maximum deviation from the mean value of 0.594^o, with a standard deviation of 0.098^o for the non-moving cable. In a monopulse system this level of magnitude and phase variation leads to a change in Σ pattern gain of 0.166 dB and in phase of 0.008^o. It can be seen that these values are similar to that of a small move. This is to be expected as the cause of the change is due to the movement of the positioner which is specifcally designed to minimise the movement of the cables.

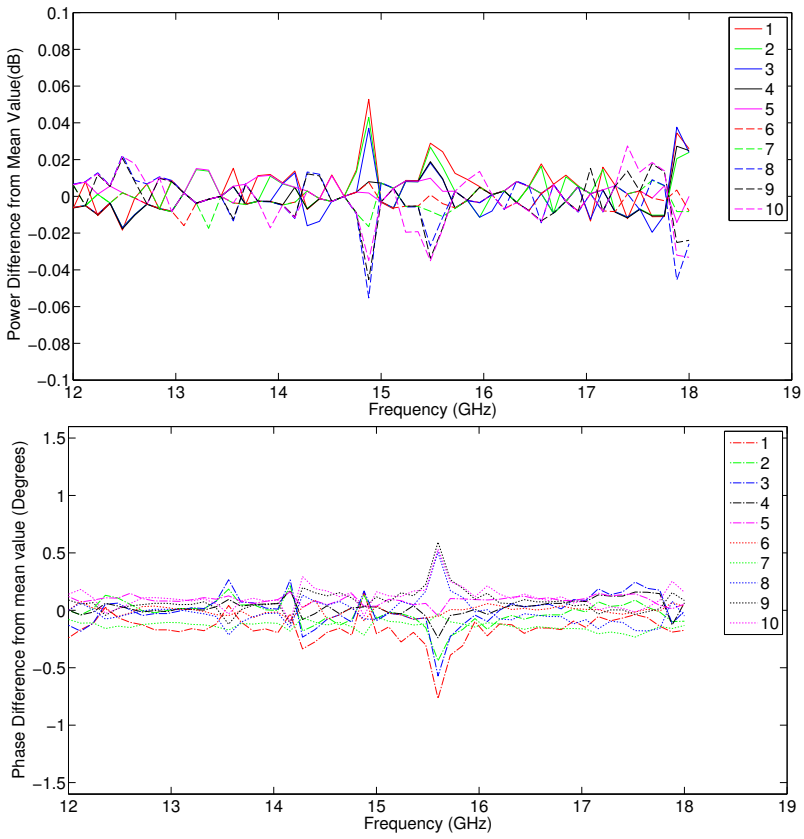

Figure 3.19: Difference from mean value of 10 repeat measurements for a cable that was moved 40^o between measurements.

From Figs. 3.16, 3.18 and 3.19, it can be seen that introducing a movement between measurements on a TRMAS will increase the maximum deviation from the mean phase and the standard deviation by 4 times. There is less effect on the magnitude, a factor of 3, which is expected as the magnitude is known to be more stable than phase for a moving RF cables. Therefore to minimise the phase difference between measurements there should be no movement of the cables, and thus no movement of the positioner between measurements.

In conclusion, data taken on multi-channel AUTs should be taken in a point-to-point manner to reduce errors introduced by the measurement configuration.

3.7.4 IMPACT OF MULTIPLE RF CABLES ON MEASUREMENTS

If multiple cables are used to measure the TRMAS there will be a magnitude and phase difference introduced between each channel due to the different cables. This difference could be calibrated out of the system [38], but this would be only valid for a static position, as previously shown. A calibration measurement could be taken at every positioner angle, however the previous section shows that the measurements are not necessarily repeatable after a positioner movement. To assess the preferred hardware configuration for stable phase measurements, measurements were taken on two identical cables attached to the AUT.

10 repeat measurements on two RF cables were taken at the same positioner angle but with a movement of the positioner of 1^o in all axes in-between measurements. The difference between the cables was calibrated out before the start of the measurements and the cables follow the same routing along the positioner. Fig. 3.20 shows the measurement on cable 2 as a difference from the mean value of cable 1 as a function of frequency. The magnitude variation has a maximum deviation from the mean value of 0.063 dB, with a standard deviation of 0.010 dB. The phase variation has a maximum deviation from the mean value of 1.680^o with a standard deviation of 0.280^o. In a monopulse system this level of magnitude and phase variation leads to a change in Σ pattern gain of 0.188 dB and in phase of 0.023^o.

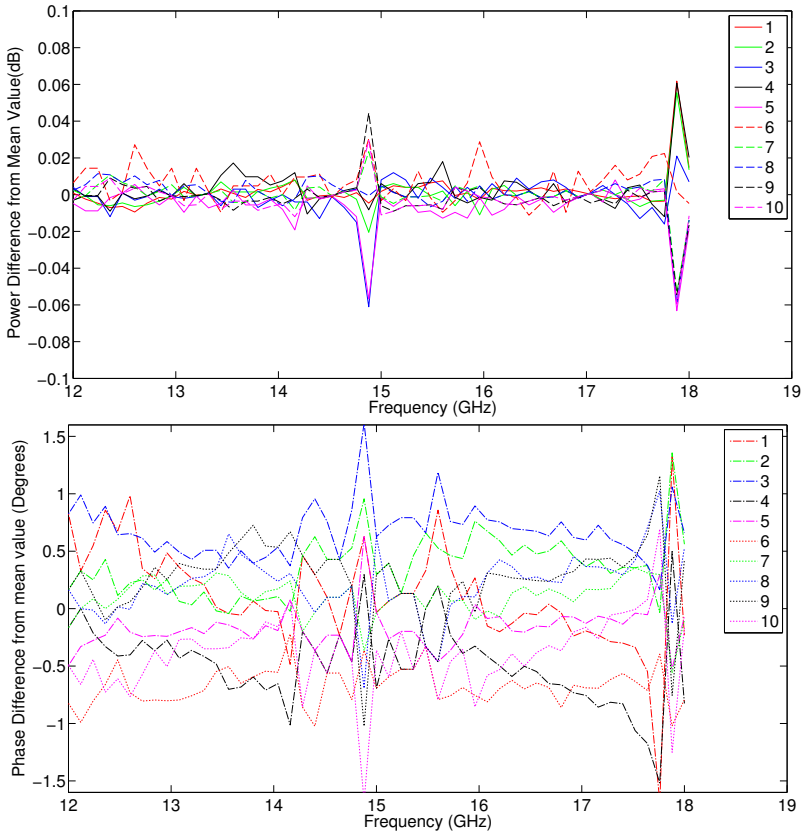

Figure 3.20: Difference from mean value of 10 repeat measurements for two cables that were moved between measurements.

This shows that the introduction of a second cable with a movement between measurements increases the magnitude deviation from the mean by a factor of 3 and the phase by a factor of 10. These are both significantly higher than the error introduced by movement

alone.

Therefore to minimise errors, a single long RF cable should be used with a multiplexer behind the TRMAS. There will need to be a cable from each output of the TRMAS to the switch mechanism which should be mounted as close to the TRMAS as possible. Since these do not need to move, these cables can be rigid cables, so the magnitude and phase variation between the different channels will not alter and therefore can be calibrated out [38].

3.7.5 IMPACT OF TEMPERATURE VARIATION ON MEASUREMENTS

All the measurements presented so far have been taken in an AC that is temperature controlled by an air-conditioning unit, the temperature is stable to 19 $\pm$ 1^{o}C over the course of a day. The following will investigate the effect of a temperature change between measurements, as could be seen on an outdoor range or an equipment failure in an AC. Measurements of a single static cable were taken at 19^{o}C, with no movement to the positioner or cable the air-conditioning unit was then switched off. When the temperature measured 24^{o}C the measurement was taken again when temperature equilibrium was reached.

Fig. 3.21 shows the measurement on cable 2 as a difference from the mean value of cable 1 as a function of frequency. The magnitude variation has a maximum deviation from the mean value of 0.064 dB, with a standard deviation of 0.009 dB. The phase variation has a maximum deviation from the mean value of 1.345^o with a standard deviation of 0.186^o. In a monopulse system this level of magnitude and phase variation leads to a change in Σ pattern gain of 0.190 dB and in phase of 0.019^o. It can be seen that this is of the same order as using different cables. If a change in temperature is suspected between measurements, then this must be taken into account.

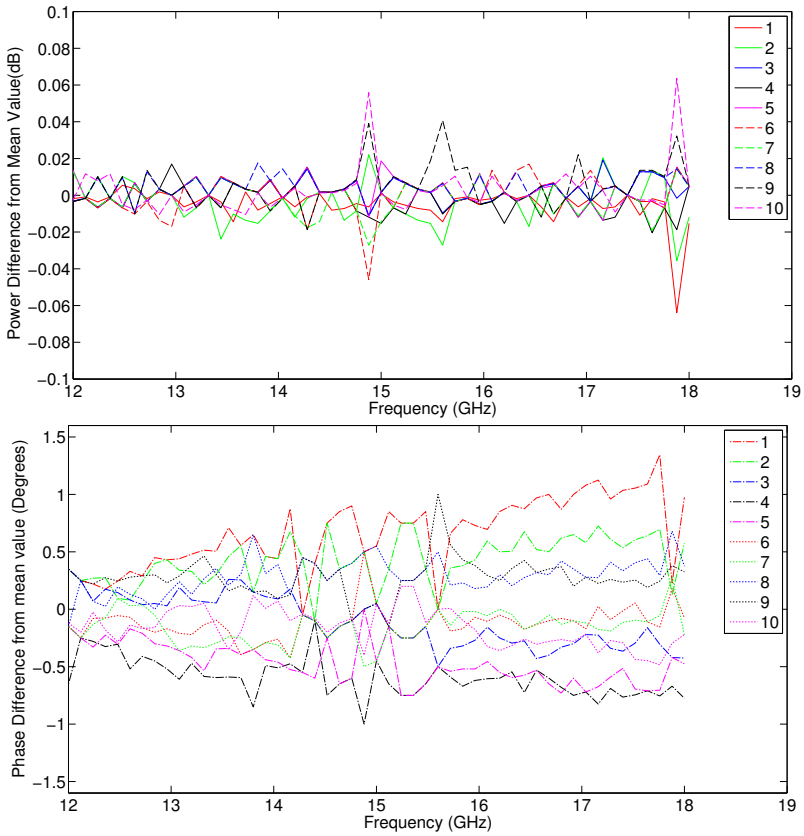

Figure 3.21: Difference from mean value of 10 repeat measurements for a cable that was measured hot and cold.

3.8 TEST RESULT CONCLUSIONS

Table 3-B shows the effect on magnitude and phase for the different test scenarios. Table 3-C shows the summary of the effect on peak Σ gain and phase on the patterns produced by the different test scenarios. In each case of increased movement it can be seen that there is a detrimental effect on the measurement stability. Using a second cable, or altering the temperature, has a further detrimental impact on the measurements.

MEASUREMENT	**MAGNITUDE MAXIMUM DEVIATION FROM MEAN (dB)**	**MAGNITUDE SD (dB)**	**PHASE MAXIMUM DEVIATION FROM MEAN (^{o})**	**PHASE SD (^{o})**
NO MOVE	0.022	0.003	0.160	0.027
1^o BACK TO [0, 0]	0.028	0.005	0.399	0.068
1^o MOVE	0.054	0.006	0.589	0.088
40^o MOVE	0.055	0.010	0.594	0.098
2 CABLES	0.063	0.010	1.680	0.280
TEMPERATURE	0.064	0.009	1.345	0.186

Table 3-B: Comparison of measured deviations from mean for different cable scenarios.

	SUM PATTERN GAIN CHANGE (dB)	**SUM PATTERN PHASE CHANGE (^{o})**
NO MOVE	0.066	0.002
1^o BACK TO [0, 0]	0.085	0.005
1^o MOVE	0.162	0.008
40^o MOVE	0.166	0.008
2 CABLES	0.188	0.023
TEMPERATURE	0.190	0.019

Table 3-C: Comparison of calculated sum pattern changes due to deviations from mean in Table 3-B.

3.9 ALTERNATIVE MEASUREMENT POSSIBILITIES

It is possible to manufacture STTE that would measure the magnitude and phase with an integral analysis system that would mount directly behind the TRMAS and produce the Σ and Δ signals. These signals would still have to be routed to the analysis PC, but would be in data cables removing the issue of transferring an RF signal over a moving cable. However, this process is expensive, lengthy and will be applicable only to the TRMAS in consideration. It also requires a significant amount of space behind the TRMAS.

Alternatively, it is also possible to purchase a measurement head for a VNA that can be located at the back of the AUT. This would down convert the signal before it travels along 4 long RF cables to the VNA. Another option would be to mix the signal with a local oscillator signal to down convert the signal to an intermediate frequency. If the signal was down converted by a factor of 10 then the phase stability would have to be increased by a factor of 10. This, along with the multiple long RF cables that would have to be used and the space required behind the TRMAS mean this expensive solution is not suitable.

3.10 CHAPTER SUMMARY

This chapter has described a new procedure to calibrate a TRMAS in an AC. This is a novel extension to current practice that describes the calibration of an AC for a single channel antenna. It presents the best practice that the RF path for each of the channels is measured separately, recording both magnitude and phase. All calculations presented should be conducted as phasors. It can be seen that the calibrated antenna gain gives the true gain of the antenna and does not suffer from the range effects that would give false readings. This calibration process can be applied to many different types of measurement ranges.

In addition this chapter has identified and quantified the best technique for stable phase measurement on a TRMAS in an AC. It has been shown that the measurement procedure to give the most stable magnitude and phase measurements occur when a multiplexer unit is situated directly behind the TRMAS and a single RF cable is run from the TRMAS to the VNA. The measurements are to be taken in a point-to-point configuration. This hardware set up and measurement procedure is applicable to different range types. For TRMAS measurements the measurements between the 4 channels are taken quickly, if a long run of several hours or days is completed there could be a change in temperature between the start and the end of a run.

The next chapter finalises the investigation into the hardware test set up and measurement methodology for a TRMAS, and details the derivation and test of an AT required for accurate characterisation of a TRMAS.

Chapter 4

AXIS TRANSFORM FOR ACCURATE CHARACTERISATION OF A TWIST REFLECTOR MONOPULSE ANTENNA SYSTEM AND RADOME

4.1 INTRODUCTION

The work in this chapter is relevant to the field of antenna measurements as it presents a comprehensive explanation of how to calculate an AT for a positioning system that is suitable for measuring a TRMAS with a radome. The AT will include the novel approach of including the radome aberration as an integral part. Firstly an AT will be derived that will allow movement of the positioner in the AUT beam frame. This AT will be assessed in simulation, hardware test and antenna measurements for its suitability of measuring a TRMAS radome system.

The following sections show a worked example of the definition of co-ordinate systems, the construction of a directional cosine matrix to define the AT and a multiplication of several ATs into a single mathematical operation. The specific measurements and co-ordinate frames shown here are correct for the needs of this thesis. As the AUT in question is liearly polarised knowledge of the reference **E** is of great importance[73].

4.2 REQUIRED AXIS TRANSFORM DEFINITIONS

In order to define an AT between different co-ordinate systems, the co-ordinate systems and transfer rules first need to be defined. The situation is further confused in terms of a TRMAS as they themselves have a scanning mechanism. This thesis defines four co-ordinate systems which will uniquely include the radome aberration: the Chamber Frame (C) whose definitions match the yaw, pitch and roll of an aircraft; the System Body Frame (S) which defines the alignment of the AUT in the positioner; the Commanded Beam Frame (B) which defines how we want the AUT to move; and the True Beam Frame (T) which is the true beam of the AUT. These are defined in Fig. 4.1. All co-ordinate frames are right handed, as defined by Fleming's right hand rule.

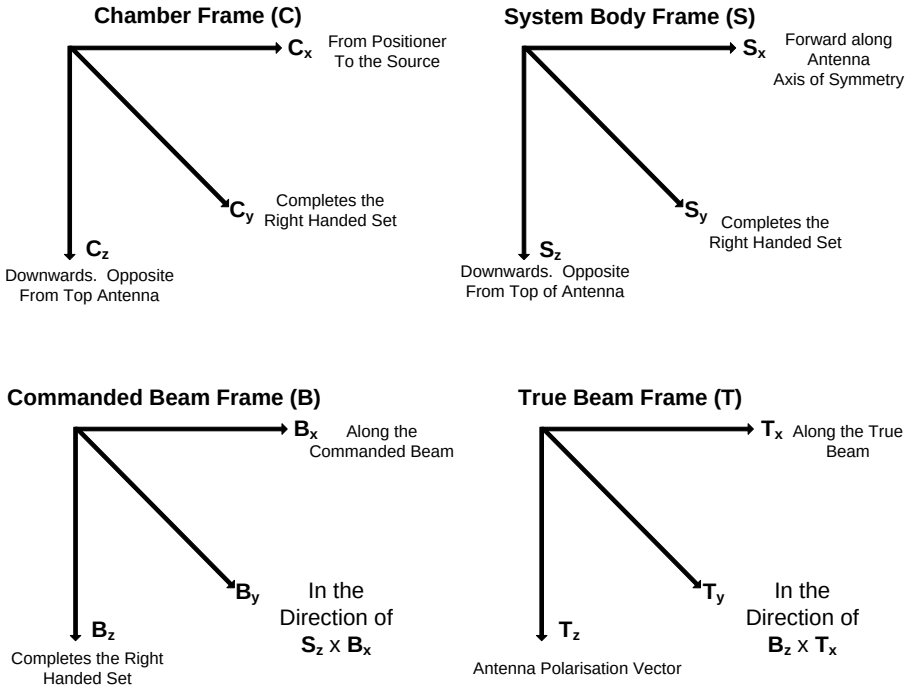

Figure 4.1: Top left: Chamber co-ordinate frame (C) definition. Top right: System body co-ordinate frame (S) definition. Bottom left: Commanded Beam co-ordinate frame (B) definition. Bottom right: True beam co-ordinate frame (T) definition.

Directional cosine matrices can be defined to describe a change between the co-ordinate

frames. The directional cosine matrices will operate on a column vector, which defines a position in one co-ordinate frame, and transform it to another co-ordinate frame. A column vector in the C frame ($\mathbf{v_C}$) under the matrix transformation from the C to the S Frame (**CToS**) will describe a vector in the S frame ($\mathbf{v_S}$) given by Equation (4.1).

$$\mathbf{v}_S = \mathbf{CToS} \cdot \mathbf{v}_C \tag{4.1}$$

Similar Matrices are defined to describe transformations between all co-ordinate frames, Equations (4.2), (4.3), (4.4), (4.5), where ^{T} denotes the transpose of the matrix and:

- The Euler angles in the C frame to the S frame matrix, **CToS.**
- The Euler angles in the S frame to the B frame matrix, **SToB.**
- The Euler angles in the B frame to the T frame matrix, **BToT.**
- The Euler angles in the T frame to the C frame matrix, **TToC.**

$$\mathbf{CToS} = \mathbf{SToC}^T \tag{4.2}$$

$$\mathbf{SToB} = \mathbf{BToS}^T \tag{4.3}$$

$$\mathbf{BToT} = \mathbf{TToB}^T \tag{4.4}$$

$$\mathbf{TToC} = \mathbf{CToT}^T \tag{4.5}$$

These will be combined into a single definition of the total required AT.

4.3 CALCULATION OF THE AXIS TRANSFORM

To determine a vector in the T frame, ($\mathbf{v_T}$), when it is known in the C frame then matrix definitions presented have to be combined, Equation (4.6).

$$\mathbf{CToB} = \mathbf{SToB} \cdot \mathbf{CToS} \tag{4.6}$$

Equations (4.6) and (4.4) can be multiplied together so the computation is completed in one step, Equation (4.7).

$$\mathbf{v_T} = \mathbf{BToT} \cdot \mathbf{CToB} \cdot \mathbf{v_C} \tag{4.7}$$

Euler angles are a set of three angles that describe the orientation of a rigid body [74]. The sequence of the implementation of the Euler angle is defined as 321. Therefore the third element is implemented first, i.e. ψ which is a rotation around the z axis. Then θ, a rotation around the y axis, is implemented second. Finally, ϕ, a rotation around the x axis, is implemented last. The orientation of the position within the reference frame is described by *Euler 321 angles* as shown by Equation (4.8) [75].

$$\textit{Euler 321 Angle} = \phi \quad \theta \quad \psi \tag{4.8}$$

4.3.1 CALCULATION OF GENERAL TRANSFORMATION MATRIX

A general transformation matrix to take a vector from one co-ordinate frame to another will be defined. As an example, the matrix transform for **CToS** will be calculated, but it will form the general case for **SToB**, **BToT** and **TToC**.

First the general AZ component of rotation will be defined. This is represented by a small arbitrary rotation of the co-ordinate frame x, y, z around the z axis by an angle ψ to form the x', y', z' axis set, Fig. 4.2. This rotation is represented by the AT matrix shown in Equation (4.9).

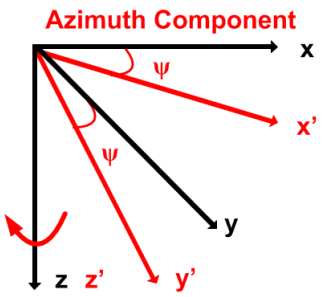

Figure 4.2: The AZ component of rotation for a small arbitrary rotation around the z axis.

$$\mathbf{CToS}_{\psi} = \begin{bmatrix} \cos\psi & \sin\psi & 0 \\ -\sin\psi & \cos\psi & 0 \\ 0 & 0 & 1 \end{bmatrix} \tag{4.9}$$

Similarly the general EL component of rotation will be defined. This is represented by a small rotation of the co-ordinate frame x, y, z around the y axis by an angle θ to form the x', y', z' axis set, Fig. 4.3. This rotation is represented by the AT matrix shown by Equation (4.10).

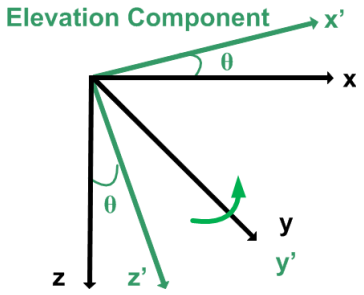

Figure 4.3: The EL component of rotation for a small arbitrary rotation around the y axis.

$$\mathbf{CToS}_{\theta} = \begin{bmatrix} \cos\theta & 0 & -\sin\theta \\ 0 & 1 & 0 \\ \sin\theta & 0 & \cos\theta \end{bmatrix} \tag{4.10}$$

Finally, the general ROLL component of rotation is represented by a small rotation of the co-ordinate frame x, y, z around the x axis by an angle ϕ to form the x', y', z' axis set, Fig. 4.4. This rotation is represented by the AT matrix, Equation (4.11).

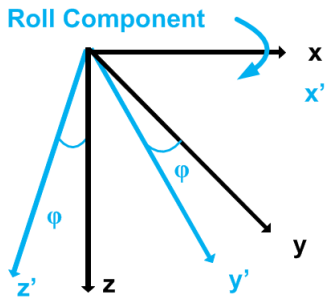

Figure 4.4: The ROLL component of rotation for a small arbitrary rotation around the x axis.

$$\mathbf{CToS}_{\phi} = \begin{bmatrix} 1 & 0 & 0 \\ 0 & \cos\phi & \sin\phi \\ 0 & -\sin\phi & \cos\phi \end{bmatrix} \tag{4.11}$$

Equations (4.9), (4.10), (4.11) are combined to calculate the full **CToS** matrix, comprising of the three movements in AZ, EL and ROLL as shown by Equation (4.12). The general case matrix follows this multiplication as shown by Equation (4.13). These will be shown for the example of **CToS**, which shows the general case and is applicable to any of the ATs previously defined.

$$\mathbf{CToS} = \mathbf{CToS}_{\phi} \cdot \mathbf{CToS}_{\theta} \cdot \mathbf{CToS}_{\psi} \tag{4.12}$$

$$\mathbf{CToS} = \begin{bmatrix} cos\theta\ cos\psi & cos\theta\ sin\psi & -sin\theta \\ -cos\phi\ sin\psi + sin\phi\ sin\theta\ cos\psi & cos\phi\ cos\psi + sin\phi\ sin\theta\ sin\psi & sin\phi\ cos\theta \\ sin\psi\ sin\phi + cos\phi\ sin\theta\ cos\psi & -sin\phi\ cos\psi + cos\phi\ sin\theta\ sin\psi & cos\phi\ cos\theta \end{bmatrix} \tag{4.13}$$

We can now solve for ψ, θ and ϕ. The following process uses standard matrix element notation, $\mathbf{M_{ij}}$, where $_{\mathbf{i}}$ is the row number and $_{\mathbf{j}}$ the column number.

Using Equation (4.13) θ can be calculated as shown by Equation (4.14).

$$\theta = \sin^{-1}\ (-\ \mathbf{CToS_{13}}) \tag{4.14}$$

Equation (4.14) shows that θ cannot equal $\pm\ 90^{o}$ as there would be no unique solution at

this point. This limitation of the AT will not be removed as the mechanical EL limit of the positioner is $\pm\ 60^o$ thus preventing this from occurring.

Using the Tangent identity function shown in Equation (4.15), where α is an angle in a right angled triangle, ϕ can be calculated from Equation (4.13) as shown by Equation (4.16).

$$\tan\ \alpha = \frac{\sin\ \alpha}{\cos\ \alpha} \tag{4.15}$$

$$\phi = \tan^{-1}\ \frac{\mathbf{CToS_{23}}}{\mathbf{CToS_{33}}} \tag{4.16}$$

Similarly ψ can be calculated from Equation (4.13), and the identity shown in Equation (4.15), as shown in Equation (4.17).

$$\psi = \tan^{-1}\ \frac{\mathbf{CToS_{12}}}{\mathbf{CToS_{11}}} \tag{4.17}$$

The final stage is to tie in the defined movement of the different co-ordinate frames to that of the Euler definitions.

Uniquely the movement of the positioner in each axis is defined, Fig. 4.5, so the AT can be calculated.

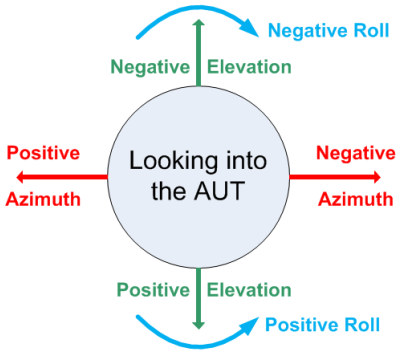

Figure 4.5: Defined movements of the positioner.

The movement in the **CToS** frame is defined in terms of the Euler definitions, Fig. 4.6. This can be used to define the transformation from the Euler angles in **CToS** to the movement on the positioner, *Positioner Angles*, Equations (4.18), (4.19), (4.20).

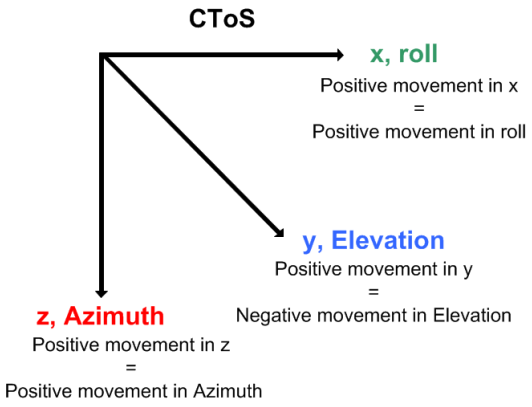

Figure 4.6: **CToS** frame Euler definition.

$$\psi_{CToS} = Positioner_{AZ} \tag{4.18}$$

$$\theta_{CToS} = -Positioner_{EL} \tag{4.19}$$

$$\phi_{CToS} = Positioner_{ROLL} \tag{4.20}$$

The movement in the **SToB** frame is defined in terms of the Euler definitions, Fig. 4.7. This can be used to define the transformation from the Euler angles in **SToB** to the movement in the S frame, i.e. *System Angles*, as shown by Equations (4.21), (4.22), (4.23).

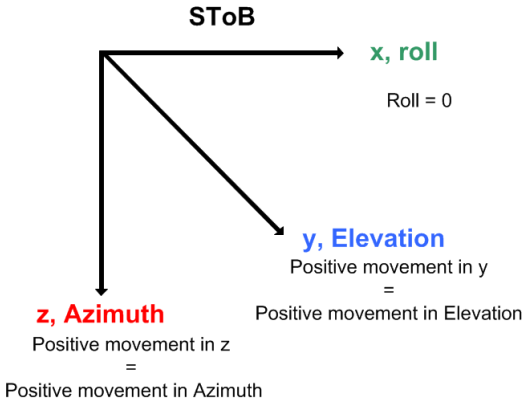

Figure 4.7: **SToB** frame Euler definition.

$$\psi_{SToB} = System_{AZ} \tag{4.21}$$

$$\theta_{SToB} = System_{EL} \tag{4.22}$$

$$\phi_{SToB} = 0 \tag{4.23}$$

The transformation from the Euler angles in **BToT**, as shown in Fig. 4.8, to the angles defined in the B frame, i.e. *Aberration Angles*, is shown by Equations (4.24), (4.25), (4.26). This stage of the AT is novel as it allows for the inclusion or the measurement of the *Aberration Angles* as an integral part of the measurement procedure. The *Aberration Angles* can be included if known by measurement or simulation, or set to 0 to allow measurement of the angles or if a radome is not present.

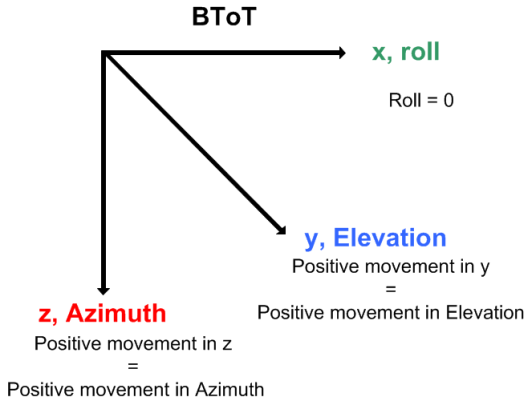

Figure 4.8: **BToT** frame Euler definition.

$$\psi_{BToT} = Aberration_{AZ} \tag{4.24}$$

$$\theta_{BToT} = Aberration_{EL} \tag{4.25}$$

$$\phi_{BToT} = 0 \tag{4.26}$$

The transformation from the Euler angles in **TToC** to the angles defined in the T frame, i.e. *Target Angles*, are shown in Fig. 4.9 and Equations (4.27), (4.28), (4.29). These angles define where we want the target in the beam. For example when taking an antenna pattern we want to move the target through the beam to create this pattern. If the pattern is to

start at -30^o, then the *Target Angle* is -30^o at this point.

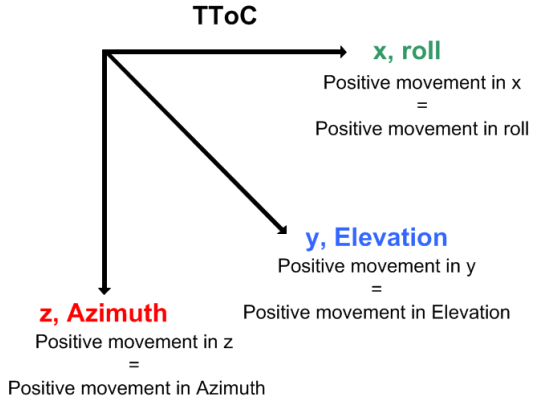

Figure 4.9: **TToC** frame Euler definition.

$$\psi_{TToC} = Target_{AZ} \tag{4.27}$$

$$\theta_{TToC} = Target_{EL} \tag{4.28}$$

$$\phi_{TToC} = Target_{ROLL} \tag{4.29}$$

The described Euler angles and matrix transformations can now be combined together to describe different types of movement. The AT will be validated firstly by simulation.

4.4 CONFIRMATION OF THE AXIS TRANSFORM

To assess the outcome of the AT the signals resulting from the ΔAZ divided by the Σ beams ($\Delta AZ/\Sigma$) for an EL cut will be assessed. These values are expected to be zero for a cut in the T frame across the 3 dB beam width of the main beam.

This will be confirmed in simulation, stand-alone positioner test and AC measurements.

4.4.1 SIMULATION TEST OF THE AXIS TRANSFORM

In order to verify the AT, a MATLAB simulation was set up. The simulation creates a monopulse antenna beam, moves this beam through an EL antenna cut as described by

the AT, and then constructs the $\Delta AZ/\Sigma$ as a function of EL angle. The following steps are then taken in order to point the positioner to a specific position in the T frame:

- The required *System Angles* are chosen. This allows **SToB** to be calculated.
- The *Aberration Angles* are set to 0, as there is no radome in this simulation. This allows **BToT** to be calculated.
- The *Target Angles* are AZ = EL = ROLL = 0^o, as we require the target to be in the centre of the beam frame. This allows **TToC** to be calculated.
- From the above three definitions and Equations (4.13) to (4.29), the *Positioner Angles* can be calculated, Equation (4.30).

$$\mathbf{CToS} = \mathbf{SToB}^{\mathbf{T}} \cdot \mathbf{BToT}^{\mathbf{T}} \cdot \mathbf{TToC}^{\mathbf{T}} \tag{4.30}$$

4.4.1.1 SIMULATION OF AXIS TRANSFORM RESULTS

The results presented are the cuts in EL and are taken at a starting position of all permutations of 0^o and 20^o, Table 4-A.

AZ START POSITION (^{o})	**EL START POSITION (^{o})**
0	0
20	0
-20	0
0	20
0	-20
20	20
-20	-20
-20	20
20	-20

Table 4-A: Start angles for AT simulation.

With and without the AT $\Delta AZ/\Sigma$ is zero for a cut starting at positions of [AZ, EL]^o, [0, 0]^o, [0, 20]^o and [0, -20]^o. This is as expected for this positioner at a starting angle of 0^o in AZ.

Fig. 4.10 shows that without the AT $\Delta AZ/\Sigma$ becomes non-zero for a cut starting at an AZ and EL angle of [20, 0]^o and [-20, 0]^o. It can be seen that starting at a non-zero AZ angle and conducting an EL cut results in the incorrect movement of the beam if an AT is not used. It can be seen that the $\Delta AZ/\Sigma$ is zero when the AT is applied. The maximum deviation from $\Delta AZ/\Sigma = 0$ for both cuts is 0.011, and the RMS value is 0.006. This level of deviation will be difficult to detect in measurements.

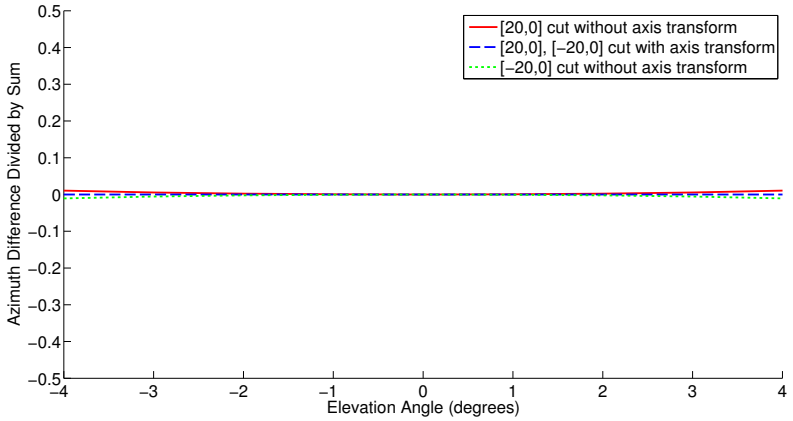

Figure 4.10: Simulated $\Delta AZ/\Sigma$ with and without an AT EL cut at [20, 0]^o and [-20, 0]^o.

Figs. 4.11 and 4.12 show that without the AT $\Delta AZ/\Sigma$ is non-zero for a cut starting at compound angles of [20, 20]^o, [20, -20]^o, [-20, 20]^o and [-20, -20]^o. It can be seen that starting at a compound angle and conducting an EL cut results in the incorrect movement of the beam if an AT is not used. It can be seen that the $\Delta AZ/\Sigma$ is zero when the AT is applied. The maximum deviation from $\Delta AZ/\Sigma = 0$ for all cuts is 0.351, and the RMS value is 0.243.

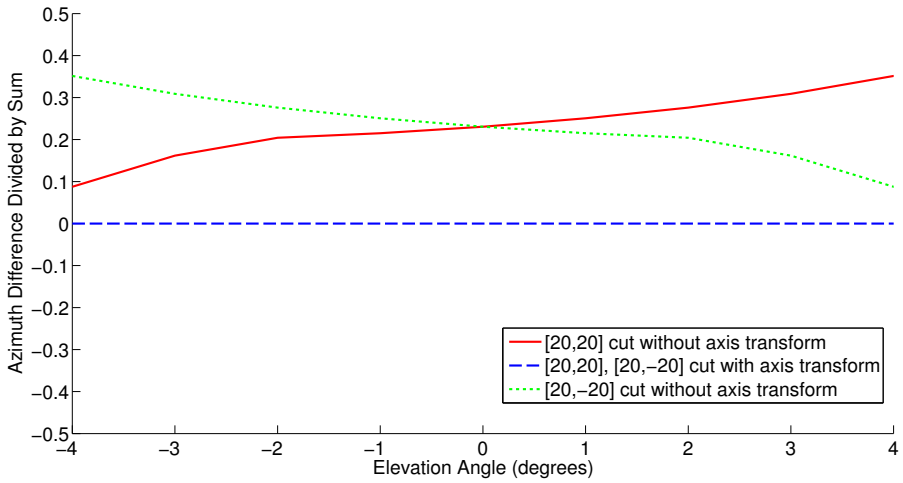

Figure 4.11: Simulated $\Delta AZ/\Sigma$ for an AT corrected and un-corrected EL cut at [20, 20]^o and [20, -20]^o.

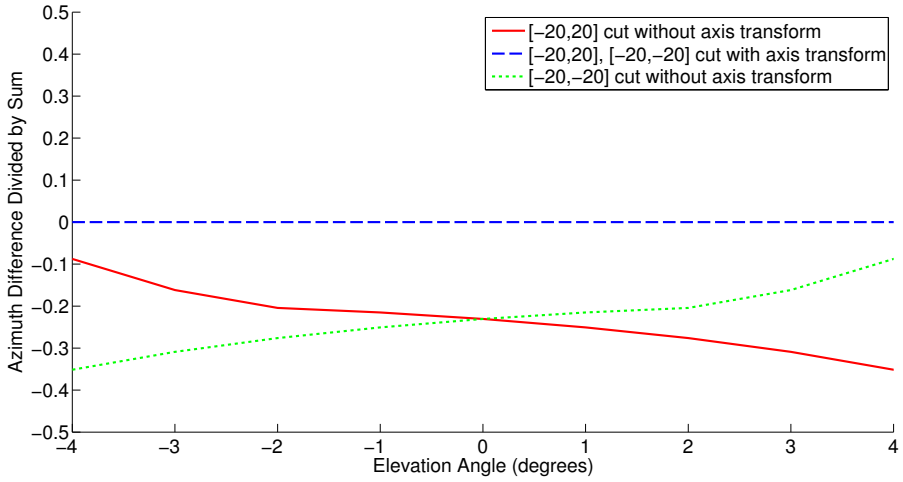

Figure 4.12: Simulated $\Delta AZ/\Sigma$ for an AT corrected and un-corrected EL cut at [-20, 20]^o and [-20, -20]^o.

In addition the $\Delta EL/\Sigma$ cuts for an AZ antenna cut will be considered to check the full working of the AT before it is integrated into a moving system.

With and without the AT $\Delta EL/\Sigma = 0$ for an AZ cut starting at AZ and EL angles of [0, 0]^o, [0, 20]^o, [0, -20]^o, [20, 0]^o and [-20, 0]^o. This is as expected because the movement is in the principal planes the axis frames are lined up.

Figs. 4.13 and 4.14 shows that without the AT $\Delta EL/\Sigma$ is non-zero for a cut starting at compound angles of [20, 20]^o, [20, -20]^o, [-20, 20]^o and [-20, -20]^o. It can be seen that starting at a compound angle and conducting an AZ cut results in the incorrect movement of the beam if an AT is not used. It can be seen that the $\Delta EL/\Sigma$ is zero when the AT is applied. The maximum deviation of $\Delta EL/\Sigma$ from 0 for all cuts is 0.351, and the RMS value is 0.243. These are the same values as measured with the $\Delta AZ/\Sigma$ cuts.

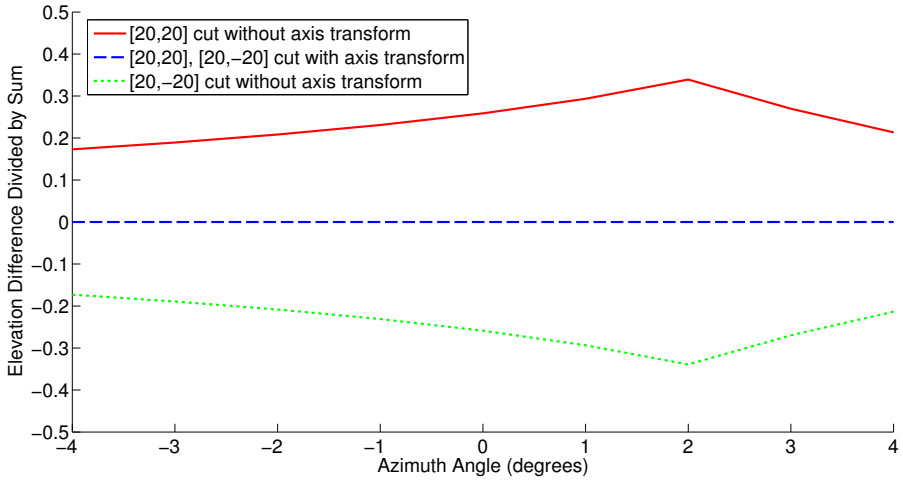

Figure 4.13: Simulated $\Delta EL/\Sigma$ for an AT corrected and un-corrected AZ cut at [20, 20]^o and [20, -20]^o.

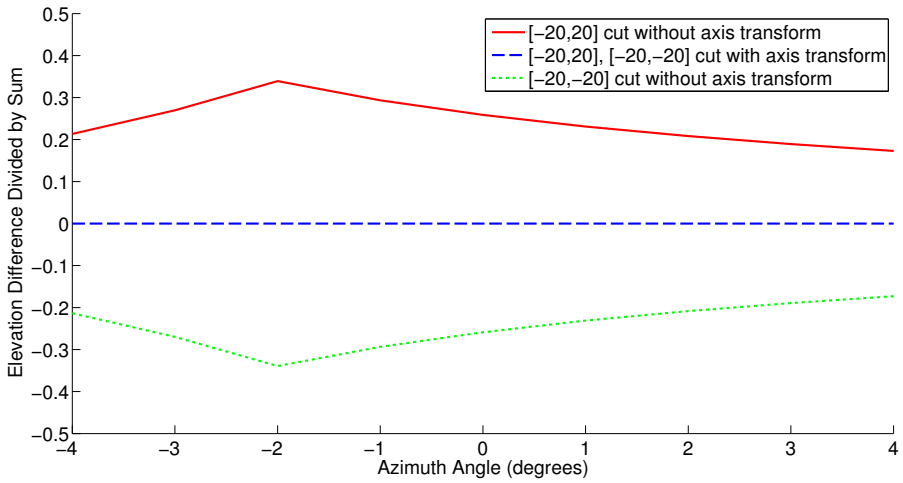

Figure 4.14: Simulated $\Delta EL/\Sigma$ for an AT corrected and un-corrected AZ cut at [-20, 20]^o and [-20, -20]^o.

Table 4-B summarises these resuts and shows that the AT works as expected for this simulated test, the AT will now be tested by a model of the positioner.

POSITION (^{o})	**ΔAZ/Σ MAX NO AT**	**ΔAZ/Σ RMS NO AT**	**ΔEL/Σ MAX NO AT**	**ΔEL/Σ RMS NO AT**	**ΔAZ/Σ MAX AT**	**ΔEL/Σ MAX AT**
[0, 0]	0	0	0	0	0	0
[0, 20]	0	0	0	0	0	0
[0, -20]	0	0	0	0	0	0
[20, 0]	0.011	0.006	0	0	0	0
[-20, 0]	0.011	0.006	0	0	0	0
[20, 20]	0.351	0.243	0.351	0.243	0	0
[20, -20]	0.351	0.243	0.351	0.243	0	0
[-20, -20]	0.351	0.243	0.351	0.243	0	0
[-20, 20]	0.351	0.243	0.351	0.243	0	0

Table 4-B: Maximum offset from $\Delta AZ/\Sigma = 0$ and $\Delta EL/\Sigma$ or RMS values for the different start angles for an EL and AZ cut in simulation with and without the AT.

4.4.2 LEGO NXT POSITIONER TEST OF THE AXIS TRANSFORM

LEGO NXT was used for the development and test of the AT control code for the AC positioner. A scale model of the positioner found in the AC was built, Fig. 4.15. The centre of rotation of all 3 axes occurs in the same place, and the axes move in the same orientation as the AC positioner. The **E** vector of the antenna mounted on the positioner is shown by the yellow rod. An antenna with 2 degrees of freedom has been put on the front of the positioner, this will allow investigation into the articulated nature of a TRMAS, Fig. 4.16.

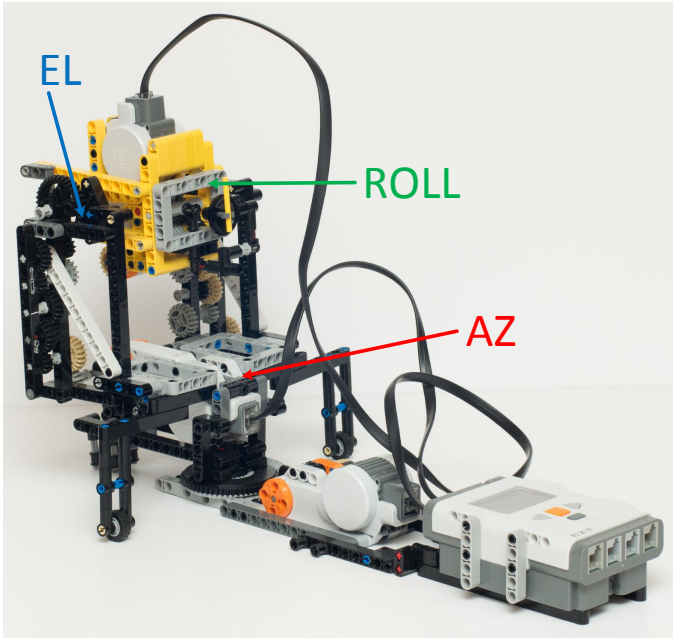

Figure 4.15: LEGO NXT positioner

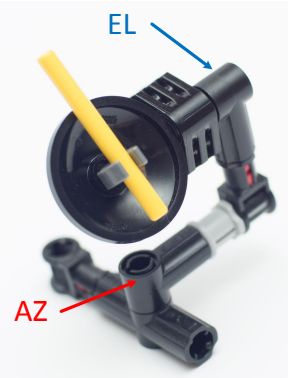

Figure 4.16: Close up of the 2 axis antenna mounted on the positioner.

4.4.2.1 SINGLE POSITION WITH AXIS TRANSFORM ON LEGO NXT

The control code for the LEGO NXT positioner was written in MATLAB. This initialised the motors and moved the axes according to the input position. The AT was included in the code, so the positioner could move according to the C or T frames of reference.

This work will investigate different scan angles of the TRMAS. Therefore, when moving to a specific position the pointing of the TRMAS has to be adjusted to account for the movement of the positioner to keep the beam pointing in the correct direction. If the positioner is moved to [30, 30]^o then the antenna has to be moved to [-30, -30]^o to compensate for this movement and to align the beam back to the target. As the positioner is moved we are concerned about the pointing of the E vector.

The LEGO positioner was moved to [0, 0]^o in the C frame, then to [0, 0]^o in the T beam frame, Fig. 4.17. As expected these result in the positioner remaining in the same place.

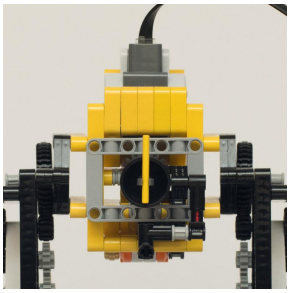

Figure 4.17: The LEGO positioner and AUT at $[0, 0]^o$.

At positions where either the AZ or EL remains on the principal plane, it is expected that there will be no difference between the positions of the positioner in the two frames. To test this the positioner was moved to $[40, 0]^o$ and the antenna moved to $[-40, 0]^o$ in the C then the T frame. This was then repeated at $[-40, 0]^o$, $[0, 40]^o$ and $[0, -40]^o$, Fig. 4.18. It was seen that with or without the AT the positioner was sent to the same location.

At compound angles a difference in position between the two frames emerges. As an example the positioner was moved to $[-40, 40]^o$ and the antenna moved to $[40, -40]^o$ in the C frame. The positioner was then moved to $[-40, 40]^o$ and the antenna moved to $[40, -40]^o$ in the T frame, a position of $[47.61, 29.50, 28.34]^o$ in *Positioner Angles*, Fig. 4.19. It can be seen that without the AT the **E** vector is rotated, with the AT it remains vertical. Table 4-C summarises results from all positions.

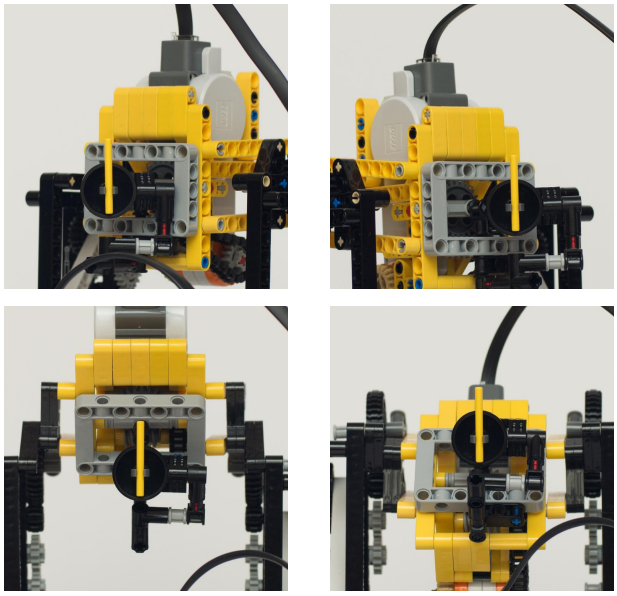

Figure 4.18: Top left image: LEGO positioner at [40, 0]^o and the AUT moved to [-40, 0]^o. Top right image: LEGO positioner at [-40, 0]^o and the AUT moved to [40, 0]^o. Bottom left image: LEGO positioner at [0, 40]^o and the AUT moved to [0, -40]^o. Bottom right image: LEGO positioner at [0, -40]^o and the AUT moved to [0, 40]^o.

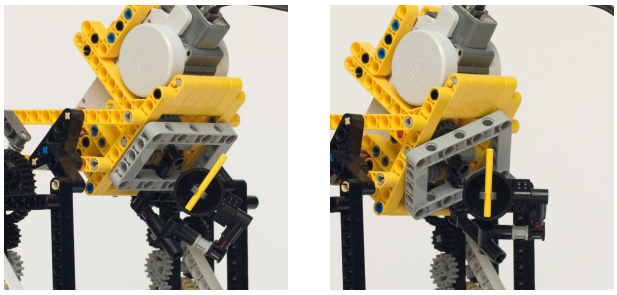

Figure 4.19: Left image: LEGO positioner at [-40, 40]^o and AUT at [40, -40]^o in the C frame. Right image: LEGO positioner at [-40, 40]^o and the AUT at [40, -40]^o in the T frame.

POSITION (^{o})	**NO AT E VECTOR VERTICAL?**	**AT E VECTOR VERTICAL?**
[0, 0]	yes	yes
[0, 40]	yes	yes
[0, -40]	yes	yes
[40, 0]	yes	yes
[-40, 0]	yes	yes
[40, 40]	no	yes
[40, -40]	no	yes
[-40, -40]	no	yes
[-40, 40]	no	yes

Table 4-C: Truth table for the results of the position of the E vector at positions on the LEGO NXT positioner with and without the AT.

4.4.2.2 ANTENNA PATTERN CUT WITH AT ON LEGO NXT

An antenna cut starting at [0, 0]^o and moving in the principal planes does not require an AT as the **E** vector remains vertical.

However, at other starting angles, a difference between the positions of the positioner in the two frames is seen. Only the movement with the AT included will keep the **E** vector vertical. To test this the positioner was moved to [-40, 40]^o and the antenna to [40, -40]^o in the C then the T frame. An antenna cut was carried out, with and without the AT, moving in EL in 20^o steps, Fig. 4.20. As expected in all cases the **E** vector remains vertical for the T frame cut, but a movement occurs for the C frame cut. Table 4-D summarises results from cuts starting at all positions.

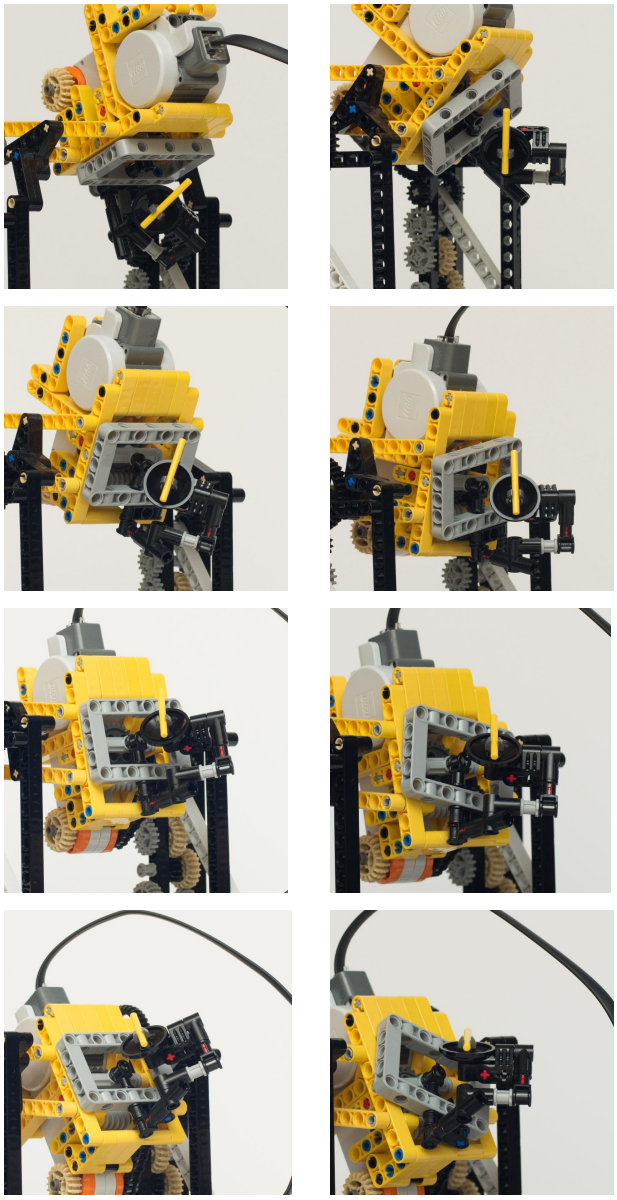

Figure 4.20: Antenna cut being performed at a start angle of [-40, 40]^o with the AUT moved to [40, -40]^o. Left column: C frame. Right column: T frame. First row: +20^o in EL from the start EL point. Second row: -20^o in EL from the start EL point. Third row: -60^o in EL from the start EL point. Fourth row: -80^o in EL from the start EL point.

POSITION (^{o})	**NO AT E VECTOR VERTICAL? AZ CUT**	**AT E VECTOR VERTICAL? AZ CUT**	**NO AT E VECTOR VERTICAL? EL CUT**	**AT VECTOR VERTICAL? EL CUT**
[0, 0]	yes	yes	yes	yes
[0, 40]	yes	yes	yes	yes
[0, -40]	yes	yes	yes	yes
[40, 0]	yes	yes	no	yes
[-40, 0]	yes	yes	no	yes
[40, 40]	no	yes	no	yes
[40, -40]	no	yes	no	yes
[-40, -40]	no	yes	no	yes
[-40, 40]	no	yes	no	yes

Table 4-D: Truth table for the results of the position of the E vector for antenna cuts on the LEGO NXT positioner with and without the AT.

It can be clearly seen that the cuts taken without the AT rotate the **E** vector, the cuts taken with the AT keep the **E** vector vertical giving a visual proof of the AT. What is also noticeable is that the position of the roll ring is aligned with the **E** vector, so with or without the movement of the antenna the **E** vector remains vertical, Fig. 4.21. The **E** vector has to remain vertical, as this is the purpose of the AT. The EL axis of the TRMAS is defined by being horizontal and perpendicular to the beam. Therefore if the TRMAS is moved to $[0, 0]^o$ the **E** vector has to be parallel to a vertical line on the roll ring. This means that the TRMAS does not have to be included on the positioner to visually show the AT. This removes one more stage and thus helps with the accuracy of the test.

The AT will now be visually tested in the AC.

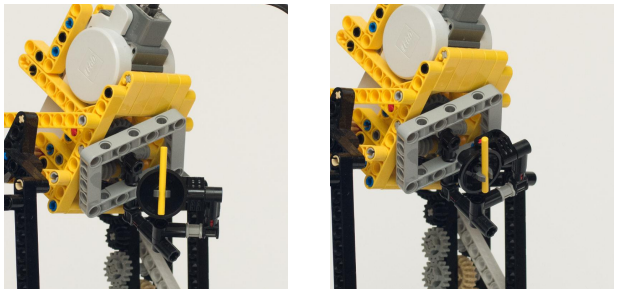

Figure 4.21: Left image: positioner at [-40, 40]^o in the T frame with movement of the AUT at [40, -40]^o. Right image: positioner at [-40, 40]^o in the T frame without movement of the antenna.

4.4.3 AC POSITIONER TEST OF AXIS TRANSFORM

4.4.3.1 SINGLE POSITION WITH THE AT ON THE AC POSITIONER

The AT was tested in the AC. The AT was added to the custom written MATLAB scripts to allow the positioner to move in the T frame, rather than the C frame. To show the position of the **E** vector a strip of red tape was stuck to the roll ring so that it is vertical when the positioner is at [0, 0]^o. The **E** vector of the antenna cannot be clearly seen in these photographs as it is too small. If, as on the LEGO positioner, a representative antenna is used with large **E** vectors that can be seen in a picture the movement of the positioner is limited by how far this antenna can move.

As the code to calculate the new angle is written in MATLAB using double-precision floating point numbers to 17 decimal places, the accuracy of this result is not considered to be a source of error. The accuracy of the AZ axis is $\pm$ 0.03^o, EL $\pm$ 0.04^o and ROLL $\pm$ 0.1^o therefore the maximum offset of the positioner from the expected position is 0.11^o. As measurements are taken in 1^o steps the expected error is an order of magnitude lower.

The positioner was moved to [0, 0]^o in the C beam frame, then to [0, 0]^o in the T beam frame, Fig. 4.22. As expected these result in the positioner remaining in the same place.

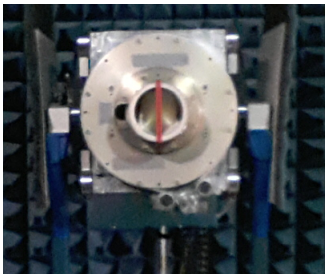

Figure 4.22: Positioner at $[0, 0]^o$ in the C and T beam frames.

At positions where either the AZ or EL remains on the principal plane, the position remains the same with or without the AT, as shown in Fig. 4.23.

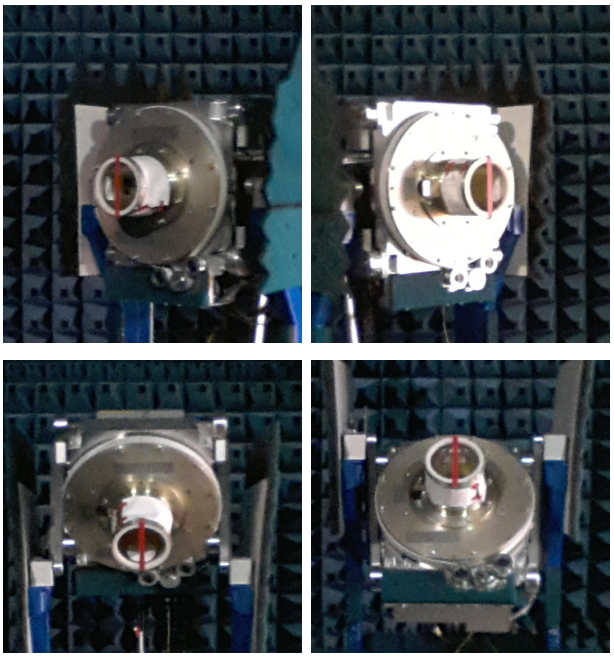

Figure 4.23: Top left image: positioner at $[40, 0]^o$. Top right image: positioner at $[-40, 0]^o$. Bottom left image: positioner at $[0, 40]^o$. Bottom right image: positioner at $[0, -40]^o$.

At compound angles a difference in position between the two frames is seen. Again, the AT correctly places the beam of the antenna as shown in Fig. 4.24. The same truth table is constructed as that shown for the LEGO NXT positioner, Table 4-C.

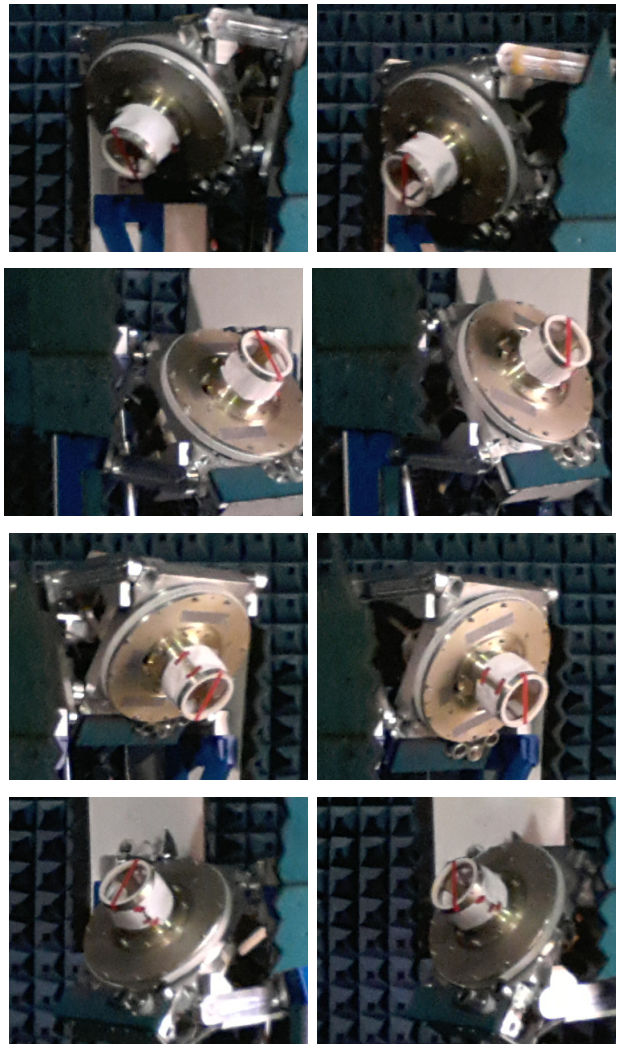

Figure 4.24: Left column: C frame. Right column: T frame. First row: positioner at [40, 40]^o. Second row: positioner at [-40, -40]^o. Third row: positioner at [-40, 40]^o. Fourth row: positioner at [40, -40]^o.

4.4.3.2 ANTENNA PATTERN CUT WITH THE AXIS TRANSFORM ON THE ANECHOIC CHAMBER POSITIONER

Fig. 4.25 shows an EL antenna cut carried out on the positioner. As expected in all cases the **E** vector remains vertical for the T frame cut, but a rotation occurs for the C frame cut. The same is seen for cuts in AZ at [20, 20]^o, AZ and EL cuts at [-20, -20]^o, [-20, 20]^o and [20, -20]^o.

This gives visual proof of the AT working. A more quantitative proof will be shown in

the following section looking at the results of testing a TRMAS on the positioner. This gives the same truth table for the antenna cut as found on the LEGO NXT positioner, Table 4-D .

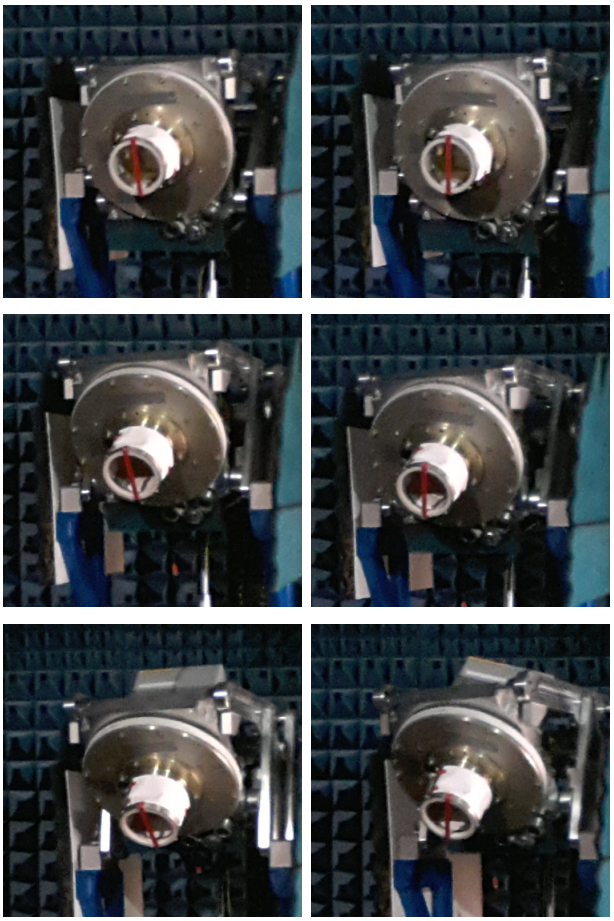

Figure 4.25: Antenna cut being performed at a start angle of [20, 20]^o. Left column: C frame. Right column: T frame. First row: start of the antenna pattern, [20, 20]^o. Second row: + 15^o in EL from the start EL point. Third row: +30^o in El from the start EL point.

4.5 AC POSITIONER TEST OF AN ANTENNA CUT

4.5.1 RESULTS OF ANTENNA CUT WITH AXIS TRANSFORM

4.5.1.1 ELEVATION CUTS

To test the validity of the AT in a measurement system the AT, with known radome *Aberration Angles*, was added to the custom written MATLAB script which controls the movement of the positioner and the control and measurement of the TRMAS in the AC. Measurement procedure is to the move the positioner to the start position of the cut, e.g. $[20, 20]^o$, move the TRMAS to the negative of this position so it points to boresight, [-20, -20]^o and then perform a $\pm\ 4^o$ cut in AZ moving only the positioner. It is not expected that the $\Delta AZ/\Sigma$ will be reduced to exactly 0 for real measurements with an AUT as was seen in the simulation. The simulation gives a perfect environment devoid of measurement error, with the quadrants of the TRMAS being exactly equal. This is not the case when testing real hardware in an AC. To quantify the offset from $\Delta AZ/\Sigma = 0$ a cut was conducted at $[0, 0]^o$, the maximum offset and the RMS error was calculated, Fig. 4.26.

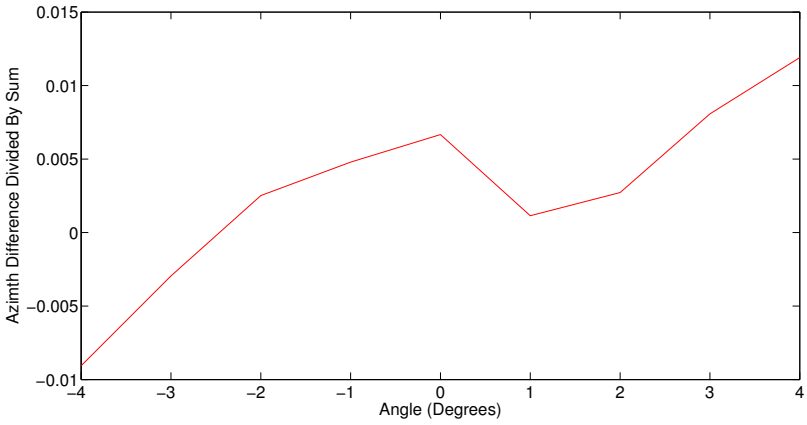

Figure 4.26: Measured $\Delta AZ/\Sigma$ for an AT corrected EL cut $[0, 0]^o$.

Calculations on the data used to construct Fig. 4.26 show that the maximum offset from $\Delta AZ/\Sigma = 0$ is 0.012 and the RMS value is 0.007, quantifies the errors in the AC at $[0, 0]^o$.

Results in Figs. 4.27 and 4.28 show the comparison of $\Delta AZ/\Sigma$ for results with no AT and those with the AT and radome *Aberration Angles* for cuts completed at the starting angles of [20, 20]^o, [20, -20]^o, [-20, -20]^o, [-20, 20]^o.

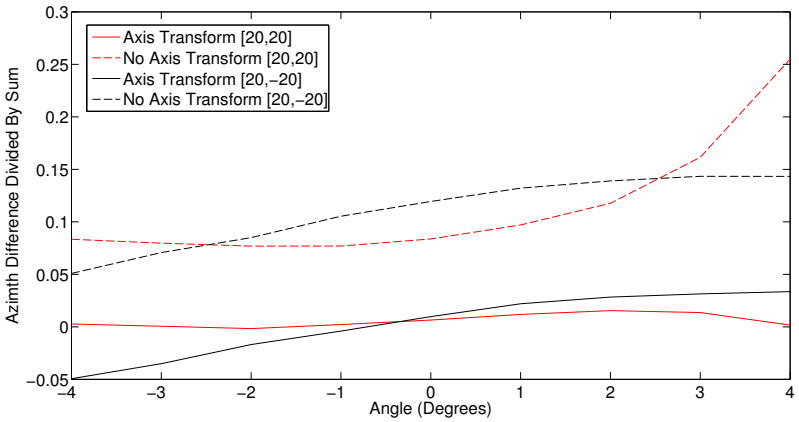

Figure 4.27: Measured $\Delta AZ/\Sigma$ with and without AT EL cut at [20, 20]^o and [20, -20]^o.

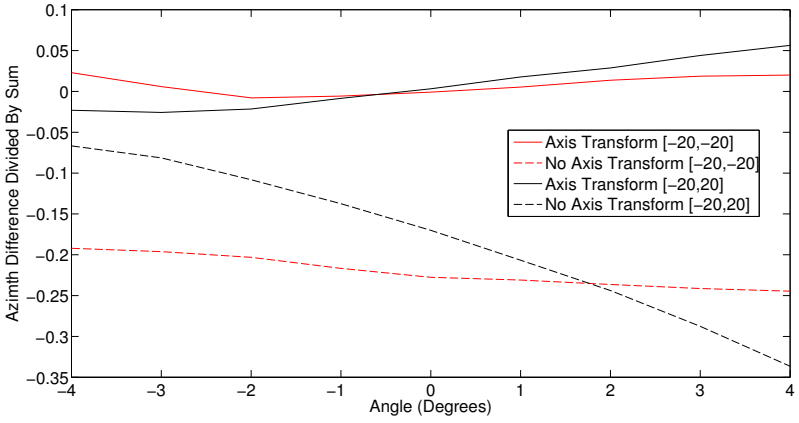

Figure 4.28: Measured $\Delta AZ/\Sigma$ with and without AT EL at [-20, -20]^o, [-20, 20]^o.

It can be seen that the cuts are significantly improved by the AT and the $\Delta AZ/\Sigma$ is reduced to approach 0 as expected for a validated AT. Results for all EL cuts taken are shown in Table 4-E.

POSITION (^{o})	NON-AT MAX	AT MAX	NON-AT RMS	AT RMS
[**0, 0**]	0.012		0.007	
[**0, 20**]	0.022		0.012	
[**0, -20**]	0.020		0.009	
[**20, 0**]	0.102	0.017	0.092	0.011
[**-20, 0**]	0.106	0.006	0.089	0.004
[**20, 20**]	0.255	0.016	0.128	0.008
[**20, -20**]	0.143	0.050	0.115	0.029
[**-20, -20**]	0.245	0.023	0.222	0.013
[**-20, 20**]	0.481	0.056	0.289	0.030

Table 4-E: Maximum offset from 0 and RMS values for the $\Delta AZ/\Sigma$ at different start angles for an EL cut on the positioner.

4.5.1.2 AZIMUTH CUTS

The same pattern can be seen in the AZ cuts. The cuts are significantly improved by the AT and the $\Delta EL/\Sigma$ is reduced to approach 0 as expected for a validated AT. An example plot is shown in Fig. 4.29. All results for AZ cuts taken are shown in Table 4-F.

POSITION (^{o})	NON-AT MAX	AT MAX	NON-AT RMS	AT RMS
[**0, 0**]	0.017		0.011	
[**0, 20**]	0.011		0.060	
[**0, -20**]	0.019		0.010	
[**20, 0**]	0.014		0.011	
[**-20, 0**]	0.024		0.013	
[**20, 20**]	0.250	0.053	0.240	0.025
[**20, -20**]	0.237	0.043	0.177	0.027
[**-20, -20**]	0.183	0.057	0.157	0.030
[**-20, 20**]	0.276	0.046	0.225	0.003

Table 4-F: Maximum offset from 0 and RMS values for the $\Delta EL/\Sigma$ at different start angles for an AZ cut on the positioner.

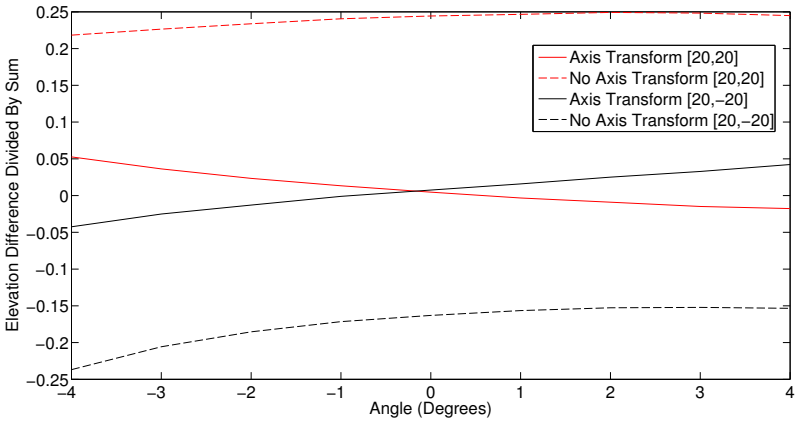

Figure 4.29: Measured $\Delta EL/\Sigma$ with and without AT AZ cut at [20, 20]^o and [20, -20]^o.

4.5.2 RESULTS OF ANTENNA CUT WITH ABERRATION ANGLES

4.5.2.1 ELEVATION CUTS

The aberration caused by inclusion of the radome can be measured using the AT. The initial value of the *Aberration Angle* are set to [0, 0]^o. The positioner is moved to the start position with the AT, [X, Y]^o, and the 4 channels of the TRMAS measured. An automatic search is conducted for the peak of the beam. This is valid for $\Delta AZ/\Sigma$ or $\Delta EL/\Sigma$. The peak of the beam is automatically found by moving the TRMAS such that the Δ/Σ value becomes 0, as expected when at the peak of the beam. To convert the Δ/Σ into an angular distance it is divided by the *Tracking Slope*, Equation (4.31).

$$Angular\ Error = \frac{\frac{\Delta}{\Sigma}}{Tracking\ Slope} \tag{4.31}$$

When this calculation has been completed once a value for the aberration has been calculated. The positioner is now moved to [X + AZ *Aberration Angle*, Y + EL *Aberration Angle*]^o and the measurement completed again, Equation (4.32). It is likely that a few iterations of this process will have to be undertaken until the value of the Δ/Σ slope approaches 0, it is unlikely that the Δ/Σ will measure exactly 0. The true *Aberration Angles* are calculated from this process. The tolerance on this value will have to be

determined by the system as an allowable *Angular Error* in the value of the boresight.

$$Aberration\ Angle = Angular\ Error + Previous\ Aberration\ Angle \tag{4.32}$$

In order to assess the inclusion of the aberration angle, cuts were taken with and without the inclusion of the radome aberration in the AT. The results for a range of starting AUT angles can be seen in Figs. 4.30, 4.31, 4.32, 4.33 and 4.34.

From Fig. 4.30 the maximum deviation from $\Delta AZ/\Sigma = 0$ for the $[0, 0]^o$ cuts are shown to reduce from 0.026 to 0.012 with the introduction of the aberration. Similarly the RMS value is shown to reduce from 0.012 to 0.007 with the introduction of the *Aberration Angle*.

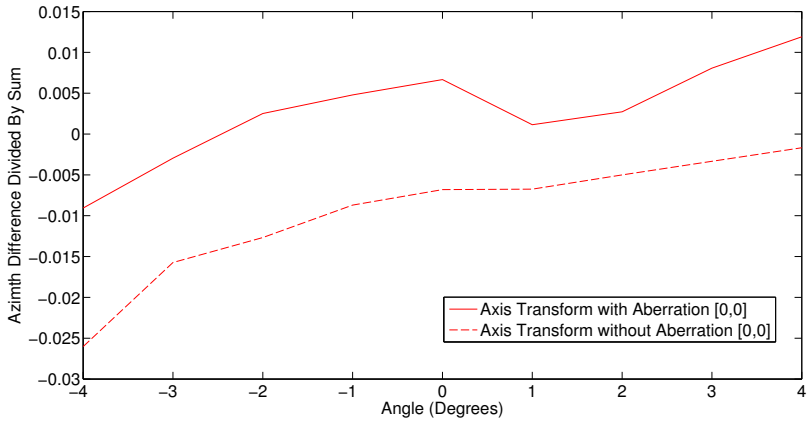

Figure 4.30: Measured $\Delta AZ/\Sigma$ with and without measured *Aberration Angles* in the AT at $[0, 0]^o$.

From Fig. 4.31 the maximum deviation from $\Delta AZ/\Sigma = 0$ for the $[0, 20]^o$ cuts are shown to reduce from 0.039 to 0.022 and the RMS value from 0.021 to 0.012 with the introduction of the *Aberration Angles*. These values explain the appearance of the graph, where the line without the *Aberration Angle* correction appears to be closer to 0, whereas in fact the line with the *Aberration Angle* correction it is on average closer to $\Delta AZ/\Sigma = 0$. The [0, -20]^o cuts maximum deviation are shown to reduce from 0.055 to 0.020, and the RMS value from 0.034 to 0.009 with the introduction of the *Aberration Angles*.

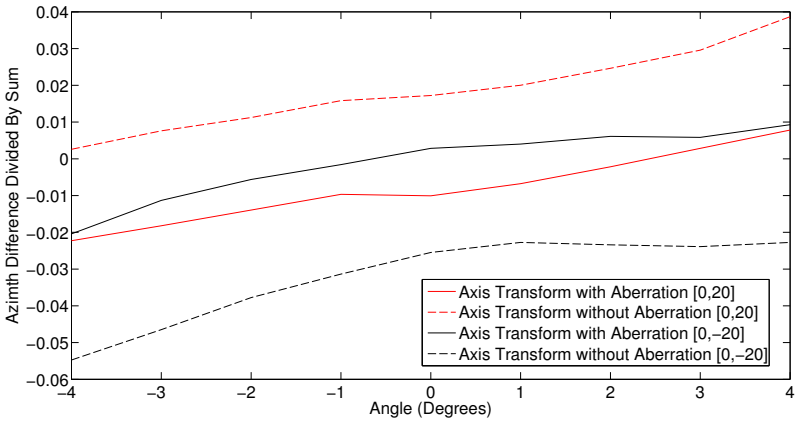

Figure 4.31: Measured $\Delta AZ/\Sigma$ with and without measured *Aberration Angles* in the AT at [0, 20]^o and [0, -20]^o.

From Fig. 4.32 the maximum deviation from $\Delta AZ/\Sigma = 0$ for the [20, 0]^o cuts are shown to reduce from 0.025 to 0.017 with the introduction of the *Aberration Angles*. Similarly the RMS value is shown to reduce from 0.016 to 0.011 with the introduction of the *Aberration Angles*. The [-20, 0]^o cuts maximum deviation is shown to reduce from 0.065 to 0.006, and the RMS value from 0.060 to 0.004 with the introduction of the *Aberration Angle*.

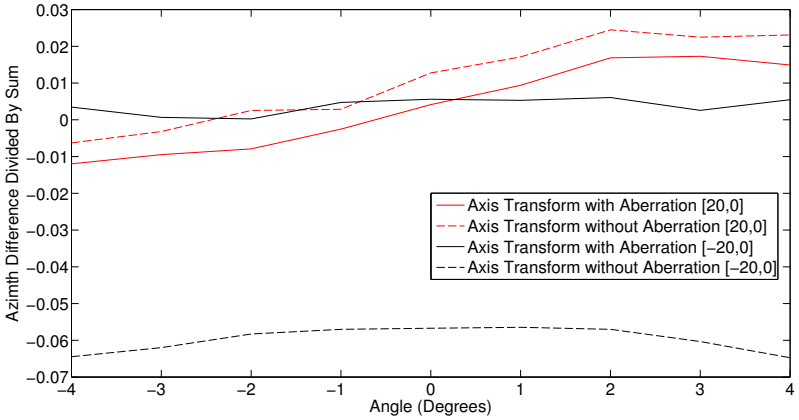

Figure 4.32: Measured $\Delta AZ/\Sigma$ with and without measured *Aberration Angles* in the AT at [20, 0]^o and [-20, 0]^o.

From Fig. 4.33 the maximum deviation from $\Delta AZ/\Sigma = 0$ for the [20, 20]^o cuts are shown to reduce from 0.050 to 0.016 with the introduction of the *Aberration Angles*, more clearly showing the effect of the AT. Similarly the RMS value is shown to reduce from 0.014

to 0.008 with the introduction of the *Aberration Angles*. The [-20, -20]^o cuts maximum deviation is shown to reduce from 0.100 to 0.023, and the RMS value from 0.080 to 0.013 with the introduction of the *Aberration Angles*.

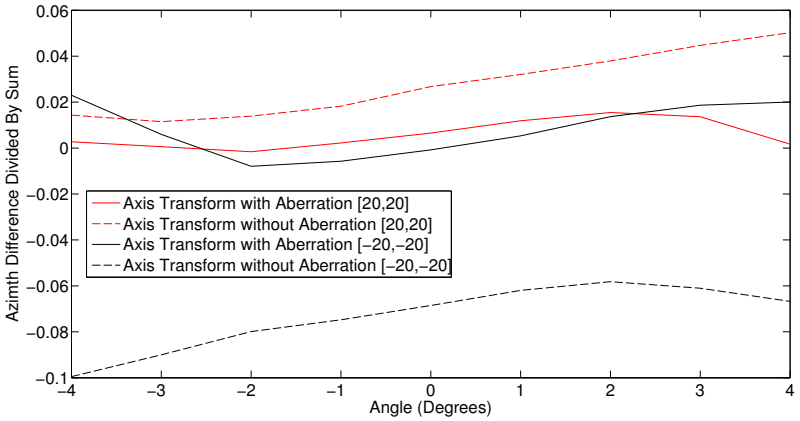

Figure 4.33: Measured $\Delta AZ/\Sigma$ with and without measured *Aberration Angles* in [20, 20]^o and [-20, -20]^o.

From Fig. 4.34 the maximum deviation from $\Delta AZ/\Sigma = 0$ for the [-20, 20]^o cuts are shown to reduce from 0.154 to 0.050, and the RMS value from 0.115 to 0.029 with the introduction of the *Aberration Angles*. The [20, -20]^o cuts deviation from $\Delta AZ/\Sigma = 0$ is shown to reduce from 0.139 to 0.056, and the RMS value from 0.094 to 0.030 with the introduction of the *Aberration Angles*.

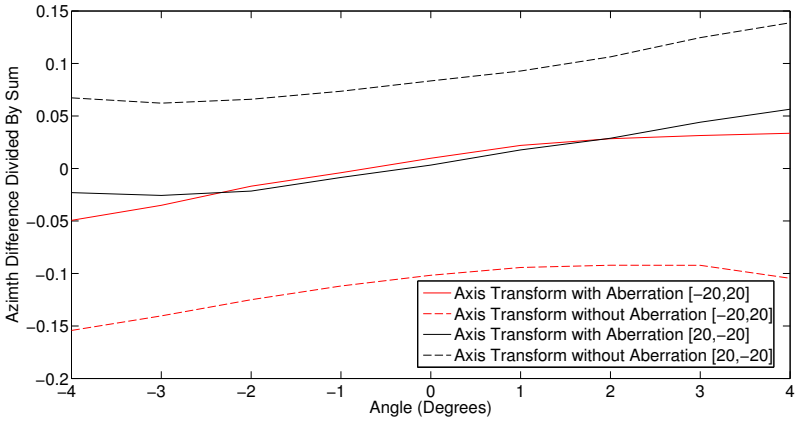

Figure 4.34: Measured $\Delta AZ/\Sigma$ for a TRMAS with and without measured *Aberration Angles* in the AT at [-20, 20]^o and [20, -20]^o.

The results are summarised in Table 4-G. The inclusion of the measured *Aberration Angles* improves the cut in the T frame by removing the offset from $\Delta AZ/\Sigma = 0$. It can be seen that the maximum deviation and RMS values in all cases are significantly improved by the inclusion of the aberration. It is only when compound angles are measured that the values start to significantly change from those measured at the [0, 0]^o position. It is noticeable that the values found at [-20, 20]^o and [20, -20]^o are the worst, however they are suitable for use.

POSITION (^{o})	**WITHOUT ABERR MAX**	**WITH ABERR MAX**	**WITHOUT ABERR RMS**	**WITH ABERR RMS**
[**0, 0**]	0.026	0.012	0.012	0.007
[**0, 20**]	0.039	0.022	0.021	0.012
[**0, -20**]	0.055	0.020	0.034	0.009
[**20, 0**]	0.025	0.017	0.016	0.011
[**-20, 0**]	0.065	0.006	0.060	0.004
[**20, 20**]	0.050	0.016	0.014	0.008
[**-20, -20**]	0.154	0.050	0.115	0.029
[**-20, 20**]	0.100	0.023	0.080	0.013
[**20, -20**]	0.139	0.056	0.094	0.030

Table 4-G: Maximum offset and RMS values for the $\Delta AZ/\Sigma$ with and without *Aberration Angles* at different start angles for an EL cut on the positioner.

4.5.2.2 AZIMUTH CUTS

The same pattern can be seen in the AZ cuts. The inclusion of the measured *Aberration Angles* significantly improves the cut in the T frame by removing the offset from $\Delta EL/\Sigma = 0$, Table 4-H. An example plot is shown in Fig. 4.35. Again, the variation from $\Delta EL/\Sigma = 0$ is small and are suitable for use. The small error could be due to the manual construction of the radome, or due to *Image Rotation* occurring.

POSITION (^{o})	WITHOUT ABERR MAX	WITH ABERR MAX	WITHOUT ABERR RMS	WITH ABERR RMS
[0, 0]	0.029	0.017	0.017	0.011
[0, 20]	0.022	0.011	0.018	0.006
[0, -20]	0.047	0.019	0.039	0.010
[20, 0]	0.040	0.014	0.022	0.011
[-20, 0]	0.110	0.024	0.084	0.013
[20, 20]	0.298	0.053	0.031	0.025
[-20, -20]	0.243	0.043	0.196	0.027
[-20, 20]	0.193	0.057	0.156	0.030
[20, -20]	0.203	0.046	0.149	0.003

Table 4-H: Maximum offset and RMS values for the $\Delta EL/\Sigma$ with and without *Aberration Angle* at different start angles for an AZ cut on the positioner. .

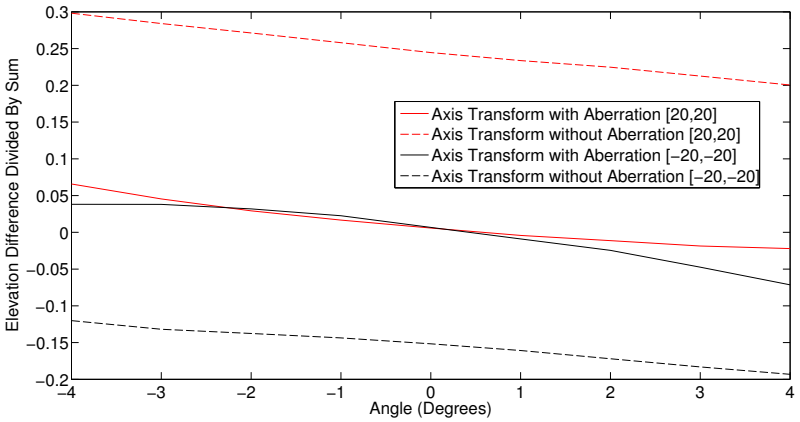

Figure 4.35: Measured $\Delta EL/\Sigma$ for a TRMAS with and without measured *Aberration Angles* in the AT at [20, 20]^o and [-20, -20]^o.

4.5.3 IMAGE ROTATION

Some of the error seen in the above cuts may be due to the *Image Rotation* caused by the mirror in the TRMAS. This will only affect images which are at a compound angle. Taking one way measurements the mirror imposes a rotation of the image into the system and

will lead to depolarisation. Tables 4-G and 4-H show that the largest residual error after the AT has been applied occurs at compound angles. The value of the *Image Rotation* can be calculated from Equation (4.33) at the largest angular position of the sweep and the values are presented in Table 4-I.

$$Image\ Rotation\ =\ \tan^{-1}\ \frac{\Delta AZ}{\Delta EL} \tag{4.33}$$

POSITION (^{o})	**IMAGE ROTATION** (^{o})
[**20, 20**]	0.2
[**-20, -20**]	1.7
[**-20, 20**]	2.1
[**20, -20**]	3.1

Table 4-I: *Image Rotation* values at different start angles.

Table 4-I shows the same trend in increasing values as a function of start value as the previous work on the $\Delta AZ/\Sigma$, indeed the cuts starting at [-20, 20]^o and [20, -20]^o are most effected by the *Image Rotation*. The largest value of *Image rotation* is 3.1^o, which equates to a loss of 0.013 dB due to depolarisation from Equation (4.34). Therefore this is not a significant effect on the performance of the TRMAS and is not required to be included in the measurements.

$$Polarisation\ Loss\ Factor = \cos^2(Image\ Rotation) \tag{4.34}$$

4.6 AC POSITIONER TEST OF A SWEPT MOTION

The positioner is not natively set up such that it can perform a sweep in AZ whilst keeping the **E** vector vertical, thus swept measurements cannot be taken. A sweep in AZ would also require a movement in ROLL on the positioner, EL remains constant. However, if the motion of the two axes in question are synchronised in the control code this swept measurement can be achieved to a good level of approximation.

The movement of an axis of the positioner is completed in 3 phases: an acceleration, a constant velocity and a deceleration. If the smoothing factor is set to 0 these phases prescribe a trapezium. If the movement of each axis takes the same time, i.e. the rates of the 3 phases are scaled, there will be a linear relationship between the two axes. This means that the movement of the axes can be controlled such that there is a known movement relationship between them and the **E** vector will stay constant through a movement.

As the AZ axis has the furthest angular distance to travel we will scale the ROLL axis to the movement of the AZ axis. The acceleration and deceleration values is set to 12740 counts s^{-2}, the velocity is set to 21840 counts s^{-1} for AZ.

The following example is for a movement from [X, Y]^o to [-X, Y]^o as a general case. To calculate the velocity of the ROLL axis, the angular *Distance Travelled* by the AZ and ROLL axes is calculated from the AT. These movements want to be synchronised, so the *Time Taken* for each movement is required to be the same. Therefore using Equation (4.35) the *velocity* of the ROLL axis can be calculated, Equation (4.36).

$$Velocity = \frac{Distance\ Travelled}{Time\ Taken} \tag{4.35}$$

$$ROLL\ Velocity = \frac{ROLL\ Distance\ Travelled}{AZ\ Distance\ Travelled}\ AZ\ Velocity \tag{4.36}$$

Similarly to calculate the *acceleration* of the ROLL axis, the *Time Taken* for each movement is required to be the same. Therefore using Equation (4.37) the *acceleration* of the ROLL axis can be calculated, Equation (4.38).

$$Acceleration = \frac{Velocity}{Time\ Taken} \tag{4.37}$$

$$ROLL\ Acceleration = \frac{ROLL\ Velocity}{AZ\ Velocity}\ AZ\ Acceleration \tag{4.38}$$

These calculations are implemented in the MATLAB control code for the AC and swept measurements performed.

4.6.1 VISUAL ASSESSMENT OF SWEEP

The positioner was moved from [40, 40]^o to [-40, 40]^o and the orientation of the ROLL axis monitored. It was shown that the E vector on the ROLL axis remained vertical and constant throughout the sweep, Fig. 4.36. This was repeated for other start and finish positions with the same result.

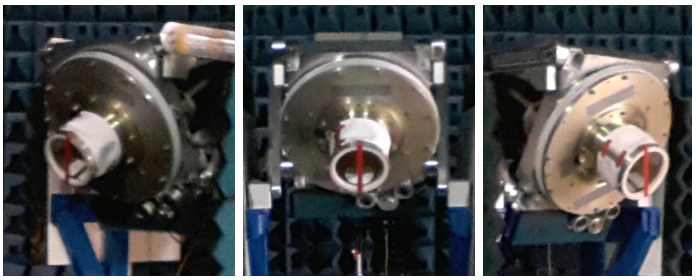

Figure 4.36: Start, middle and end positions of a swept motion in the AC. Left image: positioner at [40, 40]^o. Middle image: positioner at [0, 40]^o. Right image: positioner at [-40, 40]^o.

4.6.2 QUANTITATIVE ASSESSMENT OF SWEEP

The error this method of constant time introduces to the ROLL position was calculated. The actual ROLL angle as a function of AZ angle was calculated using the AT for 100 points over a sweep between [40, 40]^o and [-40, 40]^o. Fig. 4.37 shows this angle as a function of AZ angle, and the constant time straight line defined by the start and end positions.

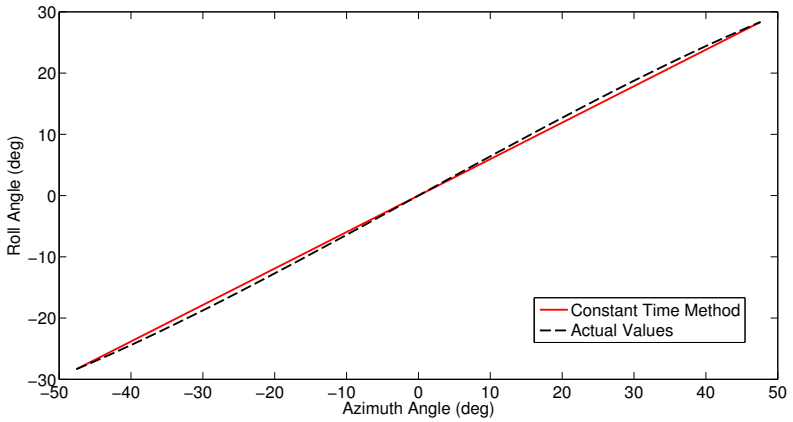

Figure 4.37: ROLL angle as a function of AZ angle for the constant time approximation and the actual calculated values.

Fig. 4.38 shows that the difference between the approximation and the real value for ROLL angle is at maximum 0.895^o, which equates to a loss in gain of 0.001 dB using Equation (4.34). The RMS difference between the approximation and the real values is 0.639^o. Therefore this constant time approximation is suitable for use.

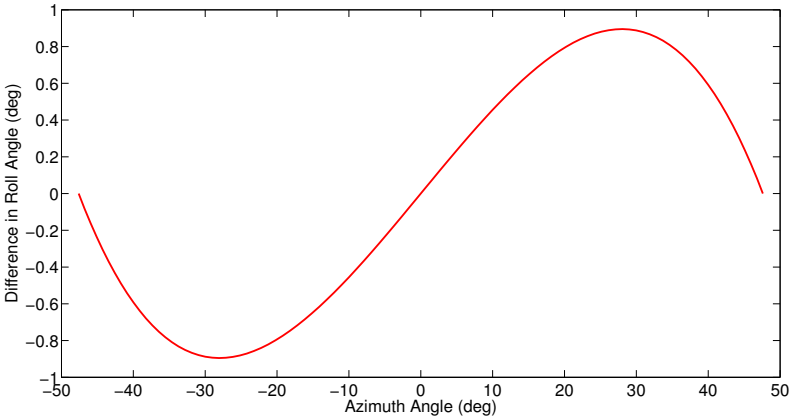

Figure 4.38: Difference in ROLL angle as a function of AZ angle between the constant time approximation and the actual calculated values.

4.7 CHAPTER SUMMARY

The derivation of an AT for a 3 axis positioner has been presented. It has been verified by simulation to show that the cuts produced are in the T frame and are correct for a TRMAS, i.e. the $\Delta AZ/\Sigma$ has been shown to reduce to 0. The AT and code implementation was then tested using a LEGO NXT positioner and the positioner in the AC and was shown to correct the movement of the positioner so the attitude of the TRMAS was correct. The AT and code implementation was tested on the AC positioner. This was shown to correctly place the **E** vector of the AUT. The AT was then tested in an AC with a TRMAS and radome system. It has been shown that the performed cut has reduced the $\Delta AZ/\Sigma$ to 0 ± 0.05, as expected. It has also been shown that the presented method of including radome aberration into a single AT is valid. This method will simplify the measurement of antenna radome systems in an AC and preserve the polarisation when measuring a polarisation sensitive antenna with a shaped radome. Also presented is a method of running the positioner in a sweep manner with the **E** vector remaining upright allowing AUT data to be measured in a swept motion.

This work has shown that the measurement of a TRMAS is successful in an AC using the presented AT. When completing a cut it would be possible to use the aberration value at each position of the cut, rather than using the aberration value of the start position. This may reduce some of the deviations from $\Delta AZ/\Sigma = 0$ that have been seen, but in general the aberration does not change significantly over a few degrees so significant improvement may not be seen.

The next chapter starts to investigate the design improvement of a TRMAS, and details the design and test verification of a PSG in a TRMAS.

Chapter 5

DESIGN AND TEST VERIFICATION OF A POLARISATION SELECTIVE GRID

5.1 INTRODUCTION

This chapter presents simulation and hardware measurement results that have been used to optimise the structure of the GLs of a PSG to optimise cross-polar isolation performance at the centre of Ku band.

The findings of this research show that the copper *GLD* can be reduced to 15 μm and still provide better than -25 dB cross-polar isolation with a Grid Line Width (*GLW*) of 1.03 mm and a Grid Line Pitch (*GLP*) of 1.92 mm for a Reflector Depth (*RD*) of 0.5 mm. The field simulation and measurements presented show that a thinner grid than this results in deterioration of the cross-polar isolation performance of the PSG, and a thicker grid does not improve the performance. Minimisation of the GLD is important to allow the manufacturing process to be streamlined, reduce costs and to ensure a well performing PSG. Reducing the metal *GLD* is desired because the edge definition that can be achieved after etching is superior and process time is reduced. It also allows the *RD* of the dielectric substrate to be reduced to allow flexing or deforming for conformal applications. The resultant reflector will have maximised cross-polar isolation performance and manufacturability whilst minimising cost.

5.1.1 IMPROVING A POLARISATION SELECTIVE GRID

A PSG is made up of two main components whose properties need to be investigated:

- **SUBSTRATE**: The material on which the PSG GL are deposited has an effect mainly on the co-polar transmission properties of the PSG. Therefore the material and *RD* of the substrate are factors that need to be investigated to reduce the co-polar transmission properties of the PSG.
- **STRUCTURE OF THE PSG**: The exact structure of the metal GLs that form the PSG affect the co-polar transmission and cross-polar isolation of the PSG. Therefore the material, *RD*, *GLW* and *GLP* need to be investigated to improve the performance of the PSG in both co-polar transmission and cross-polar isolation.

The investigation into the improvement of a PSG will have two distinct phases; firstly simulations will be run in HFSS and secondly, from the simulation results, hardware test and validation will be carried out to assess the improved performance of the PSG.

5.2 PSG SIMULATION METHODOLOGY

This investigation requires knowledge of how the fields behave in a thin metal structure. To enable this the 3-Dimensional electromagnetic simulation package has to mesh inside the metal object and use skin depth information. Therefore this simulation has to be completed in a full field simulator, such as Ansoft HFSS [55] or CST, which is able to model the field in a metallic medium with a finite conductivity.

HFSS is to be used for the simulations. There are several approaches that could be used for such an optimisation. A whole PSG could be simulated which represents the geometry of the system in question, however, this would take a large amount of model construction and simulation time and computational power. As the structure to be simulated is periodic in structure and the smooth curve of the parabola can be modelled as flat a unit cell model with Floquet ports can be used. This unit cell structure can be simulated to infinity, whilst the model remains electrically small. This means that a physically large structure can be simulated accurately on a small computational scale.

5.2.1 UNIT CELL MODEL STRUCTURE

A model was constructed containing a PSG structure made up of a dielectric substrate with copper GLs on its surface surrounded by an air box, Fig. 5.1. To ensure that the fields go through the substrate with minimum insertion loss the thickness of the dielectric substrate is well below λ / 2 [76]. Initially, a nominal grid is formed with GLW = 1 mm and GLP = 2 mm. The GLW is smaller than 0.3 λ therefore the reflection coefficient of the grid should be better than -25 dB [77]. The model is set to mesh inside the metal to fully simulate the internal fields and apply skin depth criteria thus not treating the metal as an idealised medium. The air box is set to be a quarter wavelength in the z direction away from both surfaces of the reflector. This ensures that the metal boundary is far enough away to not interfere with the simulation and to emulate free space. The GLs are aligned to be parallel to the x axis and a unit cell defined to be a square the size of two GLW and Grid Line Gaps (GLG).

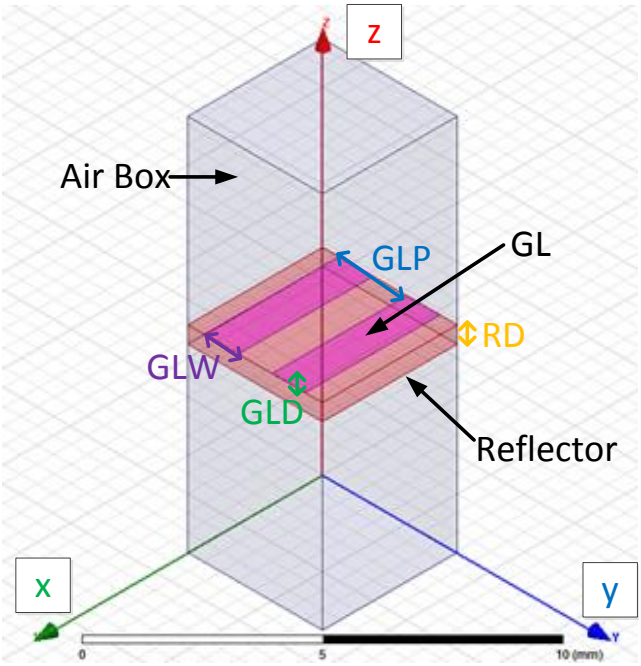

Figure 5.1: Geometry of the PSG unit cell simulation.

As this is a repeating structure in both the x and y directions using Floquet ports the initial set up of the model is of great importance [78] [79]. To create a repeating structure

both boundaries in the x axis have to have the same construction, the same applies for the y axis. This means that in the y axis both boundaries have to be either just reflector or reflector with GL, it cannot be a mixture of the two. In the x axis this is simpler as it is a cross section perpendicular to the GLs and will therefore inherently be the same, Fig. 5.2.

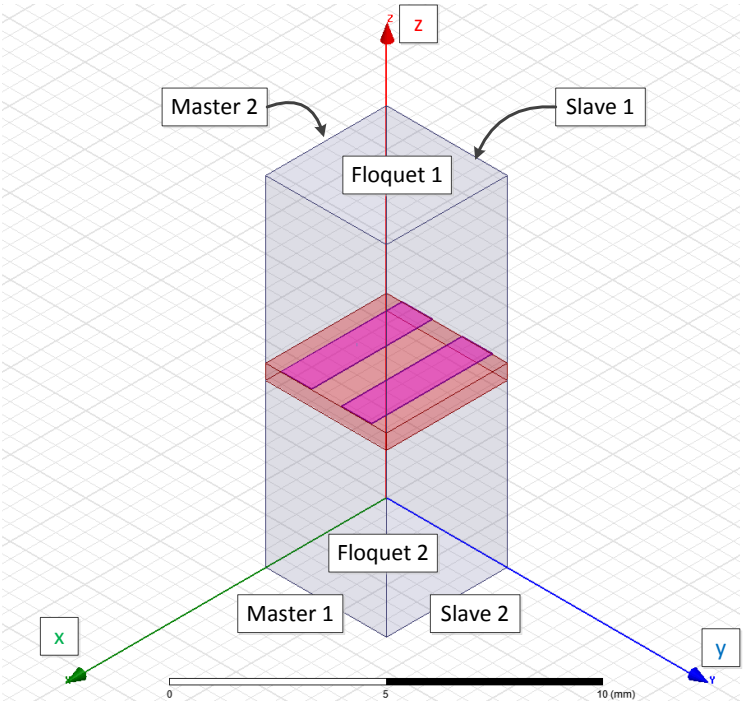

Figure 5.2: Master and slave boundaries in the yz and xz planes and the Floquet ports which define the repeating structure of the PSG unit cell simulation.

To ensure that the boundaries in the y plane are identical the model is set up so that it contains two GLs and two GLGs. One GLG to be found between the two GLs, the other is split so there is half on either side of the GL. Therefore the boundary is always just the reflector. The model could have been set up with a single GL, but it is easier to visualize the change in *GLP* and *GLW* if two grids are shown in the unit cell. This allows for error checking in the model more clearly and does not increase the electrical size of the model to a long running one.

As this is a parameterised model, allowing physical properties to be simulated through a range of values, the physical lengths have to be carefully set up and to allow a change in

size of unit cell to cope with the increase or decrease of the GLs, GLGs and RD in the x, y and z axes. The following dimensions on the model were set to parameterised values:

- *GLW* (m): Defines the width of the GL in the y axis.
- *GLP* (m): Defines the pitch of the GLs and therefore the spacing in the y axis.
- *GLD* (m): Defines the depth of the GL in the z axis.
- *RD* (m): Defines the depth of the reflector in the z axis.
- Air Box (m): Defines the distance from the surface of the reflector to the end of the air box.

From these values the unit cell can be constructed so it will always be a valid in terms of a repeating structure using Floquet ports. The *Unit Cell Width* of the model can be calculated using Equation (5.1) with the *y Value of First Grid Line* starting at the position defined by Equation (5.2). The *Height of the Unit Cell* model is defined by Equation (5.3).

$$Unit\ Cell\ Width\ =\ 2\ GLP \tag{5.1}$$

$$y\ Value\ of\ First\ Grid\ Line\ =\ \frac{GLP\ -\ GLW}{2} \tag{5.2}$$

$$Height\ of\ Unit\ Cell\ =\ \frac{\lambda}{2}\ +\ GLD\ +\ RD \tag{5.3}$$

With this set up it is possible to set up the master and slave and the Floquet boundaries required to make the simulation appear infinite. Two sets of master and slave boundaries are set up, in the yz plane and in the xz plane, and the excitations are set as two Floquet ports as shown in Fig. 5.2. This shows that the energy in the simulation flows from top to bottom and the S parameters can be extracted and analysed to show the performance of the grid set up. As the model is fully parameterised sweeps of key dimensions can be made to optimise the performance of the reflector.

This unit cell simulation described will be altered to investigate each facet of the PSG.

5.2.2 REFLECTOR SUBSTRATE MATERIAL AND THICKNESS

As the *GLD* is of order 10's of microns, this means that to manufacture this grid the metal has to be supported by a substrate. The substrate must be able to be shaped and be mechanically and thermally stable over the range of the required performance of the antenna. This substrate, the reflector body, will have a detrimental effect on the performance of the reflector as it provides extra blockage and interference to the path of the RF going through the TRMAS system. This means the material and the *RD* of the reflector are properties that need to be optimised for minimum impact.

5.2.2.1 REFLECTOR SUBSTRATE MATERIAL AND MANUFACTURE

The material of the reflector has to be able to be accurately and repeatedly shaped in manufacture. The tolerances that are required on the surface of the parabolic shape can be derived from the allowable de-focussing of the feed horn.

Equation (5.4) defines a parabola where x and y are the respective axis co-ordinates and f is the focal length, 0.1 m, as shown in Fig. 5.3.

$$y = \frac{x^2}{4\,f} \tag{5.4}$$

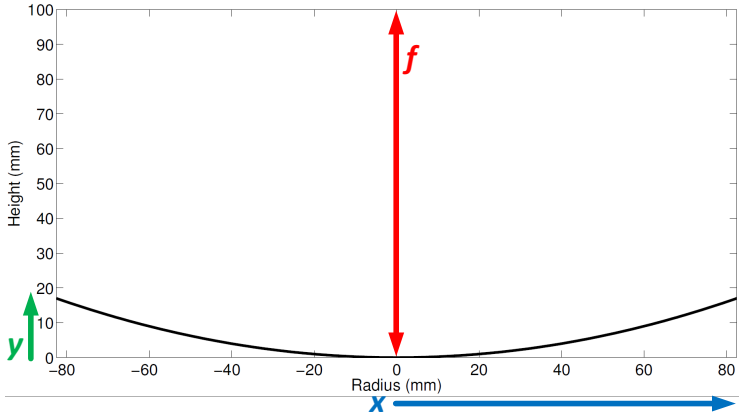

Figure 5.3: Dimensions of a parabola.

To assess the shape of the reflector the parabolic shape can be easily measured on a coordinate-measuring machine. The variation in height as a function of radius is the simplest metric to characterise the parabola. To calculate the allowable deviation from the parabolic surface δy, the allowable deviation in height of the parabola, should be calculated. The parabola in question has $f = 100$ mm, maximum $x = 0.0825$ m (the radius of the reflector) and an allowable $\delta f = 1$ mm as determined from experimental measurements. Using Equations (5.5) and (5.6) the allowable deviation in the surface profile can be calculated from Equation (5.7) to be $\delta y = \pm\ 0.17$ mm. Equivalent to a phase change ($\Delta\phi\ (^o)$) of 3.2^o from Equation (5.8).

$$y_{max} = \frac{x^2}{4\ (f - \delta f)} \tag{5.5}$$

$$y_{min} = \frac{x^2}{4\ (f + \delta f)} \tag{5.6}$$

$$2\ \delta\ y = y_{max} - y_{min} \tag{5.7}$$

$$\Delta\phi = \frac{2\ \pi}{\lambda}\ \delta\ y \tag{5.8}$$

Therefore injection moulding is the sensible choice for the process. Vacuum moulding is not able to achieve the shape tolerances for the parabolic reflector, and may not be able to cope with the thermal cycling involved with the deposition of the grid lines.

The reflector is manufactured from an injection moulded plastic which has a low $\epsilon_r = 2.5$ and loss tangent $\tan\delta = 0.007$, PC/ABS Bayblend T45. This will give minimum interference to the RF, whilst allowing a suitable manufacturing process to be used. In this instance assessing only the change in focal length is acceptable to assess suitability. The reflectors are made from an injection moulded process which gives a very repeatable reflector parabolic profile. In general the RMS surface error of the parabola should be investigated and Ruse's equation used to assess the functionality of the parabola, Equation (5.9. Where ϵ is the surface RMS error of the parabola and G_o is he gain of the antenna in the absence of surface errors.

$$G_{(\epsilon)}\ (dB) = G_o\ e^{-\ (\frac{4\ \pi\ \epsilon}{\lambda})^2} \tag{5.9}$$

5.2.2.2 OPTIMISATION OF REFLECTOR DEPTH

Having chosen the material to manufacture the reflector from it is now possible to assess the impact of the *RD* on the performance of its transmission in the unit cell model. It is obvious that the thicker the material is the more effect it will have on the transmission performance, so a balance between degradation of the transmission and ability to support the grid structure over the environmental conditions needs to be reached. Care also has to be taken to avoid the thickness being a multiple of the wavelength of the frequency in question to avoid unwanted resonances. To ensure that the fields go through the substrate with minimum insertion loss the thickness of the dielectric substrate should be kept well below λ / 2 [76]. The simulation is run without the grid lines, Fig. 5.4

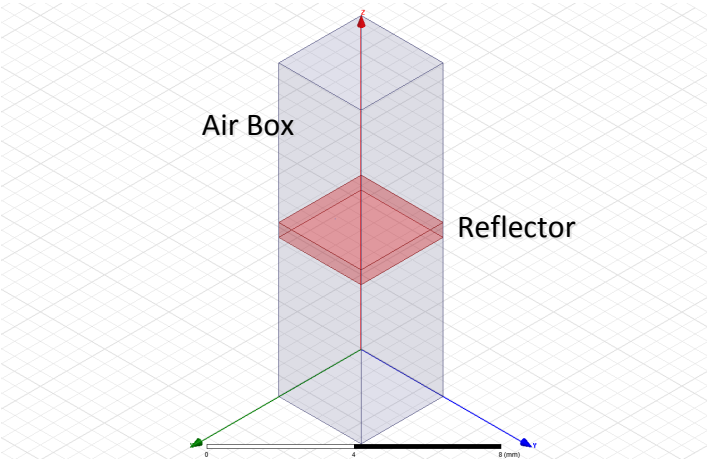

Figure 5.4: Unit cell PSG simulation containing only the reflector material.

The thickness of the reflector is run as a parameterised sweep from 0 to 5 mm in the unit cell model. Fig. 5.5 shows how the transmission varies as a function of *RD* at 15 GHz. The transmission can be seen to increase to a maximum and then start to decrease, showing the repeating nature of the thickness performance as a function of reflector thickness. The fringings seen are facets of the unit cell simulation and are not real. At positions where the fringing is seen the simulation has 9 instead of 5 passes to converge showing that the model had difficulty to converge at these points.

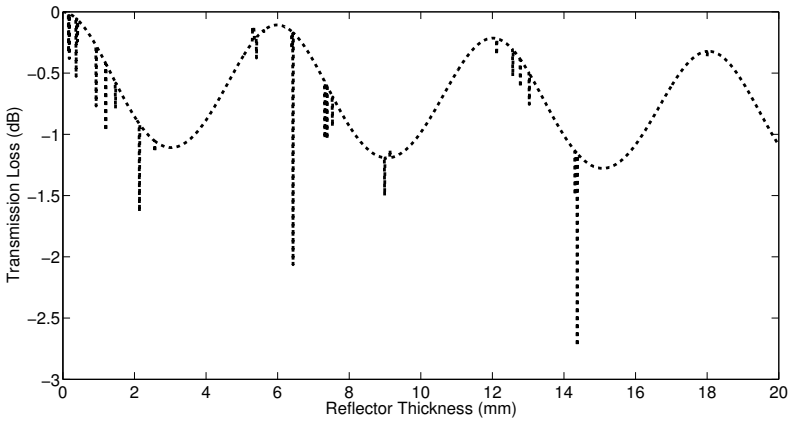

Figure 5.5: Transmission loss as a function of RD at 15 GHz.

The downward trend of the maxima are due to the loss tangent of the increased thickness of the material, as shown by Equation (5.10 and Table 5-A.

$$Expected\ Loss\ (dB)\ =\ 20\ log_{10}\ (e^{-\ tan\delta\ Reflector\ Thickness\ \frac{2\ \pi}{\lambda}}) \tag{5.10}$$

REFLECTOR THICKNESS (m)	**CALCULATED LOSS (dB)**	**MEASURED LOSS (dB)**
0	0	0
0.006	-0.11	-0.12
0.01201	-0.21	-0.24
0.01803	-0.32	-0.36

Table 5-A: Comparison of loss results for as a function of reflector thickness for equation calculated loss and simulation measured loss.

These results indicate that the RD should be at maximum 1.1 mm to keep transmission below -0.5 dB. The thinnest structurally stable reflector that can be manufactured is 0.5mm. Therefore $RD = 0.5$ mm will be investigated.

The simulation is then run across the Ku band frequency. Fig. 5.6 shows how the transmission varies as a function of frequency for a 0.5 mm thick reflector, it can be seen to

function well over the range of frequencies, with a trend of increasing co-polar transmission loss with increasing frequency.

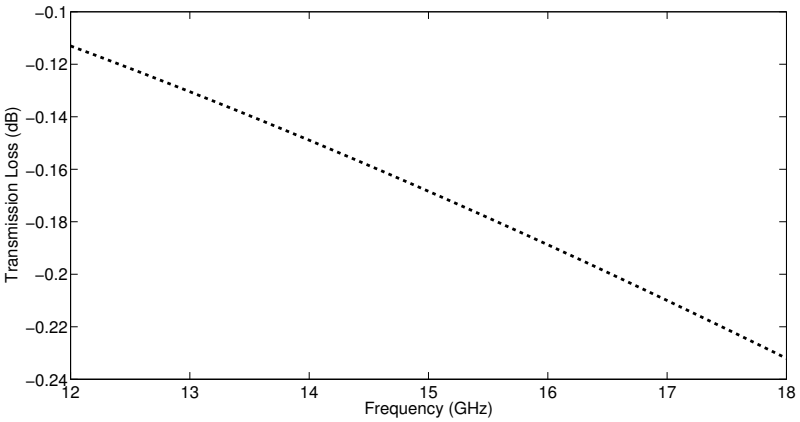

Figure 5.6: Transmission loss as a function of frequency for a 0.5 mm thick reflector.

5.2.3 GRID MATERIAL DEFINITION

5.2.3.1 INCLUSION OF METAL GRID

A nominal grid is added to the reflector structure with $GLW = 1$ mm, $GLP = 2$ mm and $GLD = 5$ μm. This grid has not been optimised, so it is not expected to work at the correct level at the frequency under test of 15 GHz. This nominal grid is to be used to investigate the required metal to form a working PSG and as a basis to carry out the further optimisations.

The co-polar transmission and cross-polar isolation is frequency dependent as shown in Fig. 5.7. This shows degradation in performance for both co-polar transmission and cross-polar isolation with increase in frequency. This shows that it is important to optimise the performance of the reflector at the top of the desired band of frequency operation. The metal that the GLs are manufactured from will next be investigated.

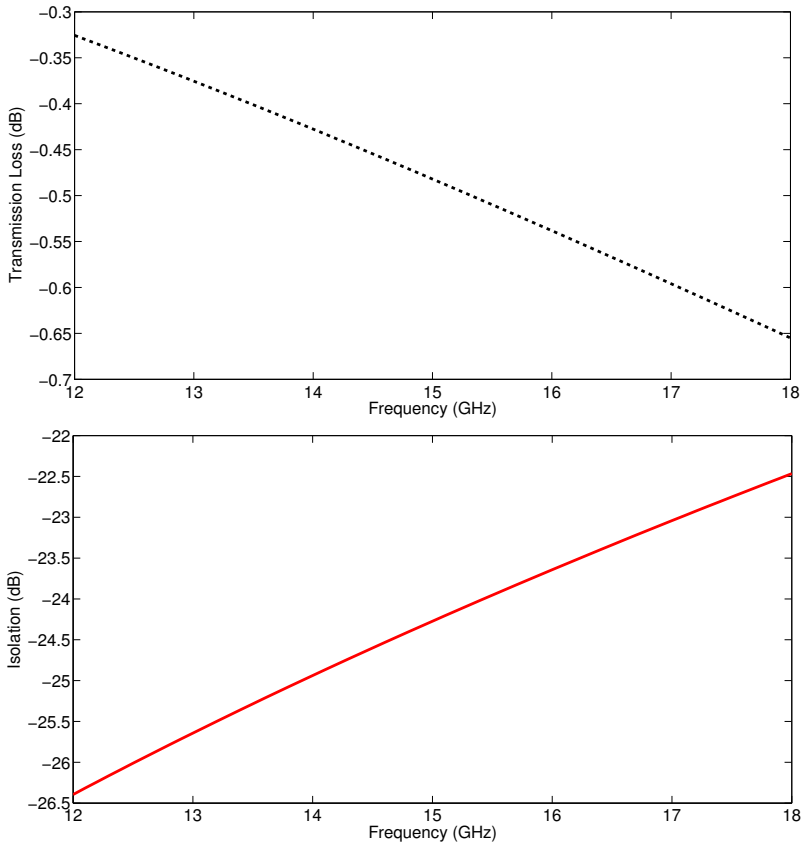

Figure 5.7: Co-polar transmission loss and cross-polar isolation as a function of f for a 0.5 mm thick reflector.

5.2.3.2 METAL GRID MATERIAL DEFINITION

To define the metal that the GLs are to be manufactured from the conductivity (σ (Sm^{-1})) of the GL is to be investigated. A parametric sweep in HFSS is set up to vary the σ of the metal of the GLs. The other parameters are kept the same and the performance of the grid is shown as a function of the σ.

Fig. 5.8 shows that as long as the $\sigma >$ 0.3 x 10^4 Sm^{-1} then the grid will perform well in co-polar transmission and cross-polar isolation. This means that several materials would be suitable, copper is to be used rather than the more expensive gold. It also gives the opportunity to use a combination of metals in the production of the GLs if this aids manufacture.

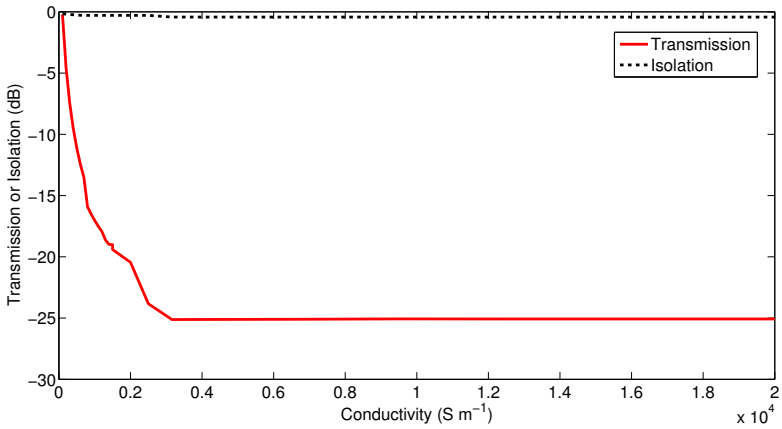

Figure 5.8: Co-polar transmission and cross-polar isolation as a function of σ for a PSG.

5.2.4 GRID LINE WIDTH AND PITCH OPTIMISATION

The best case for co-polar transmission will be to have 0 mm wide grid lines, and the best case for cross-polar isolation will be to have the reflector surface fully covered in metal. It is apparent that the optimisation of the *GLW* is tied to its *GLP*. Therefore a dual optimisation was set up in HFSS where both the *GLW* and *GLP* are varied to see the effect on the S21 co-polar transmission and cross-polar isolation. Fig. 5.9 shows the results of the optimisation where the co-polar transmission target value is -0.5 dB, the cross-polar isolation target value is -26 dB, the convergence criteria is 1 x 10^{-6} and the variables are *GLW* and *GLP*. It can be seen that the optimised $GLW = 1.03$ mm and $GLP = 1.92$ mm, which when used in a simulation gives a co-polar transmission value of -0.52 dB and a cross-polar isolation value of -26.24 dB. During the optimisation the GLP is set first and then the GLW continues to be optimised until the simulation conditions are met.

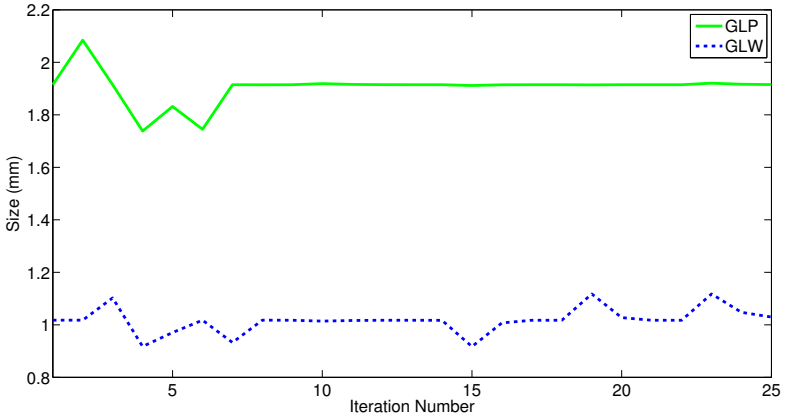

Figure 5.9: HFSS optimisation results for GW and GP size.

5.2.5 GRID LINE DEPTH MINIMISATION

The minimisation of the *GLD* is important to allow the manufacturing process to be streamlined. Reducing the metal *GLD* is desired because the edge definition that can be achieved after etching is superior with a thinner GL and process time is reduced. It also allows the thickness of the dielectric substrate to be reduced to allow flexing or deforming for conformal applications. The resultant reflector will have maximised cross-polar isolation performance and manufacturability whilst minimising cost, it is suitable for many types of antenna systems.

5.2.5.1 SKIN DEPTH

It has been a widely held heuristic that if the depth of a metal is over 5 times the skin depth (δ (m)) at the frequency under test then the current density will decay through the depth of the metal [80]. Therefore fluctuations due to reflection effects in the metallic medium become minimal and no longer dominate the cross-polar isolation value [81].

From Equation (5.11) the δ of copper can be calculated at 0.53 μm where: f = 15 GHz; conductivity of copper = 5.96 x 10^{-7} Sm^{-1}; μ_o is the permeability of free space (4 π x 10^{-7} Hm^{-1}) and μ_r the relative permeability of copper (0.999994).

$$\delta = \sqrt{\frac{1}{\pi f \sigma \mu_o \mu_r}} \tag{5.11}$$

5.2.5.2 INTERPRETATION OF SIMULATED S21 RESULTS

A simulation was carried out for a range of $GLD = 0$ to 30 μm, with all other variables remaining static. **E** vectors parallel and perpendicular to the GLs were simulated. The co-polar transmission loss and the cross-polar isolation results are plotted in Fig. 5.10. The dip seen in the transmission line is a simulation artifact as previously seen.

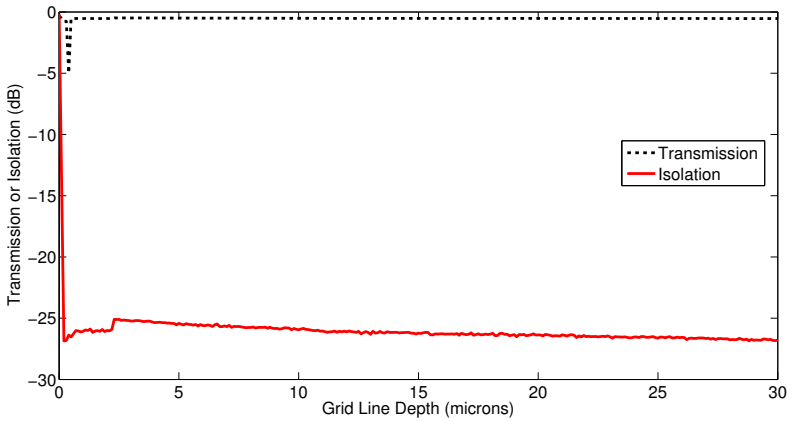

Figure 5.10: Co-polar transmission and cross-polar isolation as a function of copper *GLD*.

Fig. 5.10 shows that if the *GLD* is greater than 0.2 μm then the PSG performs as required with a cross-polar isolation of better than -25 dB in the simulation. Between *GLDs* of 0.20 and 2.3 μm the cross-polar isolation then fluctuates due to the reflection effects inside the metal [81]. When the *GLD* is over 2.3 μm (i.e. 5 times the skin depth, the co-polar transmission is stabilised at better than -25 dB.

To show how the **E** vector incident on the GLs behaves, the thickness of the GLs was set to 2.5 μm and the simulated **E** magnitude was plotted for **E** vectors parallel to and perpendicular to the GLs, Fig. 5.11. When the **E** vector is perpendicular to the GLs the plane wave passes through the grid lies largely undisturbed, when the **E** vector is parallel to the GLs the **E** cannot pass through the GLs and the plane wave is strongly reflected.

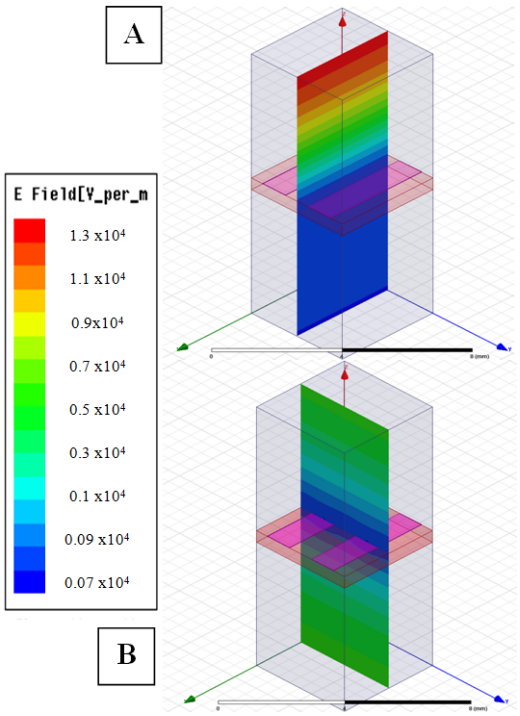

Figure 5.11: **E** field variation in normal incidence travelling from top to bottom of the geometry at f = 15 GHz. A) **E** field parallel to the GLs and the field being reflected. B) **E** field perpendicular to the GLs and the field passing through. The *GLD* is 2.5 μm.

5.2.6 DEFINITION OF OPTIMAL GRID FROM SIMULATION

From the simulation work presented here a PSG with $GLD = 2.3$ μm, $GLW = 1.03$ mm, $GLP = 1.92$ mm on a reflector with $RD = 0.5$ mm is predicted to perform at the cross-polar isolation level of -25 dB.

5.3 POLARISATION SELECTIVE GRID TESTING

The performance of the PSG can be tested in cross-polar isolation and co-polar transmission to validate the simulation results.

5.3.1 MANUFACTURE OF POLARISATION SELECTIVE GRID

Using the findings from the results presented in the simulation section, a grid of $GLD = 5 \pm 2\ \mu$m, $GLW = 1.03 \pm 0.05$ mm and $GLP = 1.92 \pm 0.05$ mm was manufactured on a plastic substrate made from injection moulding PC/ABS Bayblend T45, with $\epsilon_r = 2.5$, $\tan\delta = 0.007$ and $RD = 0.7$ mm as shown in Fig. 5.12. As this is a prototype, the thinnest easily manufactural and measureable grid and reflector was used.

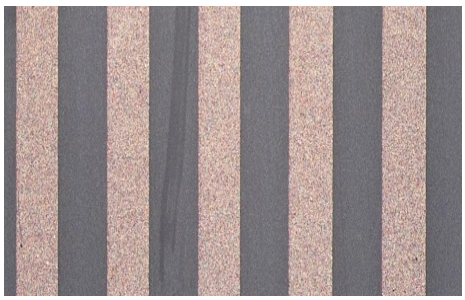

Figure 5.12: Manufactured PSG. The GLs are orange, reflector substrate grey.

5.3.2 PSG CROSS-POLAR AND CO-POLAR HARDWARE TEST

To test the cross-polar isolation and co-polar transmission of a PSG a bench test set up was constructed. A jig to hold the PSG in a stable position and allow an accurate and repeatable orientation with respect to the test horns was designed and manufactured from rapid prototyping. The test horns have specific slots in the test fixture to ensure repeatable positioning. The test horns used are Ku band pyramidal horns. These are connected to an VNA via coaxial cables. All cables and connectors are rated to 18 GHz. This experimental set up is shown in Fig. 5.13.

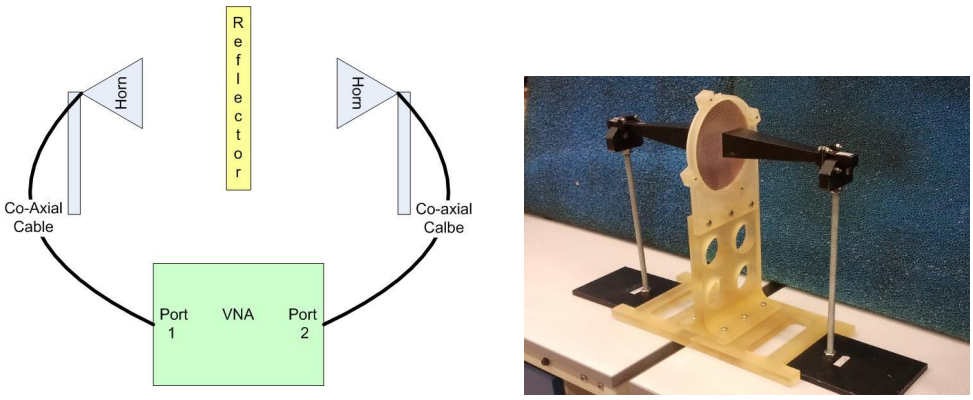

Figure 5.13: Hardware test set up for PSG testing. Left hand image: schematic set up. Right hand image: stand with PSG and the test horns used.

5.3.3 S PARAMETER MEASUREMENT VALIDATION

Measurements with no reflector are taken to allow the effect of the additional cables, connectors, pyramidal horns and free space losses to be corrected for. With the reflector fixed in the jig at a certain rotation the S parameters are measured. The reflector is then rotated to the next orientation and the S parameters measured again.

The S_{12} and S_{21} should be reciprocal, however this will be checked. Fig. 5.14 shows the corrected S_{12} and S_{21} co-polar transmission results for a reflector in the nominal position of 0^o overlay well. The RMS error difference between the 2 measurements was calculated to be 0.0012 dB and the maximum difference 0.238dB. Therefore only S_{21} measurements of the PSGs will be presented.

The PSG should be rotationally symmetric. Fig. 5.15 and Table 5-B shows the difference between the possible orientations for a PSG. 0^o is defined as the first position, 90^o is a 90^o rotation from the first position clockwise, similarly for 180^o, 270^o and 360^o. Therefore 360^o is a repeat of the measurement at the 0^o position. It can be seen that, as expected, the different orientations of the PSG overlay very well. 90^o and 270^o have less variation as these are co-polar transmission. This shows that the test set up is robust and reliable and that the PSG is well manufactured and rotationally symmetric.

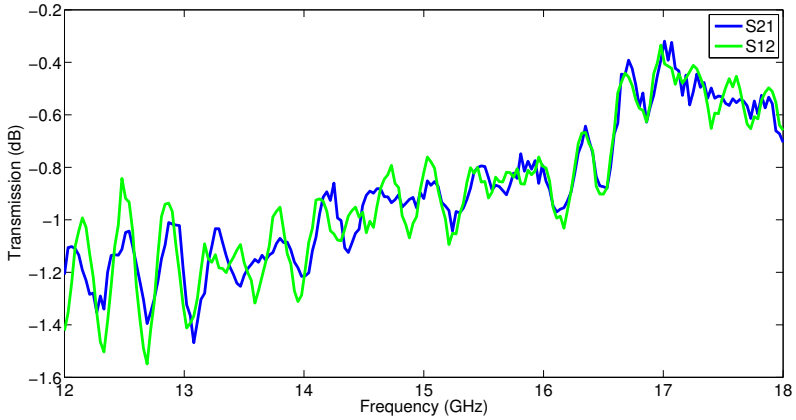

Figure 5.14: S_{21} and S_{12} results for PSG hardware testing in co-polar at 0^o.

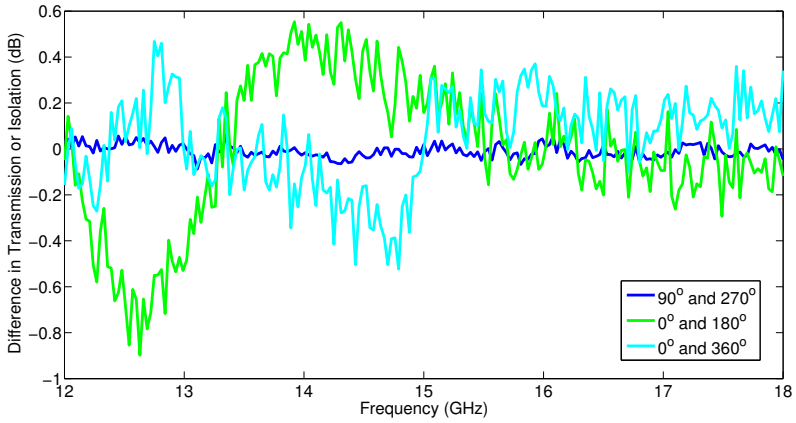

Figure 5.15: Difference in S_{21} results for PSG hardware testing at different orientations.

ANGLES (^{o})	**MAX DIFFERNCE (dB)**	**RMS (dB)**
90 and 270	0.088	0.026
0 and 180	0.898	0.247
0 and 360	0.523	0.174

Table 5-B: Maximum offset from 0 and RMS values for S_{21} results at different orientations.

5.3.3.1 REFLECTOR MEASUREMENT RESULTS

Fig. 5.16 shows the results for a PSG with $GLD = 5$ μm. The co-polar transmission losses of -0.9 dB through the PSG is seen as expected from simulation. However, it can be seen that the cross-polar isolation is on average -22.4 dB. From simulation S_{21} results this PSG should perform at the -25 dB level.

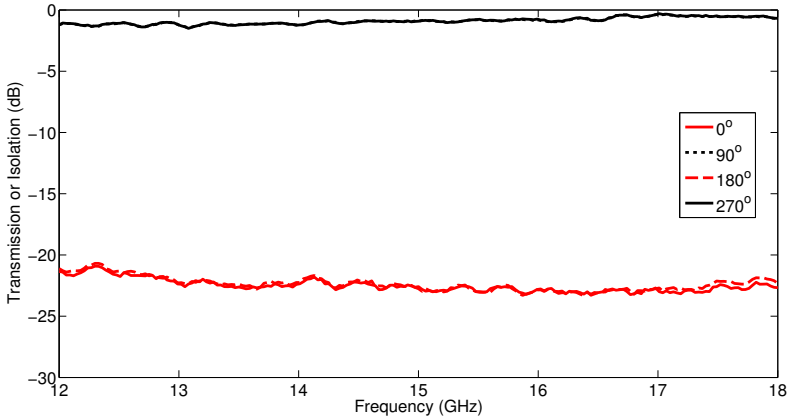

Figure 5.16: S_{21} hardware test results for a PSG $GLD = 5$ μm.

Further PSGs were manufactured using the same technique but with increased *GLD* of metal. The thinnest *GLDs* that consistently performed well were 15 μm. Fig. 5.17 shows a PSG of $GLD = 15$ μm thickness and shows that this PSG performs at the -25 dB level as required. The PSGs are manufactured identically, the only difference being the *GLD*. Therefore the improvement in performance can be attributed to this increase in *GLD*.

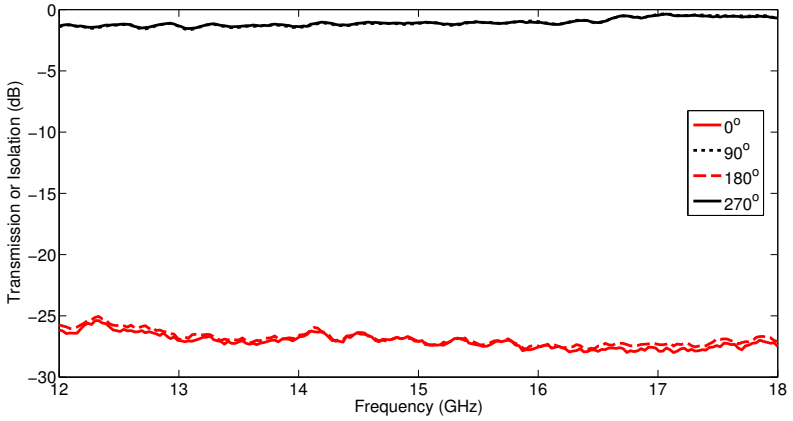

Figure 5.17: S_{21} hardware test results for a PSG with $GLD = 15$ μm.

5.4 GRID LINE DEPTH ITERATION

The minimum *GLDs* calculated from simulation and from experimental measurements are not in agreement. The simulation tends to underestimate the *GLD* required for a -25 dB cross-polar isolation. Further analysis of the simulation and measurement results are required to understand the reasons for the discrepancy and to reduce it. Simulations, even when constructed correctly, do not always yeild the correct answer. This means that different approaches have to be used to solve problems correctly [82].

5.4.1 CURRENT DENSITY RESULTS

Reference [80] states that if the *GLD* is less than twice the skin depth, the current induced in the metal is high throughout the whole GL and the **E**, regardless of orientation, will be able to pass though the GLs to some extent. To assess this effect in the simulation the current density in GLs of different *GLDs* are presented.

Fig. 5.18 shows the current density inside the metal GL from the simulation. If the *GLD* is 5 times the skin depth (2.5 μm) the current density should show a large decay through its depth. However, Fig. 5.18A, shows that although the current does decay with the depth, it starts to increase again towards the bottom of the GL. When the GL is 30 times the skin depth (15 μm) the current density fully decays through the depth of the GLs and will perform as a PSG, as shown in Fig. 5.18B. This insight explains the discrepancy between the simulation and experimental result.

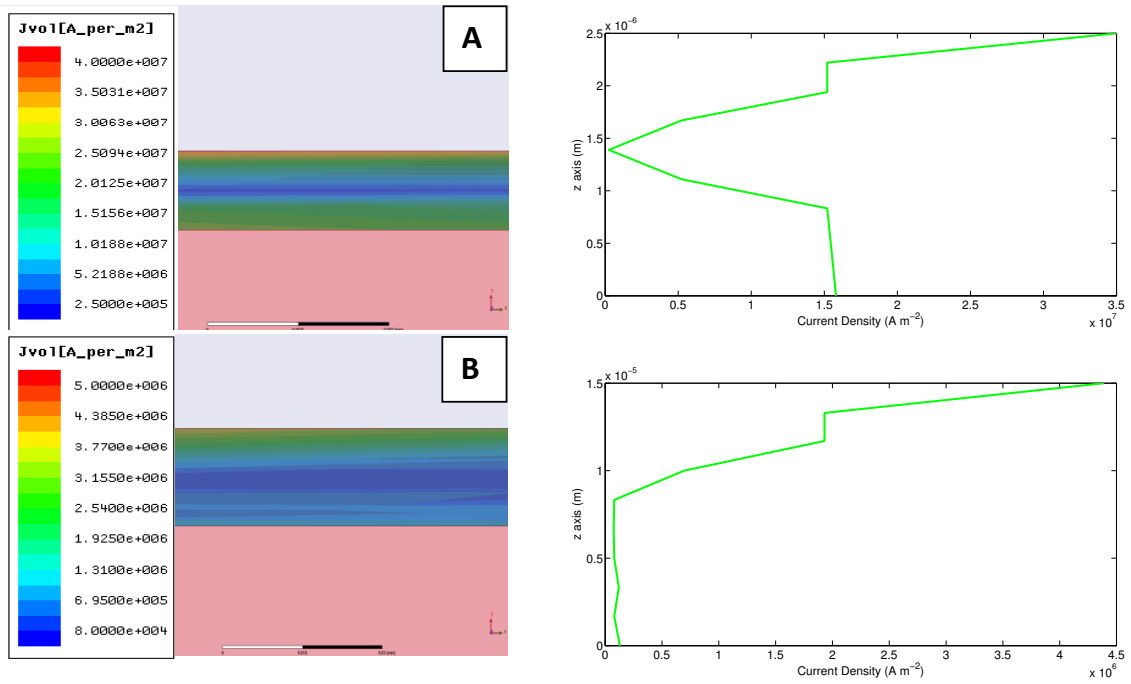

Figure 5.18: Current density variation through the conductive GLs with incident **E** field vector parallel to the GLs. A) Copper $GLD = 2.5$ μm. B) Copper $GLD = 15$ μm. Air box is above the GL (pale blue), reflector dielectric substrate is below (pink).

5.5 CHAPTER SUMMARY

A full field simulation of the **E** fields outside and inside a set of parallel thin GLs has been performed. With additional work looking at the current density it was found to match experimental measurement of a very thin grid. This has been used to determine the minimum depth of thin metal GLs required to provide a sufficient level of cross-polar isolation and low co-polar transmission loss. The simulation and measurement results have been shown to correlate. To manufacture a functioning PSG from a metal deposition process, the grid has to be at least 15 μm, 30 times the skin depth, to ensure a cross-polar isolation of better than -25 dB. For the PSG to work at 15 GHz the *GLW* should be 1.03 mm and the *GLP* 1.92 mm. In simulating thin metal GLs to function as a polarisation grid, it is not sufficient to look at the S_{21} performance. The current density within the metal GL must be considered and be fully decayed through the *GLD*.

The next chapter continues to investigate the design improvement of a TRMAS, and details the design and test verification of a TRMAS radome for minimum transmission loss.

Chapter 6

DESIGN AND TEST VERIFICATION OF A RADOME FOR MINIMUM TRANSMISSION LOSS

6.1 INTRODUCTION

This chapter presents a novel and improved process to define the *RMT* of a radome. The approach described in this chapter is a specifically written 2-Dimensional (2D) ray tracing method written in MATLAB which is based on the geometry of a TRMAS. This outputs an average angle which is used as the input to a unit cell HFSS simulation. The output of the optimisation in the HFSS simulation is the optimal thickness of the radome in question. This result is then verified by further simulation and hardware test.

6.1.1 THICKNESS FROM TRADITIONAL TECHNIQUES

The radome under investigation in this thesis is manufactured from BTCy-1, a pre-preg laminar composite material, $\epsilon_r = 3.6$. Therefore, using Equations (6.1) and (6.2) the *RMT* of this radome can be calculated to be 5.1 mm for normal incidences. To maximise the antenna aperture and reduce transmission losses n should be kept as low as possible, if manufacturable then ideally n = 1.

$$\lambda_m = \frac{\lambda_0}{\sqrt{\epsilon_r}} \tag{6.1}$$

$$NMT \;=\; \frac{n\ \lambda_m}{2} \tag{6.2}$$

6.1.2 CHOICE OF RADOME SHAPE TO OPTIMISE

The radome shape to be optimised in this thesis is a Von Kármán with $\mathbf{C} = 0$ which gives the LD-Haack body for minimum drag during flight as described by Equations (6.3) and (6.4). Where x (m) is the distance along the length (L (m)) of the radome at any given point with the corresponding angle (θ_v (radians)). R (m) is the radius of the radome. This shape is optimised for areodynamic properties, as it gives minimum drag for a given length and diameter, but is undesirable for RF beam quality due to the sloped sides and pointed tip. The radome on an airborne system is a compromise between aerodynamical and RF performance. Therefore, this work will look at a pointed radome that causes differential aberration and therefore is not inherently good in the RF and show what improvements can be made.

$$\theta_v = \arccos\left(1 - \frac{2x}{L}\right) \tag{6.3}$$

$$y = \frac{R}{\sqrt{\pi}}\sqrt{\theta_v - \frac{\sin(2\theta_v)}{2} + \mathbf{C}\sin^{\mathbf{3}}\theta_{\mathbf{v}}} \tag{6.4}$$

6.1.3 COMBINED APPROACH FOR RADOME DESIGN

Traditional methods of defining *RMT* have been shown to be time consuming and rely on an iterative approach in manufacture. These are either based on equation approximations, complex ray tracing or electrically large EM simulations. Completing a full detailed EM simulation of the radome antenna structure and optimising the radome thickness will be accurate if sufficient time and computing resources are available.

This chapter will describe a novel approach which combines 2D Ray Tracing Model (2DRTM) and an electrically small unit cell EM simulation to determine the RMT. This will reduce the time by 3 orders of magnitude and Computer Processing Unit (CPU) resources required by 2 orders of magnitude to complete the optimisation whilst maintaining accuracy. The process is outlined in Fig. 6.1 and will be discussed in further detail in the following sections.

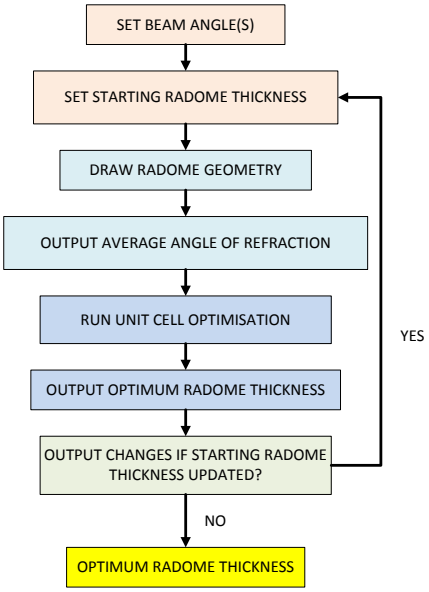

Figure 6.1: 2DRTM and HFSS unit cell model flow chart for combined approach of radome design presented in this chapter.

6.2 2D RAY TRACING

The ray tracing approach is valid for situations, as presented in this chapter, where diffraction is not a main effect. The 2DRTM is written in MATLAB. In summary the simulation creates the required geometry for the TRMAS and radome under investigation and traces the path of a ray from the twist plate and calculates the refraction at both radome and air boundaries; and determines the position where the ray travels to infinity.

The following sections describe custom written MATLAB scripts which define the developed 2DRTM.

6.2.1 MODEL GEOMETRY CONSTRUCTION

Initially in the 2DRTM the geometry of the model is set up. The 2DRTM sets up the external geometry of the radome, which is a Von Kármán Ogive with $\mathbf{C} = 0$ followed by a parallel section of length 0.1 m, Fig. 6.2. Equations (6.3) and (6.4) define the shape of a Von Kármán surface. The axial length of the Von Kármán section is set so the external

diameter is 0.2 m. The internal geometry of the radome is drawn to give a constant wall thickness using the external geometry as the defining surface. The initial thickness chosen is the nominal thickness of 5.1 mm as calculated previously.

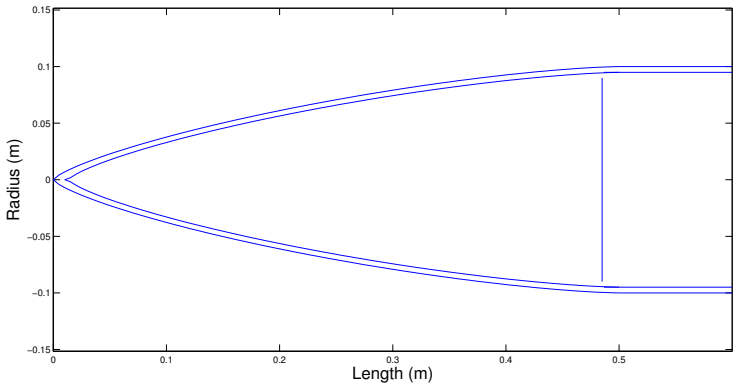

Figure 6.2: 2DRTM geometry of the TRMAS with radome at a beam angle of 0^o.

A TRMAS geometry can be simplified to parallel rays emerging from the twist plate. The twist plate diameter is maximised in the available volume as 0.09 m. The simulation allows the movement of this twist plate to scan the beam 40^o away from the central axis.

Now that the geometry of the radome and twist plate have been set up the path of a ray can be determined.

6.2.2 SINGLE RAY PATH CONSTRUCTION

In this chapter an example ray is run at a beam angle of 0^0 where a parallel ray has been reflected off the twist plate.

At the intersection of the ray with the radome refraction will occur as the RF can travel through the radome. The refraction at the air to radome boundary is calculated using a form of Snell's law, Heckbert's method [83]. Heckbert's method, Equation (6.5), allows the incident and refracted angles to be calculated by using **I**, the unit vector of the incident ray's direction and **N** the surface normal unit vector. **N** is calculated from the gradient

of the surface where the ray intersects.

$$\cos\alpha_i = -\mathbf{I}\cdot\mathbf{N}$$
$$\cos\alpha_r = \sqrt{1-n^2\left(1-\cos\alpha_i^2\right)} \tag{6.5}$$

As defined by Equation (6.5) the ray then travels through the radome. At the radome air boundary refraction occurs again, as defined by Equation (6.5), and the ray then travels out of the radome and away from the antenna, as shown in Fig. 6.3.

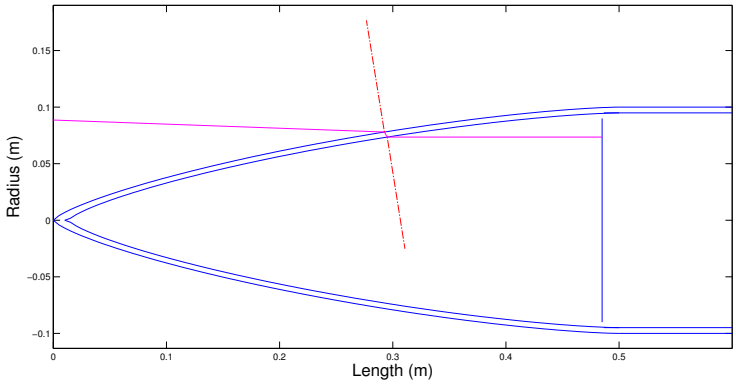

Figure 6.3: 2DRTM TRMAS and radome with an example ray, twist plate at a beam angle of 0^o.

In the 2DRTM, the twist plate can be scanned between a beam angle of $\pm$ 40^o, to move the direction of the beam. To allow for this movement the 2DRTM has been written to automatically detect the intersections between the different sections. This means that the simulation can be run at different beam angles by changing only the twist plate angle. As examples Fig. 6.3 shows the ray tracing at a beam angle of 0^o and Fig. 6.4 shows the ray tracing at a beam angle of 40^o.

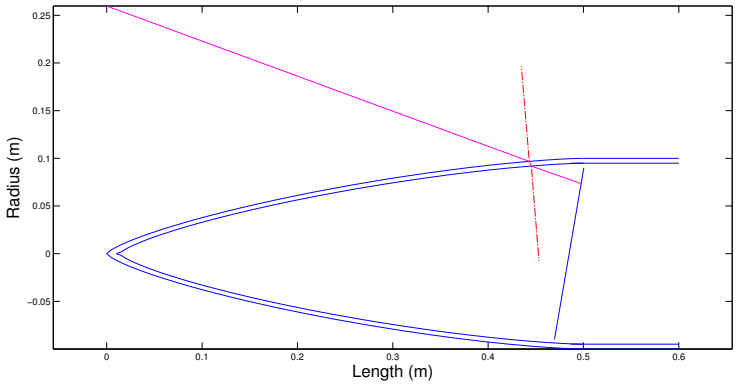

Figure 6.4: 2DRTM TRMAS and radome with an example ray, twist plate at a beam angle of 40^o.

6.2.3 EXTENSION TO MULTIPLE RAYS

Now the geometry and the path of a single ray has been set up, the 2DRTM is extended to use multiple rays. The quantity required from the 2DRTM is the angle of refraction (α_r) on the outgoing ray as a function of ray start position at a particular twist plate angle. The average of this range of angles of refraction is used as an input to the HFSS unit cell simulation.

The 2DRTM is altered so that a band of parallel rays emerge from the twist plate. Fig. 6.5 shows such a selection of rays, at 0.1 mm spacing and the aberration caused as they pass through the radome, with the twist plate at a beam angle of 0^o. The gap in the rays at the centre of the twist plate are due to the blockage caused by the feed. This spacing clearly shows how the ray tracing works for a ray bundle. As the required parameter from this simulation is the α_r between the normal and the exit ray the ray spacing is decreased to 0.01 mm to give a higher density of rays and a more accurate answer, Fig. 6.6.

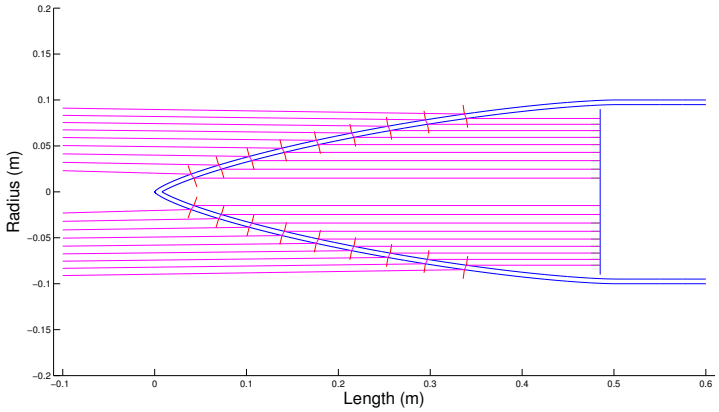

Figure 6.5: 2DRTM TRMAS and radome with a ray bundle at 0.1 mm spacing at a beam angle of 0^o. Gap in the centre is due to the feed horn.

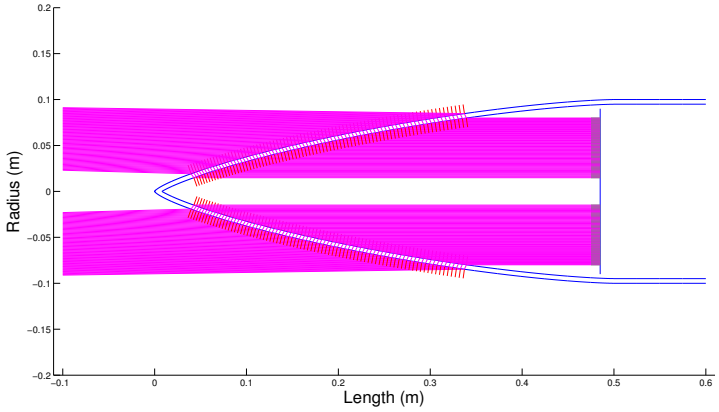

Figure 6.6: 2DRTM TRMAS and radome with a ray bundle at 0.01 mm spacing at a beam angle of 0^o. Gap in the centre is due to the feed horn.

The range of angles of refraction that come out of the 2DRTM with 0.01 mm ray spacing is shown in Fig. 6.7. The α_r ranges from 81.1^o to 68.8^o, with the average α_r being 76.5^o. The symmetrical nature of this can be clearly seen in Figs. 6.5 and 6.7 with the gap around the centre of the starting position due to the feed horn, and at this twist plate angle, coincident with the radome tip. This allows the minimum, mean and maximum angle of refraction to be calculated.

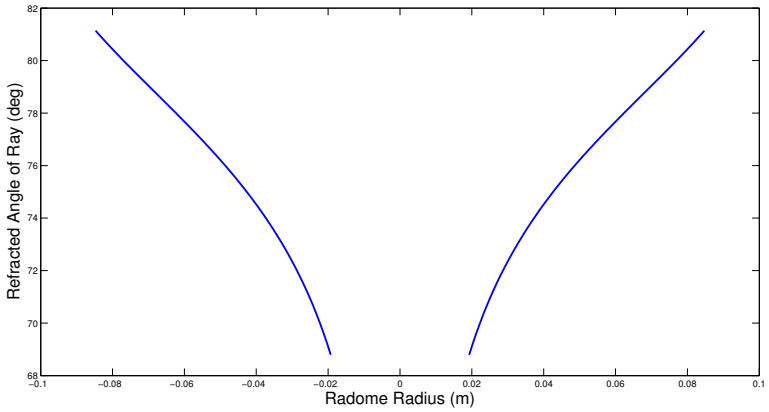

Figure 6.7: α_r for exit rays from a 2DRMT TRMAS and radome at a beam angle of 0^o. Gap in the centre is due to the feed horn.

The 2DRTM is then altered so that it is run over a range of twist plate angles. From this the minimum, mean and maximum angle of refraction can be plotted as a function of beam angle, Fig. 6.8.

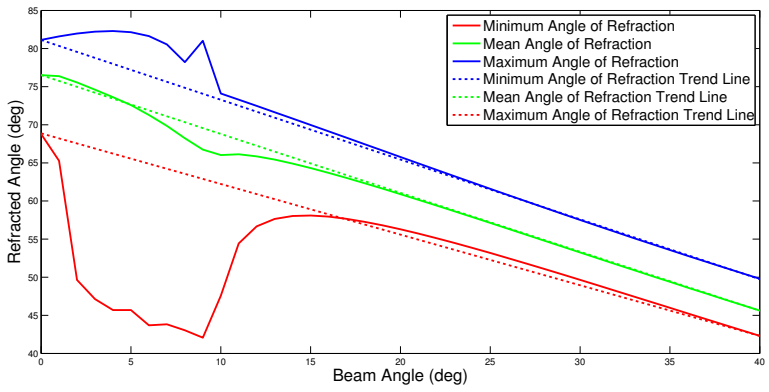

Figure 6.8: α_r for a 2DRMT TRMAS and radome as a function of beam angle with trend line overlaid.

Fig. 6.8 shows that there is a change in the trend and range of α_r for beam angles between 1^o and 15^o. It can be seen that the trend overall as a function of beam angle remains the same, but the specific values in this range deviate. This is because this is where the rays pass through the tip of the radome and are disturbed from the straight path of the bundle due to the different refraction through the sharp gradient around the nose, Figs. 6.9 and 6.10. Unfortunately there is no way of avoiding this occurring unless the geometry of the

radome is altered.

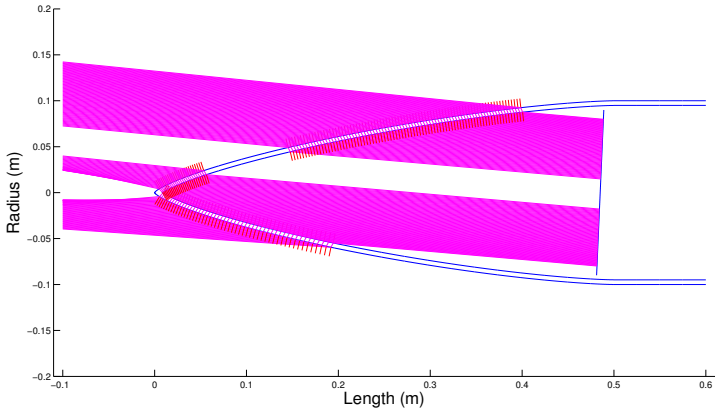

Figure 6.9: 2DRTM TRMAS and radome with a ray bundle at 0.01 mm spacing at a beam angle of 5^o. Gap in the centre is due to the feed horn.

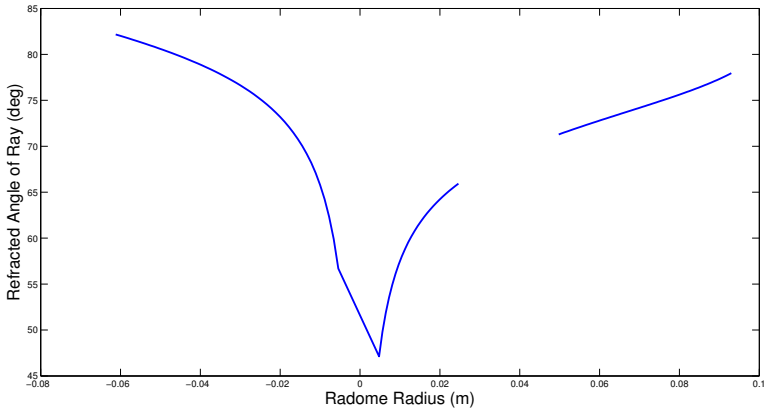

Figure 6.10: α_r for exit rays from 2DRMT TRMAS and radome at a beam angle of 5^o. Gap in the centre is due to the feed horn.

6.2.4 OUTPUT FROM RAY TRACING

The average α_r at a beam angle of 0^o is 76.5^o as measured from the 2DRTM. This value will be used as an input to the unit cell model in HFSS to define the *RMT* for maximum transmission at the required beam angle. As antennas are reciprocal this α_r on transmission is the α_i in receive mode. For ray tracing it is easier to think in terms of transmission, but for the unit cell model it is easier to think in terms of receive. Therefore $\alpha_r = \alpha_i = 76.5^o$.

Now an α_i has been calculated Equation (6.6) can be used to calculate the thickness of the radome. Using $\alpha_i = 76.5^o$ and n = 1 the thickness of the radome is calculated to be 5.91 mm.

$$NMT = \frac{n\ \lambda_0}{2\sqrt{\epsilon_r - \sin^2 \alpha_i}} \tag{6.6}$$

6.3 UNIT CELL MODEL

This unit cell model will be completed in HFSS. It is an electrically small model that is quick to run. It takes the input of the average angle of incidence from the ray tracing model and varies the thickness to optimise it for minimum loss. The simulation is readily run on a 4 GB machine.

6.3.1 SET UP OF RADOME UNIT CELL MODEL

To optimise the thickness of the radome in the RF window a HFSS simulation was constructed. The geometry is a flat sheet of radome material (pink) of parameterised thickness with an air box (blue) around it that is in excess of half the wavelength at f = 15 GHz, Fig. 6.11. The radome material is BTCy-1, with a $\epsilon_r = 3.6$ and $\tan\delta = 0.004$, losses are included. Floquet ports are used so the model becomes a repeated structure infinite in size, but it remains electrically small so it remains quick to solve. The α_i of the radiation can be altered between 0^o, which is perpendicular to the top face of the radome, and 90^o, which is parallel to the top face of the radome. Because of reciprocity this is equivalent to the α_r found in the MATLAB simulation. The change in angle alters the path length through the radome. The angle is set according to the calculated α_i in the ray tracing model, $\alpha_i = 76.5^o$.

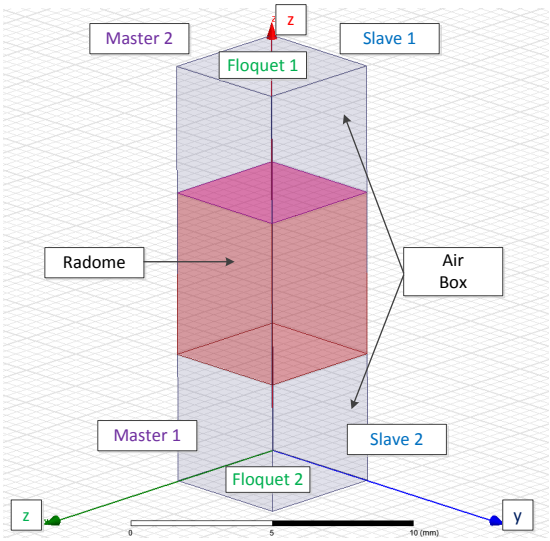

Figure 6.11: HFSS unit cell model used to optimise radome thickness.

6.3.2 INITIAL UNIT CELL OPTIMISATION RESULTS

In HFSS the Quasi Newton optimization tool [84] was used to determine the *RMT* for a given α_i. For this investigation a single f = 15 GHz will be used as the optimisation frequency. The optimisation was set to optimise the thickness of the radome at $\alpha_i = 76.5^o$ with an S_{11} value of -32 dB and a convergence criteria of 1 e^{-6}, Equation (6.7), these values are derived from experimentation and good engineering practice. Great care must be taken to assign these values correctly, or the final result of the S_{11} optimisation will be invalid. The results are shown in Fig. 6.12 and a thickness of 6.136 mm can be seen as the *RMT*.

$$RMT \;=\; \underset{S_{11}}{min}\,(\alpha_i, RMT) \tag{6.7}$$

To check the output of the parameterisation, and show that multiple answers are available a parametric sweep of radome thickness ranging from 0 to 30 mm in 0.1 mm increments was run using the unit cell simulation, with $\alpha_i = 76.5^o$. Fig. 6.13 shows how the S_{11} value changes as a function of radome thickness. Looking at the S_{11} plot a minimum reflection loss is required, i.e. the highest transmission of energy, for a functioning thickness. It can be seen that there are multiple resonances, occurring at 0, 6.1, 12.3, 18.4 and 24.5 mm. The lowest practical value of S_{11} is -23.71 dB at 6.1 mm. The other resonances could be

used, but to minimise the transmission losses a thin radome is required. The 10 dB width across the troughs remains stable at around 0.4 mm.

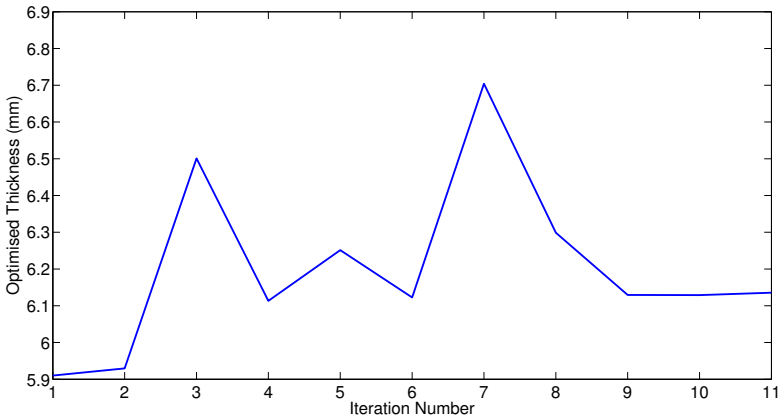

Figure 6.12: HFSS unit cell radome thickness optimisation results at $\alpha_i = 76.5^o$.

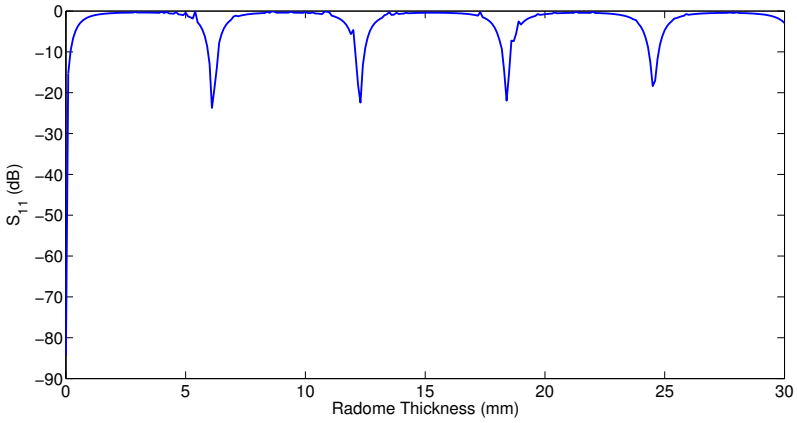

Figure 6.13: HFSS unit cell simulation results for $\alpha_i = 76.5^o$ as a function of radome thickness in 0.1 mm steps.

To achieve the required accuracy the simulation is re-run at 0.001 mm increments over the thickness range of interest: 6 to 6.2 mm. Fig. 6.14 shows that the *RMT* to manufacture is between 6.134 and 6.135 mm with a value of S_{11} of -31.02 dB, which is at maximum 0.002 mm from the *RMT* validating the optimisation input choices. In practice, this wide range of thicknesses will not need to be simulated and time can be much reduced by simulating only the small area around the required values, this range has been shown for illustrative purposes only.

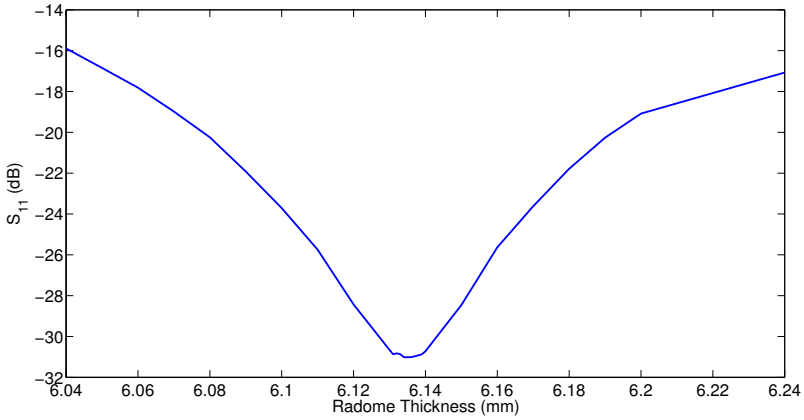

Figure 6.14: HFSS unit cell simulation results for $\alpha_i = 76.5^o$ as a function of radome thickness in 0.001 mm steps.

Figs. 6.15 and 6.16 shows the S_{21} results for the same simulation, where the minimum transmission loss is the *RMT*. The fringing effects seen in Fig. 6.15 are an artefact of the unit cell simulation, they are not real features and should be ignored. This again shows resonances at the same thicknesses, with the resonance at 6.1 mm on the coarse scale graph, Fig. 6.15, and 6.136 mm on the fine scale graph, Fig. 6.16, as having the lowest transmission loss. This again validates the optimal thickness calculation. However, the peak of the S_{21} is broader than the null of the S_{11} making it harder to calculate the point of inflection. Therefore S_{11} results will be used.

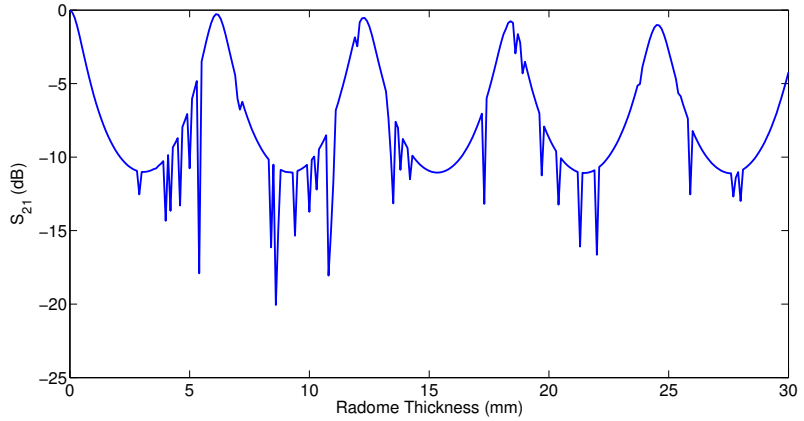

Figure 6.15: HFSS unit cell simulation S_{21} results for $\alpha_i = 76.5^o$ as a function of radome thickness with 0.1 mm steps.

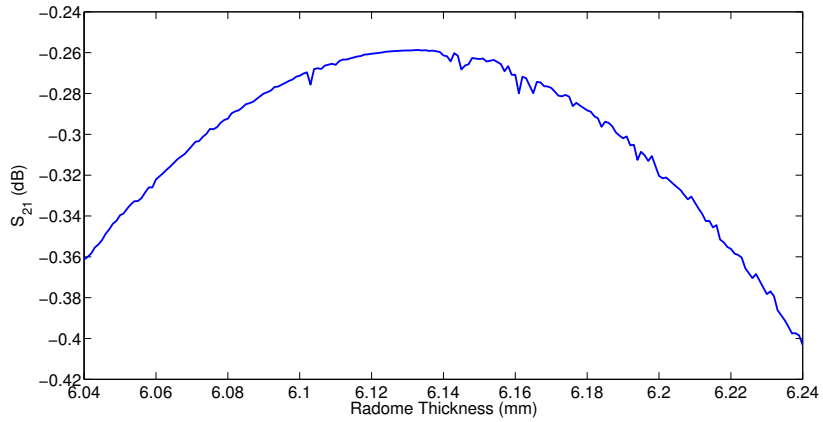

Figure 6.16: HFSS unit cell simulation S_{21} results for $\alpha_i = 76.5^o$ as a function of radome thickness in 0.001 mm steps.

To verify this value with a different approach a second simulation was conducted. Again using a unit cell simulation, but this time the thickness of the radome is set to 6.136 mm and the incident angle is swept from 0 to 90^o in 0.01^o steps, Fig. 6.17. This shows that the lowest reflection value is 76.4^o, which is 0.1^o away from the previous value calculated and verifies the value from a different method.

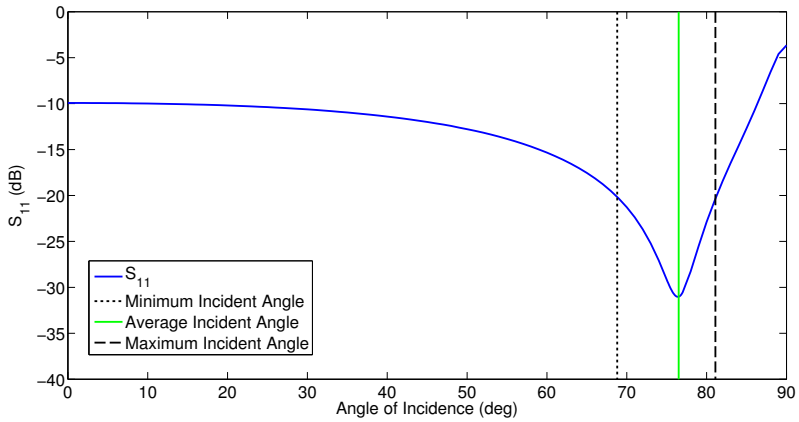

Figure 6.17: HFSS unit cell simulation results for radome thickness of 6.135 mm as a function of α_i.

This means that the *RMT* of the radome is 6.136 mm. This is 1.036 mm different to the value of thickness calculated from Equations (6.1) and (6.2) that was used as the input for the ray tracing. If the radome is manufactured to the calculated value of 5.1 mm then it can be seen from Fig. 6.15 that the loss through the radome is 6 dB, rather than the

optimised 0.27 dB.

6.4 ITERATION OF 2DRTM AND UNIT CELL MODEL

Due to the difference between the starting thickness of the radome used as an input to the 2DRTM and the end thickness of the radome it is valuable to determine if an iteration of the design process is required before finalising the optimal thickness of the radome.

The 2DRTM is re-run at the new radome thickness of 6.136 mm and the difference between these results and those calculated at 5.1 mm are shown in Fig. 6.18. At a beam angle of 0^o there is no change in the minimum, mean and maximum angles of refraction, this is the same past 14^o. If the optimisation was to occur at a different scan angle, or over a range of scan angles, then the 2DRTM and HFSS unit cell simulation would have to be iterated to achieve an accurate result. However, at an angle of 0^o the simulations do not have to be iterated and the optimal radome thickness is defined as 6.136 mm with the new approach to radome thickness definition.

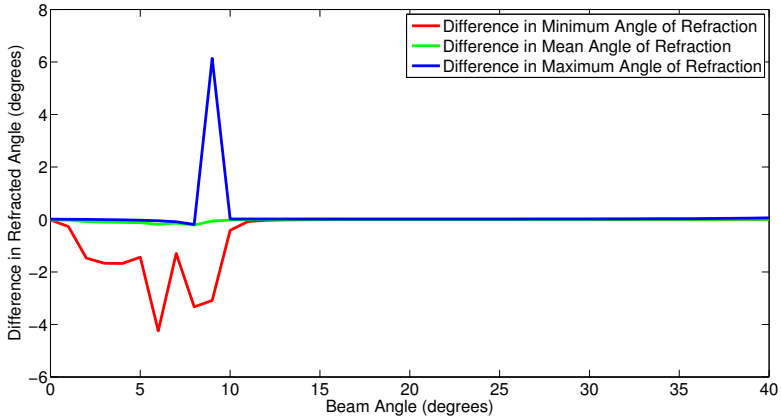

Figure 6.18: Difference in α_r for a 2DRTM TRMAS and radome as a function of beam angle with a radome thickness of 5.1 mm and 6.135 mm.

Now an α_i and an RMT has been calculated Equation (6.6) can be used to calculate the thickness of the radome. Using $\alpha_i = 76.5^o$ and n = 1 the thickness of the radome is calculated to be 5.9 mm. This is much closer to the optimised value of 6.136 mm as calculated by the method presented in this chapter.

6.5 RADOME AND ANTENNA HFSS MODEL

This section contains the results of a simulation of the radome and antenna HFSS model, Fig. 6.19. A simplified TRMAS is to be simulated. Again, a set of parallel rays are to be projected from the twist plate. In this simulation this is achieved by using a front fed parabola. This simulation is detailed enough to calculate the gain as a function of thickness, whilst removing the full geometrical complexity that would extend the simulation time to 26 hours, with no change in the results. A generic single pyramidal horn feed is used as the feed which is situated at the focus of a metal paraboloid. An air box (vacuum) is constructed around the radome with a radiation boundary set up at edge of this vacuum. A wave port is set up at the input end of the feed because it is inside the air box. To look at the gain of the system infinite radiation spheres are set. Conductor and dielectric losses are included in the simulation. The thickness of the radome is constructed as a parameter, and the gain of the system is simulated as a function of radome thickness. For a single frequency, beam angle and radome thickness this simulation takes 51:15 minutes to run on a distributive computing system with 96 cores and 576 GB total memory capacity. It was not possible to run this simulation as an optimisation as there was not enough memory available, therefore it is run multiple times at difference thicknesses. The same simulation can be run on a 48 GB stand-alone machine, but it takes 26 hours to run, it cannot be run on a 4 GB machine.

Fig. 6.20 shows the results for the gain as a function of radome thickness for the full radome and antenna HFSS model in 0.1 mm increments over the range of interest of 4.6 to 6.2 mm. The range of thickness covered has to start below the calculated value of thickness of 5.1 mm and continue until a peak is found at 6.1 mm.

From the peak gain found at 6.1 mm the next simulation range is chosen as 6.1 to 6.2 mm thickness in 0.01 mm stages, Fig. 6.21. It can be seen that the peak gain is found at a thickness of 6.14 mm.

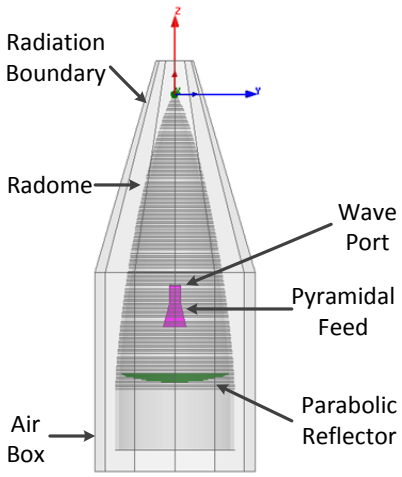

Figure 6.19: HFSS full model simulation set up for a radome and antenna model.

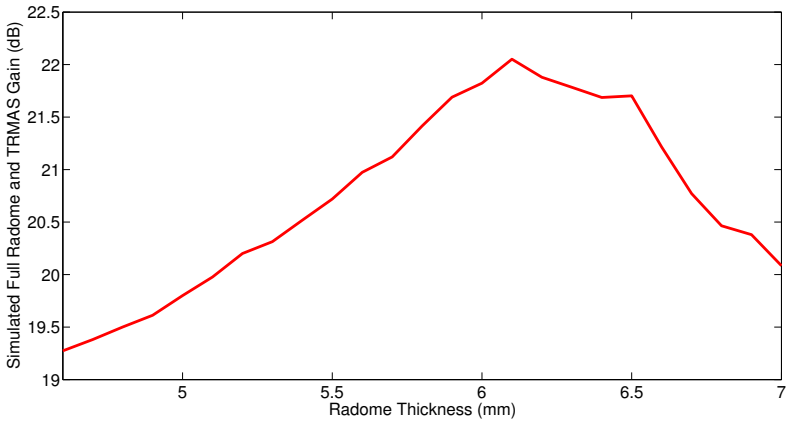

Figure 6.20: HFSS full model simulation results at 0.1 mm spacing.

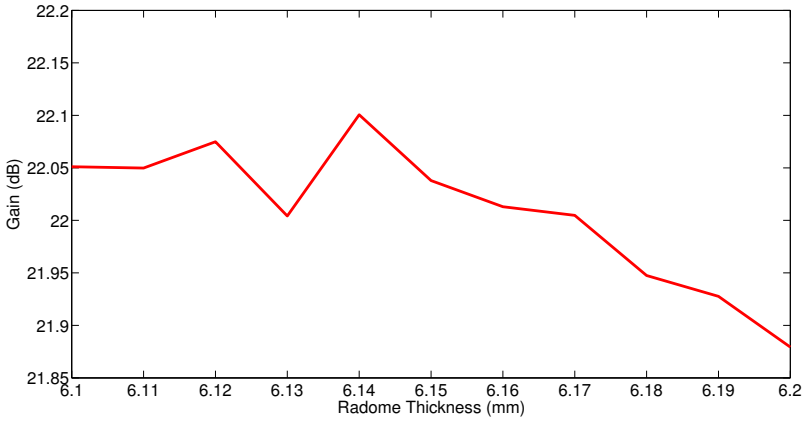

Figure 6.21: HFSS full model simulation results at 0.01 mm spacing.

From the peak gain found at 6.14 mm the next simulation range is chosen as 6.127 to 6.142 mm thickness in 0.001 mm stages, Fig. 6.22. It can be seen that the maximum gain, i.e. the *RMT*, occurs at a thickness of 6.132 mm. The gain variation over this band width is only 0.14 dB, this level is below measurement tolerance and therefore is below measurement accuracy, and shows the noise level in this simulation.

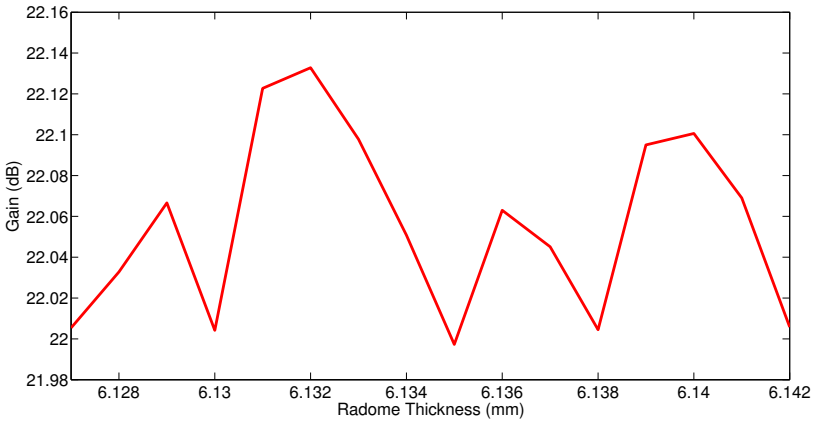

Figure 6.22: HFSS full model simulation results at 0.001 mm spacing.

The overall optimisation of the radome thickness has taken 44 simulations and 41 hours of simulation time.

6.6 COMPARISON OF APPROACHES

It can be seen that both approaches presented in this thesis give a very similar value for the *RMT*, therefore both methods are suitable for use. The difference between the methods is 0.004 mm. This difference in thickness leads to a drop in gain of 0.07 dB in the full HFSS simulation, which is negligible in a real system. Indeed, in reality a standard machining tolerance is $\pm$ 0.1 mm, which means a thickness of 6.13 mm would be chosen in both cases as the manufacturable thickness.

As the two approaches give the same answer, the real difference between them is the time taken. The following analysis will not include the set up time of the models and will only consider the run times. Table 6-A shows that the approach described in this thesis, of using a combination of MATLAB and HFSS, speeded up the simulation time by 822 times,

and reduced the memory required by 144 times.

SIMULATION	**TIME TAKEN (MINUTES)**	**MEMORY (GB)**	**ITERATIONS**
MATLAB RAY TRACING	0:12	4	potentially 1
HFSS UNIT CELL	2:44	4	potentially 1
HFSS	51:15	576	~ 47

Table 6-A: Comparison of simulation times and CPU for radome thickness calculations.

The new method presented in this thesis is able to be adjusted to new geometry shapes, as it is a simple matter of altering the geometry of the radome in the MATLAB ray tracing. The HFSS unit cell model would only require a change of radome material and scan angle. The full HFSS antenna and radome simulation will take several days to construct and successfully simulate. Therefore the approach designed in this thesis will be quicker to set up the simulation for a new antenna and radome system. However, it is often still important to still have a mechanically accurate HFSS model of your system, for other tuning work that you may wish to complete.

The thickness calculated from the simulations will now be tested in hardware in an AC.

6.7 RADOME AC TESTING

Radome testing was carried out in an AC with a TRMAS, the gain was measured as described in Chapter 3. The thickness of the radome was determined as an average of 20 thickness measurement points across the RF window. Radomes of different thicknesses were tested with the same antenna at a beam angle of 0^o, the gain as a function of radome thickness is shown in Fig. 6.23. Due to the cost of the units it was not possible to manufacture a large number of radomes that were known to be incorrect. However, one unit was manufactured 2.031 mm under thickness, and bottom, middle and top of tolerance units have been used to show the range in gain performance.

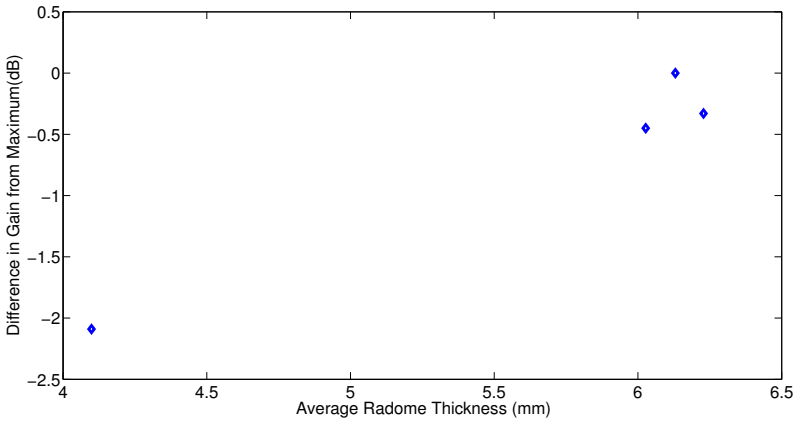

Figure 6.23: AC measurement results of gain for a TRMAS with radome.

Fig. 6.23 shows that the radome thickness has an impact on the gain. The highest gain is found from the calculated thickness of 6.13 mm thus validating the design process. The two points either side of the peak are at approximately ± 0.1 mm and are less than 0.5 dB down on the peak gain. This shows that the machining tolerances of the unit are valid. The one outlier at -2 mm clearly shows a 2 dB drop in gain.

6.8 DIELECTRIC CONSTANT VARIATION

As the radomes are manufactured by a manual technique there is expected to be a small variation in ϵ_r across the unit and from unit to unit. The allowable variation in ϵ_r is set to ± 5 %. Fig. 6.24 shows the results from running the optimised thickness in the unit cell model as a function of ϵ_r. It can be seen that there is a trend in decreasing thickness with increasing ϵ_r. A ± 5 % change in ϵ_r gives at maximum a thickness change of 0.226 mm, which leads to a decrease in performance of 0.36 dB. When the full HFSS simulation is run with a ± 5 % change in ϵ_r there is no change in peak sum pattern gain.

From the ϵ_r measurements taken on the manufactured radomes a graph showing the measured ϵ_r and gain can be produced, Fig. 6.25. This shows the manufactured unit to unit variation of the ϵ_r being 0.1, equivalent to 2.7 %, and being independent of radome performance.

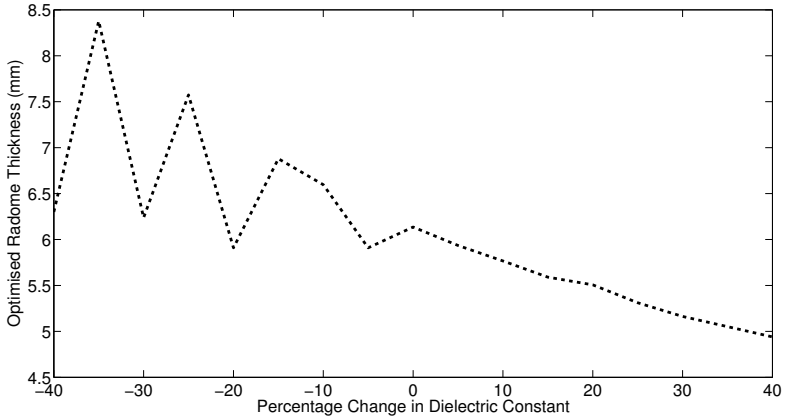

Figure 6.24: Unit cell optimisation results for thickness of radome as a function of ϵ_r.

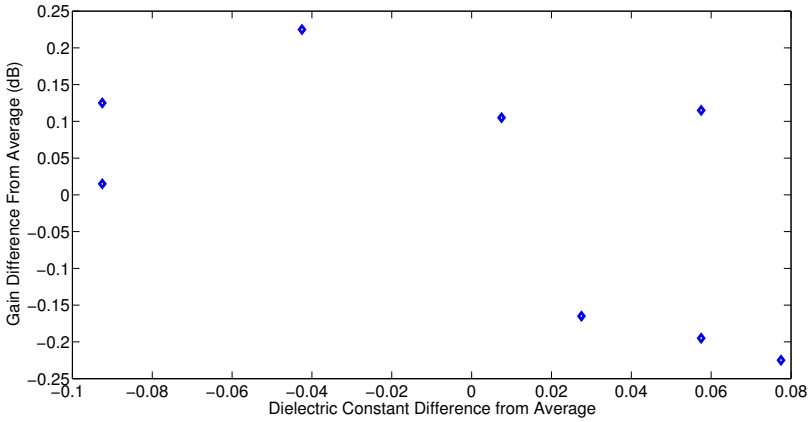

Figure 6.25: Gain range caused by ϵ_r variations in manufactured units.

6.9 CHAPTER SUMMARY

This chapter describes and validates a new method for the optimisation of the thickness of a radome. This new method reduces the time to calculate the optimal thickness of a radome by 3 orders of magnitude and the required computer memory by 2 orders of magnitude without compromising accuracy. The thickness of the radome is validated by AC measurement. The next chapter finalises the investigation into the design improvement of a TRMAS, and details the design and test verification of the formation of TRMAS Σ and Δ signals with compensation for a failed feed element.

Chapter 7

FORMATION OF MONOPULSE SIGNALS WITH COMPENSATION FOR A FAILED FEED ELEMENT

7.1 INTRODUCTION

Monopulse antenna systems are often used in airborne radar as they give angular target information in a single measurement. Monopulse antenna systems send out multiple overlapping beams from the feed ports. The return signals are then re-combined in hardware to form Σ and Δ signal channels which provide angular information about the target.

Comparator networks are typically found in monopulse antenna systems and are used to combine the feed element data into the Σ and Δ signals [85]. It is important that phase and amplitude errors are minimised, as the four ports need to be highly symmetrical and the phase shift introduced by the symmetry requirements taken into account. A comparator is a collection of waveguide, coaxial cables or strip line [86] with dividers and combiners; the exact choice depends on the requirements of the system [22].

In a comparator system, Σ and Δ are created using hardware techniques such as those discussed above and the individual feed element signals are not recorded. If one of the feed elements, transmitters or receivers becomes damaged this signal cannot be readily compensated for and the antenna will no longer function.

This chapter presents clarification of a process by which this combination of monopulse signals can be completed in software by signal processing, Software Defined Combination (SDC), thus removing the requirement for a traditional comparator. This is an approach

that has numerous advantages in terms of space and mass saving and in reducing the complexity of the hardware to be manufactured. It allows the simultaneous availability of Σ and Δ signals without suffering the loss of a comparator.

In this particular example the waveguide comparator had been specifically designed to be compact and lightweight, with a mass of 0.356 kg and a volume of 1.4 x 10^{-6} m^2. Four receivers were used to record the Σ and Δ signals and a processor was present to measure the signals after they had been digitised. The removal of this comparator would result in a direct mass and volume saving of the size of the comparator. The receivers may have to be changed to ones that measure magnitude and phase, and spare capacity has to be available in the processor to complete the additional calculations.

The novel approach of this chapter is to apply a further level of processing to the SDC to enable the antenna system to function satisfactorily if a feed element has failed. This is not possible using a hardware based comparator and has the benefits of extending the functionality of the antenna by allowing it to continue to function in a failure mode.

7.2 Σ AND Δ WITHOUT A COMPARATOR

To combine the 4 feed element signals in software, Equations (7.1), (7.2), (7.3) and (7.4) should be followed [18]. A proof of these equations and verification using AC measurements is to be given below.

$$\Sigma = \frac{A + B + C + D}{2} \tag{7.1}$$

$$\Delta AZ = \frac{(A + C) - (B + D)}{2} \tag{7.2}$$

$$\Delta EL = \frac{(A + B) - (C + D)}{2} \tag{7.3}$$

$$Q = \frac{(A + D) - (B + C)}{2} \tag{7.4}$$

Ideal comparators obey the law of conservation of energy during the formation of the Σ and Δ signals. To combine the 4 feed element signals in software, simply using the addition function would violate the conservation of energy; therefore additional mathematical steps

must be taken.

An antenna can be thought of as a circuit with a voltage source and a load, Fig. 7.1. Where V_S is the voltage source, R_L is the load resistance and R_S is the source resistance.

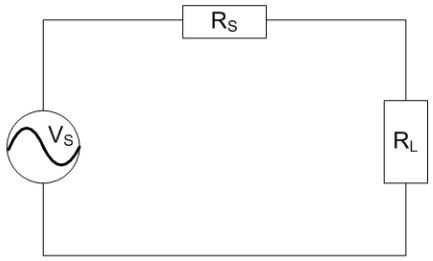

Figure 7.1: Equivalent circuit for an idealised antenna system.

An ideal divider splits its signal into two equal parts in terms of power with no overall loss of power and preserves the phase. An ideal combiner re-combines the split signal without loss of power. These operations are performed twice sequentially inside the comparator. Consider the effect on the power of one divide and combination. Fig. 7.2 shows how two signals are combined. Combining Equations (7.5) and (7.6) gives an expression that relates the Current (I (A)), Voltage (V (V)), Power (P (W)) and Resistance (R (Ω)), Equation (7.7).

$$V = IR \tag{7.5}$$

$$P = IV \tag{7.6}$$

$$V = \sqrt{PR} \tag{7.7}$$

As defined by the combiner, the split is of equal P, thus the P received by each part of the split is shown by Equation (7.8). Therefore the ratio of reduction for V is $1/\sqrt{2}$, as shown by Equation (7.9) and in Fig. 7.2.

$$V = \sqrt{\frac{P}{2}R} \tag{7.8}$$

$$V = \frac{\sqrt{\frac{P}{2}R}}{\sqrt{PR}} = \frac{1}{\sqrt{2}} \tag{7.9}$$

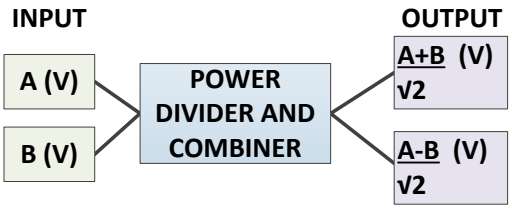

Figure 7.2: Schematic showing how one divider maintains the conservation of P.

Therefore, to create the second combination, the same process is followed and the split occurs again, as shown in Equation (7.10). This means that after two splits V has been reduced by a factor of $1/\sqrt{2}$ twice, as shown by Equation (7.11) and Fig. 7.3. Therefore V has to be divided by 2 to conserve power.

$$V = \sqrt{\frac{P}{4}R} \tag{7.10}$$

$$V = \frac{\sqrt{\frac{P}{4}R}}{\sqrt{PR}} = \frac{1}{2} \tag{7.11}$$

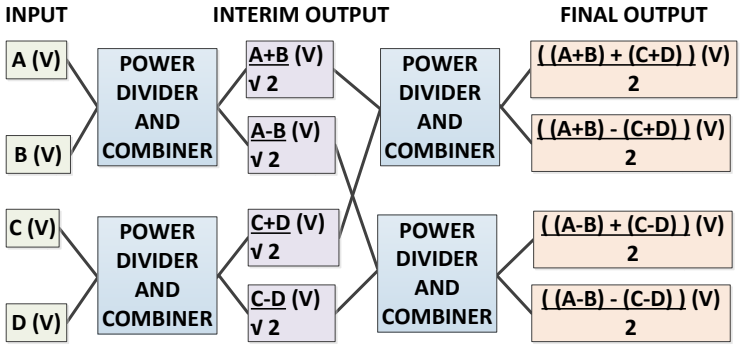

Figure 7.3: Schematic showing how the comparator combination of 4 feed elements maintains the conservation of P.

If the comparator is to be replaced by software processing there has to be spare capacity behind the antenna for these additional requirements, both in terms of power and computer processing. A hardware comparator requires no computer processing power or electrical connection. For the hardware comparator system, typically 3 receivers are required, as the Q channel is not recorded, however, the software alternative requires 4 receivers. In

the following work a CPU and 4 receivers are available.

7.2.1 MEASURED Σ AND Δ PATTERNS

To prove SDC, a TRMAS was tested in an AC with and without a comparator. In place of a comparator, a multiplexer was introduced with additional cables, to allow measurement of the multi-channel antenna. The difference in RF path between these two set-ups was measured and calibrated for, as reported in Chapter 3 [38]. Figs. 7.4 and 7.5 show the radiation pattern cuts for Σ and Δ in AZ and EL produced by traditional comparator and the SDC. To assess the difference between the cuts, the RMS difference for angles at ± 10 degrees from the centre was calculated, ignoring values below -30 dB, where a large numerical difference is actually a small difference in signal. For tracking radar, it is only the angular width of the main beam that is of interest, the selection covered here is greater than this. The additional loss through the traditional comparator has been measured and calibrated for. ΣAZ cut RMS difference is 0.04 dB, ΣEL cut RMS difference is 0.05 dB, ΔAZ cut RMS difference is 0.25 dB, and ΔEL cut RMS difference is 0.31 dB, Table 7-A. These differences between the patterns produced by traditional comparator and the SDC are lower than those found for repeated measurements of the same pattern with the same hardware set up, i.e. they are at the measurement error level, therefore validating this procedure for creating the Σ and Δ signals from the feed element data.

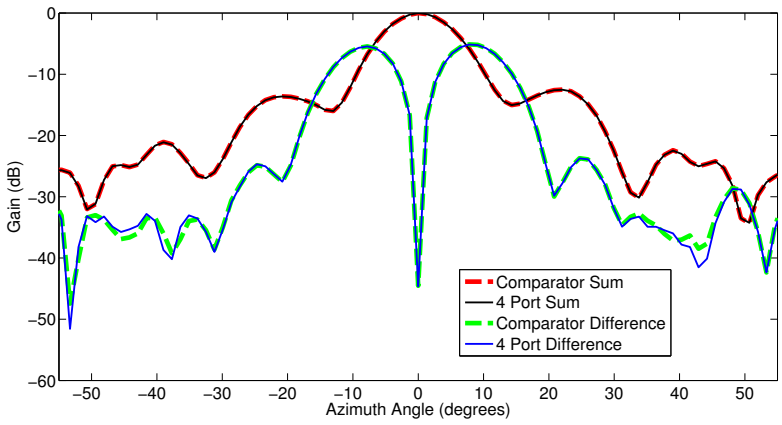

Figure 7.4: Measured Σ and Δ AZ Patterns With and Without a Comparator.

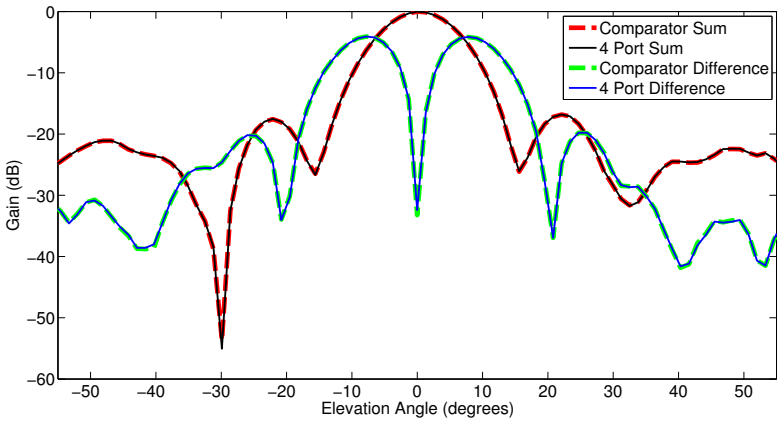

Figure 7.5: Measured Σ and Δ EL Patterns With and Without a Comparator.

CUT PERFORMED	**RMS DIFFERENCE BETWEEN COMPARATOR AND SDC SUMMATION (dB)**
ΣAZ	0.04
ΣEL	0.05
ΔAZ	0.25
ΔEL	0.31

Table 7-A: RMS difference between comparator and SDC summed Σ and Δ pattern.

7.2.2 MEASURED Σ GAIN

Fig. 7.6 shows that the gain as a function of frequency produced by the traditional comparator and the SDC overlay. The additional loss through the comparator has been measured and compensated for. The RMS difference between the Σ was calculated to be 0.04 dB with a maximum difference of 0.18 dB. These differences have been found for repeated measurements with the same hardware set up, i.e. they are at the measurement error level, therefore validating this procedure for creating the Σ gain.

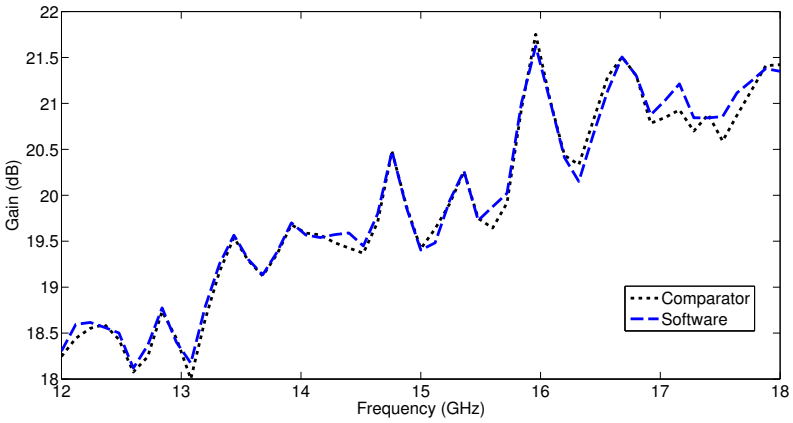

Figure 7.6: Measured gain as a function of frequency for a TRMAS formed with a traditional comparator and by SDC from raw feed element data.

7.3 COMPENSATION FOR A FAILED FEED ELEMENT

7.3.1 SET-UP AND VALIDATION OF SIMULATION MODEL

A MATLAB model of an idealised monopulse antenna was constructed, with feed element diameter 15 cm and offset of 0.05 radians. Using a Bessel function, the beams from each of the antenna feed elements are formed and are completely symmetrical [87]. These beams were formed in 2 dimensions and the position of each beam is shown in Fig. 7.7. It can be seen that each beam is offset from the centre due to its physical position with respect to the centre of the monopulse feed horn. These four beams are summed together as described in Equations (7.1) to (7.3) as phasors and the Σ and Δ formed as shown in Fig. 1.5. It can be seen that this model provides a suitable Σ and Δ pattern from a monopulse antenna and it assumes that the target is in the centre of the monopulse beam.

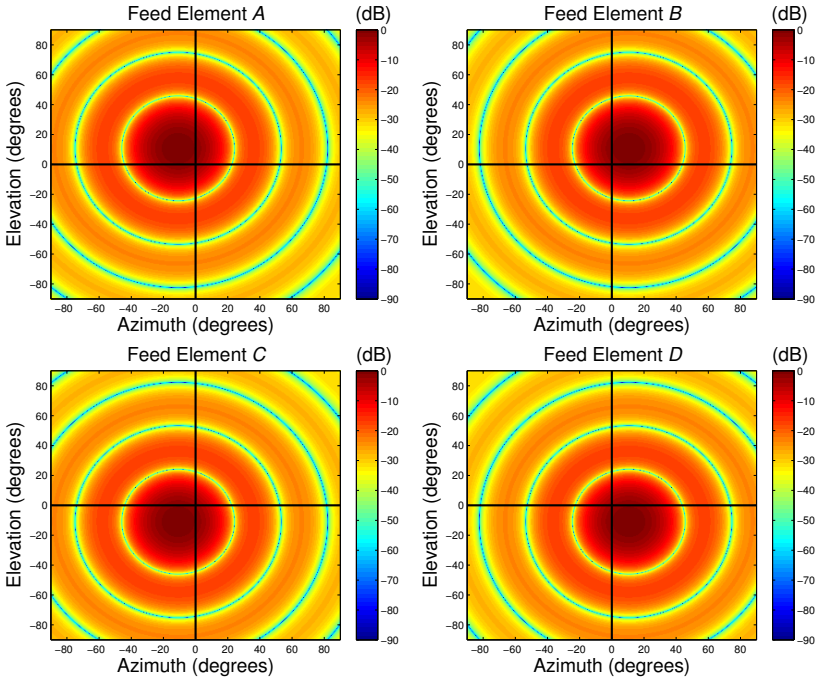

Figure 7.7: Simulated far-field contour plots of individual feed elements of a TRMAS.

With the comparator removed from the system, and the individual signals recorded, the effects of a failed feed element can be detected and compensated for during the formation of the Σ and Δ signals. This is made possible because of the additional data available for processing. Figs. 7.8, 7.9 and 7.10 show how the Σ gain , first side lobe and first null alters when the signal of one of the feed elements is reduced. It can be seen that a reduction in gain of 1 dB in one feed element reduces the Σ gain by 0.23 dB and increases the RMS difference to 0.24 dB. Therefore this level of difference in the feed elements should be compensated for.

The Σ and Δ patterns can now be formed directly from the raw feed element data, and can be created without using the failed feed element, as described by the following analysis.

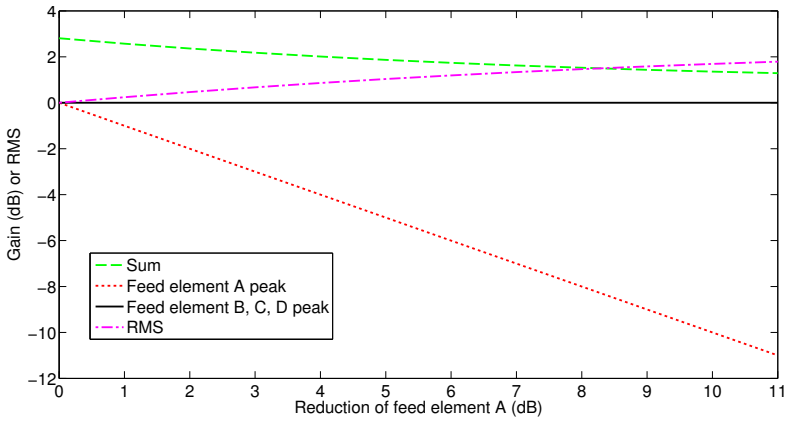

Figure 7.8: Simulated Σ max gain as a function of the loss in one feed element.

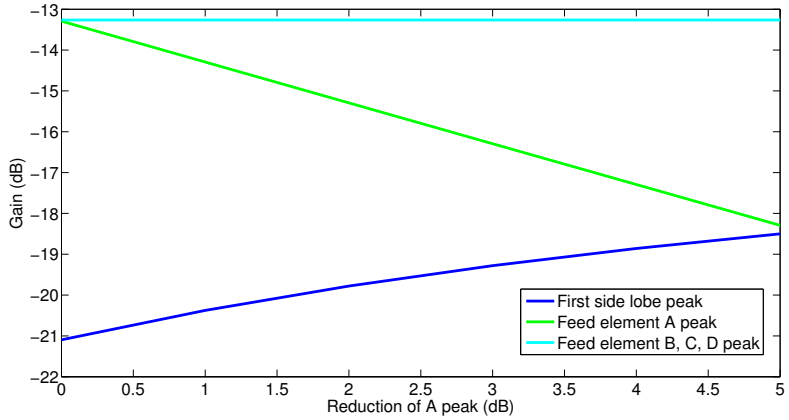

Figure 7.9: Simulated Σ first side lobe peak change as a function of loss in one feed element.

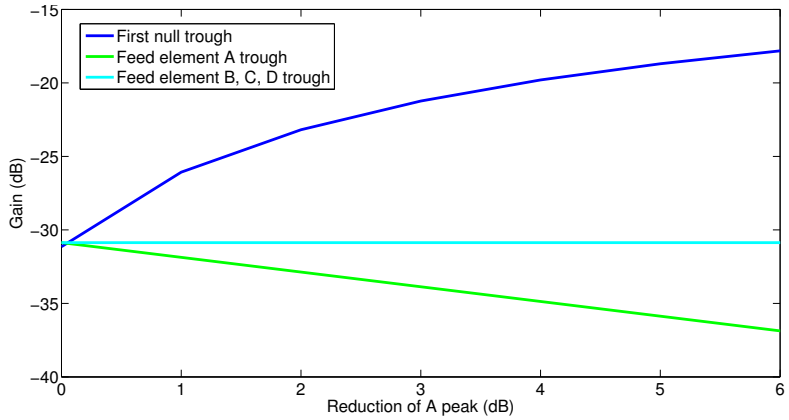

Figure 7.10: Simulated Σ first null level change as a function of loss in one feed element.

7.3.2 COMPENSATION FOR A FAILED FEED ELEMENT IN Σ

In a four port monopulse antenna there are multiple ways in which the Σ pattern can be calculated if a feed element has failed. For the purpose of this analysis, feed element A has been identified as the failed feed element. Permutations to form the Σ signal from the available channels are shown in Equations (7.12) to (7.19) and plotted in Fig. 7.11 and 7.12, where they are compared to the traditional Σ pattern formation. Σ is calculated from Equation (7.1). If the values are un-scaled (Σ_{US}), the missing feed element is simply set to 0. To appropriately scale the value, (Σ_S), a scaling factor is introduced into the numerator to compensate for missing feed element and to preserve the gain. Equations (7.12) to (7.19) show the possible permutations for calculating Σ.

$$\Sigma_S\ BCD = \left(\frac{\frac{4}{3}(B\ +\ C\ +\ D)}{2}\right)^2 \tag{7.12}$$

$$\Sigma_{US}\ BCD = \left(\frac{B\ +\ C\ +\ D}{2}\right)^2 \tag{7.13}$$

$$\Sigma_S\ BC = (B\ +\ C) \tag{7.14}$$

$$\Sigma_{US}\ BC = \left(\frac{B\ +\ C)}{2}\right) \tag{7.15}$$

$$\Sigma_S\ BD = (B\ +\ D) \tag{7.16}$$

$$\Sigma_{US}\ BD = \left(\frac{B\ +\ D)}{2}\right) \tag{7.17}$$

$$\Sigma_S\ CD = (C\ +\ D) \tag{7.18}$$

$$\Sigma_{US}\ CD = \left(\frac{C\ +\ D)}{2}\right) \tag{7.19}$$

The different combinations of feed elements can be seen to squint the beam and alter the peak gain. To more easily see which combination gives the closest representation the difference from the Σ created from all 4 channels and the calculated Σ is shown in, Figs. 7.13 and 7.14. It can be seen the Σ_S AZ and EL cuts produced by the feed elements BC, calculated from Equation (7.14), gives a close representation of the ΣAZ and ΣEL cuts created with all 4 feed elements, Fig. 7.15. The RMS difference from the correct Σ

is 0.11 dB in both cases. This is equivalent to a feed element drop in gain of less than 0.5 dB. Therefore, to create a Σ cut from a four port monopulse feed with one failed feed element, the Σ should be created from the scaled value of the two feed elements adjacent to the failed feed element, Equation (7.20).

$$\Sigma_S \;=\; \Sigma \; adjacent \; channels \tag{7.20}$$

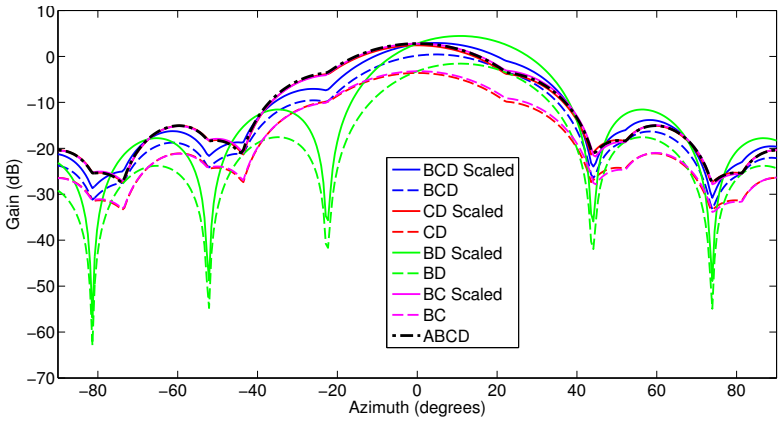

Figure 7.11: Simulated alternative methods to calculate the ΣAZ cut.

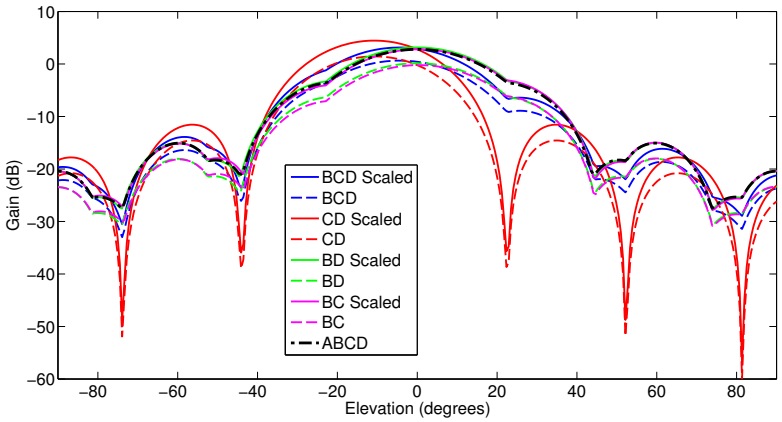

Figure 7.12: Simulated alternative methods to calculate the ΣEL cut.

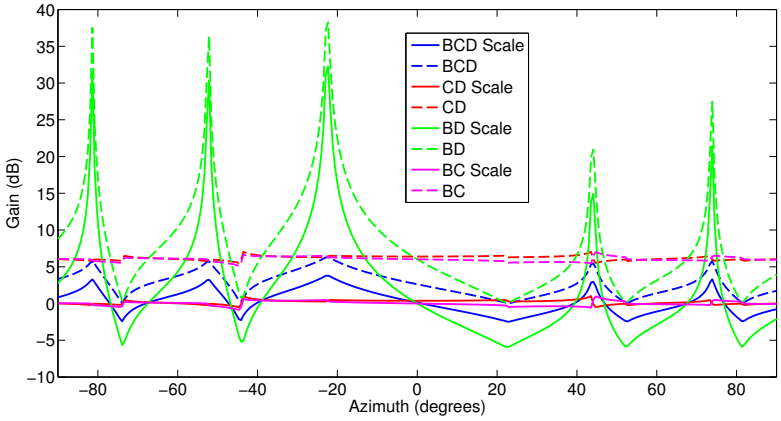

Figure 7.13: Simulated difference from the ΣAZ created with 4 channels and the alternative methods to calculate the ΣAZ cut.

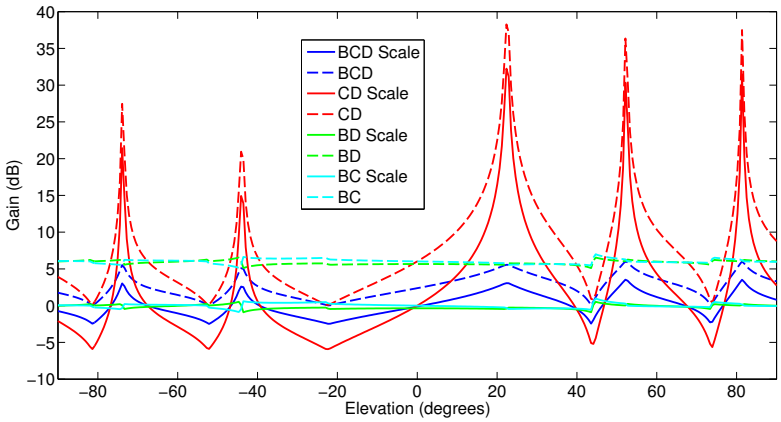

Figure 7.14: Simulated difference from the ΣEL created with 4 channels and the alternative methods to calculate the ΣEL cut.

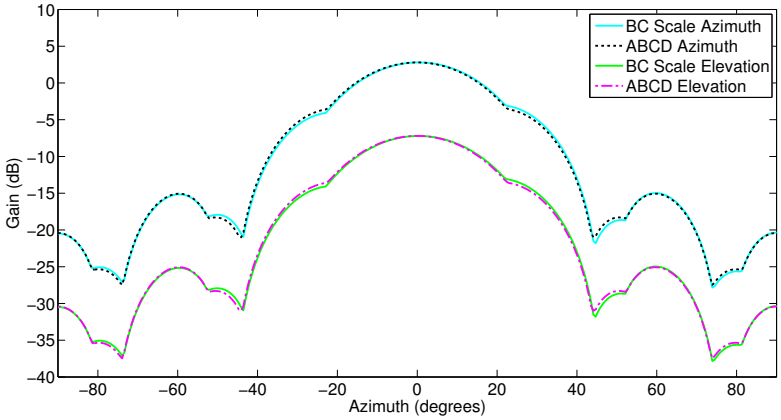

Figure 7.15: Best RMS method for ΣAZ and ΣEL shown with an offset of -10dB.

7.3.3 COMPENSATION FOR A FAILED FEED ELEMENT IN Δ

With a four port monopulse antenna there are multiple ways in which the Δ patterns can be produced if feed element A has failed. Δ is calculated from Equations (7.2) and (7.3). Potential permutations to calculate ΔAZ are shown in Equations (7.21) to (7.26). Potential permutations to calculate ΔEL are shown in Equations (7.27) to (7.32).

$$\Delta_S AZ\ BCD = \left(\frac{2C\ -\ (B\ +\ D)}{2}\right) \tag{7.21}$$

$$\Delta_{US} AZ\ BCD = \left(\frac{C\ -\ (B\ +\ D)}{2}\right) \tag{7.22}$$

$$\Delta_S AZ\ BC = (B\ -\ C) \tag{7.23}$$

$$\Delta AZ_{US}\ BC = \left(\frac{(B\ -\ C)}{2}\right) \tag{7.24}$$

$$\Delta_S AZ\ CD = (D\ -\ C) \tag{7.25}$$

$$\Delta_{US} AZ\ CD = \left(\frac{(D\ -\ C)}{2}\right) \tag{7.26}$$

$$\Delta_S EL\ BCD = \left(\frac{2B\ -\ (C\ +\ D)}{2}\right) \tag{7.27}$$

$$\Delta_{US} EL\ BCD = \left(\frac{B\ -\ (C\ +\ D)}{2}\right) \tag{7.28}$$

$$\Delta_S EL\ BC = (B\ -\ C) \tag{7.29}$$

$$\Delta_{US} EL\ BC = \left(\frac{(B\ -\ C)}{2}\right) \tag{7.30}$$

$$\Delta_S EL\ BD = (B\ -\ D) \tag{7.31}$$

$$\Delta_S EL\ BD = \left(\frac{(B\ -\ D)}{2}\right) \tag{7.32}$$

The different combinations of feed elements can be seen to squint the beam or cause a change in the gain, Figs. 7.16 and 7.17 for ΔAZ and ΔEl respectively.

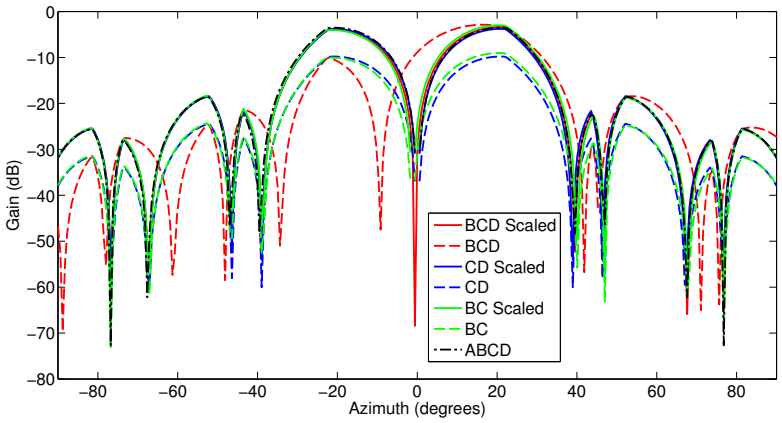

Figure 7.16: Simulated alternative methods to calculate the ΔAZ cut.

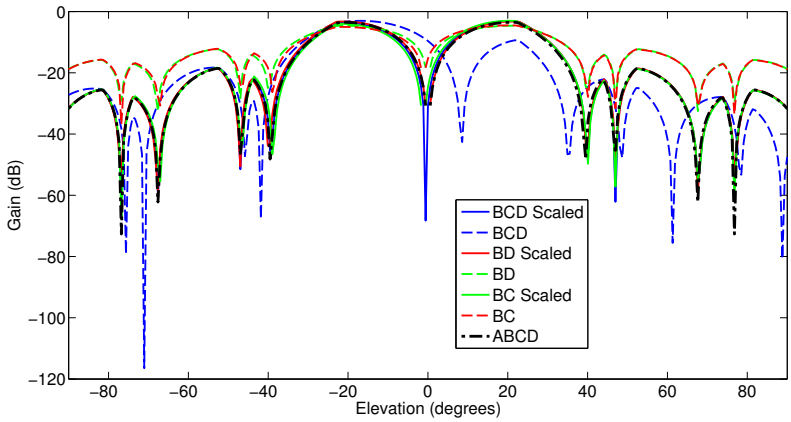

Figure 7.17: Simulated alternative methods to calculate the ΔEL cut.

To clearly see which combination gives the best representation the Δ from the value calculated using all 4 channels is plotted Figs. 7.18 and 7.19 for ΔAZ and ΔEl respectively.

The $\Delta_S AZ$ cuts produced by the feed elements CD, Equation (7.25), gives the closest representation of the ΔAZ cut created with all 4 feed elements, Fig. 7.20. The RMS difference is 0.24 dB. However, it can be seen that the $\Delta_S El$ cut produced by the feed elements BD, Equation (7.31), gives a very good representation of the ΔEl cut created with all 4 feed elements, Fig. 7.20, the RMS difference is 0.24 dB.

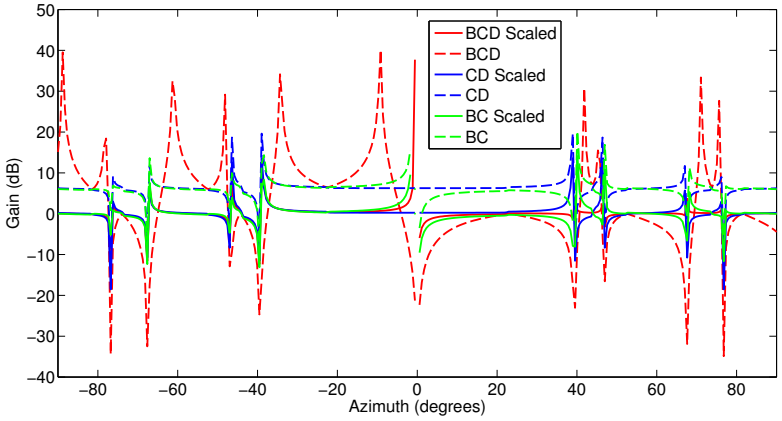

Figure 7.18: Simulated difference from the ΔAZ created with 4 channels and the alternative methods to calculate the ΔAZ cut.

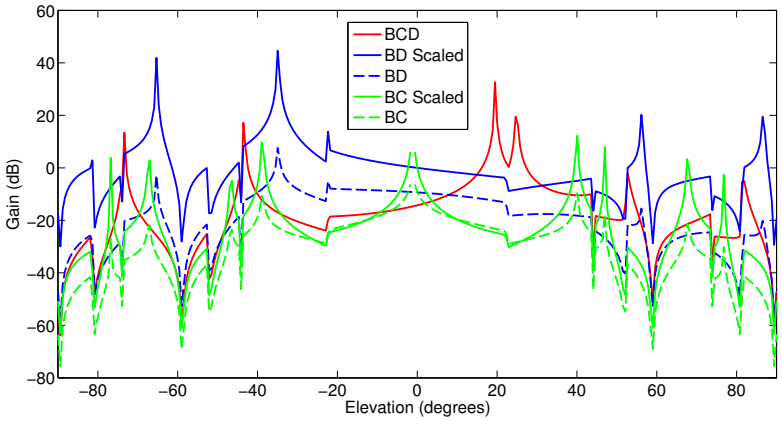

Figure 7.19: Simulated difference from the ΔEL created with 4 channels and the alternative methods to calculate the ΔEL cut.

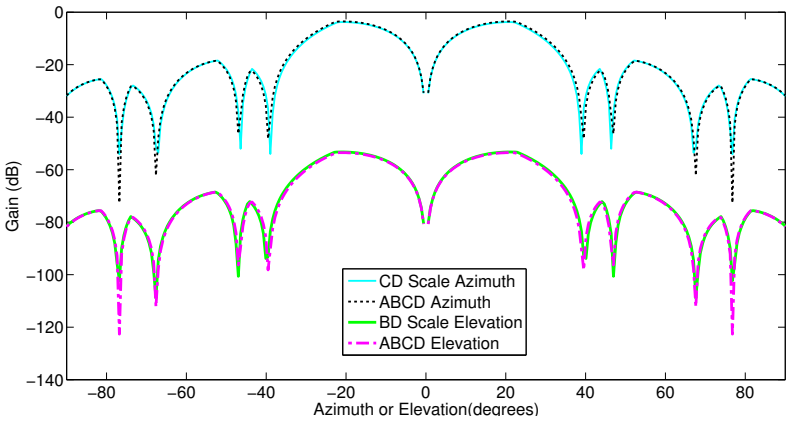

Figure 7.20: Simulated best RMS method for ΔAZ, ΔEL with a -10dB offset.

This is understandable as it allows creation of the Δ cuts without using the section of the monopulse horn that is damaged. Therefore, to create a Δ cut from a four port monopulse feed with one failed feed element, the Δ cut should be created from the scaled value of two feed elements, removing the failed feed element and its adjacent feed element in terms of the cut that is being taken, Equation (7.33).

$$\Delta_S = \Delta \; Channels \; Not \; Adjacent \; in \; Direction \; of \; Cut \tag{7.33}$$

7.4 COMPENSATION FOR A FAILED FEED ELEMENT AC TESTING

To prove the proposed method for compensation of a failed feed element, a TRMAS was tested in an AC. The chamber was calibrated for measuring a multi-channel antenna [38]. Fig. 7.21 shows that the radiation pattern produced by using Equations (7.1), (7.2), (7.20) and (7.33). The RMS error between the ΣAZ cut is 0.07 dB and the ΔAZ cut is 0.42 dB. Fig. 7.22 shows the section over which the RMS error is calculated.

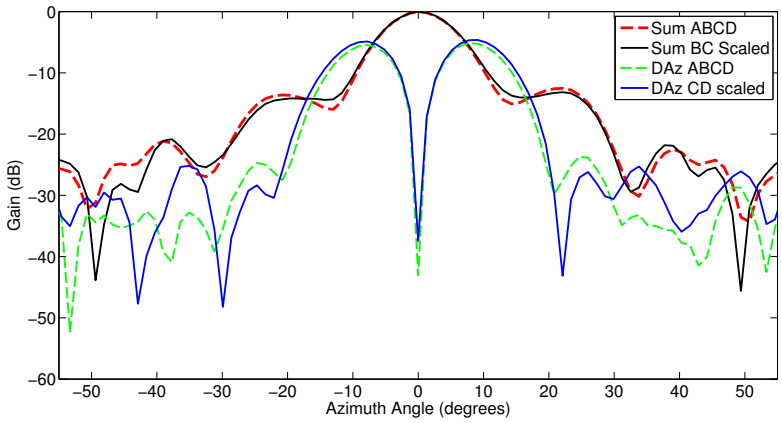

Figure 7.21: Measured ΣAZ and ΔAZ with and without a failed feed element.

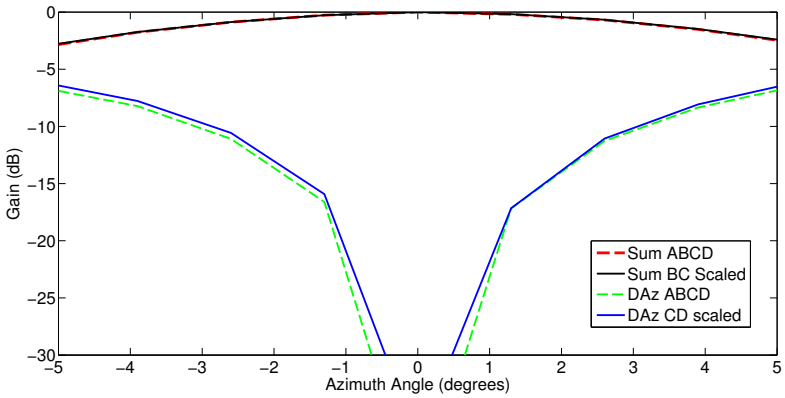

Figure 7.22: Reduced scale measured ΣAZ and ΔAZ with and without failed feed element.

Fig. 7.23 shows that the radiation pattern produced using Equations (7.1), (7.3), (7.20) and (7.33). The RMS error between the ΣEL cut is 0.06 dB and the ΔEL cut is 0.69 dB. Fig. 7.24 shows the section over which the RMS error is calculated.

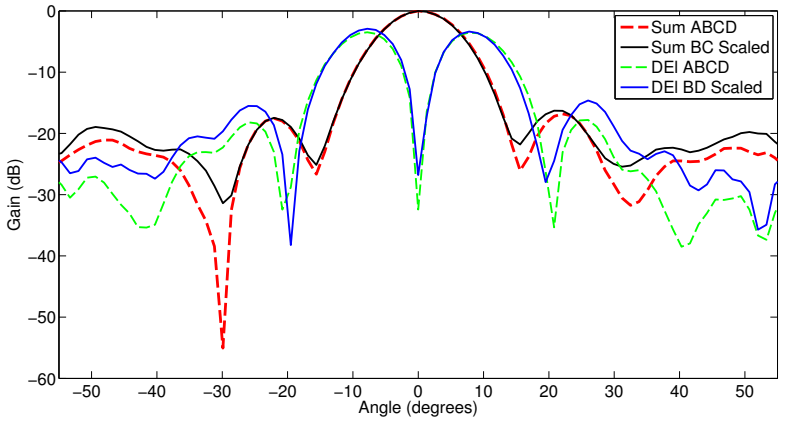

Figure 7.23: Measured ΣEL and ΔEL with and without a failed feed element.

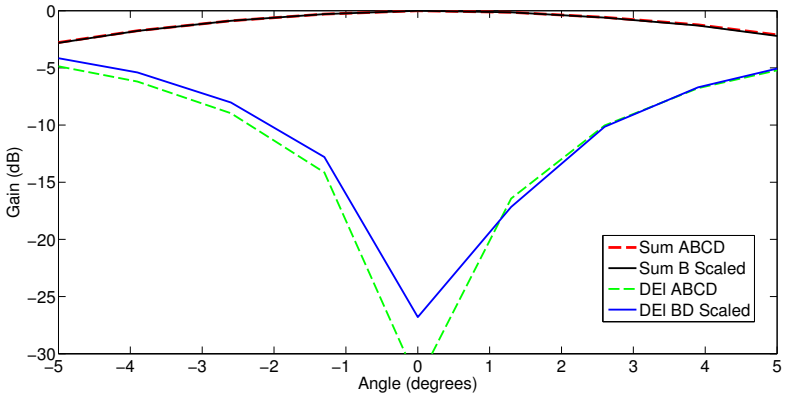

Figure 7.24: Reduced scale measured ΣEL and ΔEL with and without failed feed element.

The results are summarised in Table 7-B. These differences are the same as those found on repeat measurements with the same hardware set up, i.e. they are at the measurement error level, therefore validating this procedure for creating the Σ and Δ signals from the feed element data.

CUT PERFORMED	**RMS DIFFERENCE BETWEEN SDC AND COMPENSATION SUMMATION (dB)**
ΣAZ	0.07
ΣEL	0.06
ΔAZ	0.42
ΔEL	0.69

Table 7-B: RMS difference between SDC and compensation for a failed feed element summed Σ and Δ pattern.

Fig. 7.25 shows that the gain as a function of frequency produced by summing 4 channels as described in Equation (2.5) and 3 channels as described in Equation (7.14) show excellent overlay. The RMS error difference between the Σ was calculated to be 0.06 dB and the maximum difference 0.19 dB. Again, this is at the level of repeat measurements in the AC.

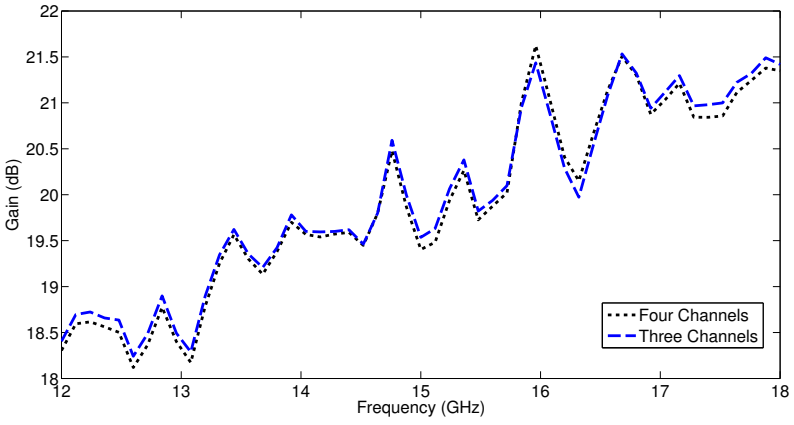

Figure 7.25: Measured gain as a function of frequency for a TRMAS formed with a comparator and by SDC from raw feed element data.

7.5 MULTIPLE FAILED FEED ELEMENTS

Although the work contained in this chapter has focused on the failure of a single feed element, because all permutations of feed elements have been investigated the results actually give information on multiple failed feed elements, as shown in Table 7-C.

If diagonal feed elements fail the ΣAZ and EL can be recovered, as shown in Figs. 7.11 and 7.12, the RMS difference between this signal and one created from all four feed elements is 0.11 dB. The ΔAZ and EL can be recovered to a lesser level, as shown in Figs. 7.16 and 7.17, the RMS difference is 1.90 dB. This difference results in a shift in the Δ null of -0.57^o, which may be a tolerable error to allow the system to continue to function.

However, if either horizontal or vertical adjacent feed elements fail only one Σ and one Δ signal can be successfully re-created. Therefore this would render the system inoperative.

FAILED FEED ELEMENTS	**WORKING FEED ELEMENTS**	**ΣAZ RMS** (dB)	**ΣEL RMS** (dB)	**ΔAZ RMS** (dB)	**ΔEL RMS** (dB)
AD	BC	0.11	0.11	1.90	1.90
AC	BD	5.07	0.38	not possible	0.23
AB	CD	0.40	5.07	0.24	not possible

Table 7-C: Recoverable signals using combinations of feed elements in terms of RMS difference from the signal calculated using all feed elements.

7.6 SUMMARY

This chapter has provided a derivation and tested a method to construct the Σ and Δ cuts from a TRMAS in software negating the use of a hardware comparator. This has been compared to measurements taken with and without a comparator, both in terms of pattern and gain, and has been validated as a viable method.

It has been demonstrated that the mathematical approach presented allows the monopulse antenna system to work if one of the channels has been damaged. This work has been extended to show that the system may still be able to operate if two diagonally opposite feed elements fail. This would normally mean that the whole antenna system would fail to operate, however by applying the equations derived and shown here the antenna will continue to be able to function.

Patent application number GB1505562.7 has been filed in the name of MBDA UK Ltd in relation to aspects of the material described in this chapter.

The next chapter details the conclusions of the improved hardware test of a TRMAS and the design improvement of a TRMAS discussed in this thesis.

Chapter 8

CONCLUSIONS AND FURTHER WORK

8.1 MAIN CONTRIBUTIONS OF THESIS

The main contributions of this thesis are summarised below:

- Definition of an accurate anechoic chamber calibration procedure for measurement of a twist reflector monopulse antenna system.
- Definition of a measurement technique to perform phase stable measurements of a twist reflector monopulse antenna system.
- Derivation, simulation and hardware confirmation of an axis transform to accurately measure a twist reflector monopulse antenna system and radome system on a 3 axis positioner.
- Through theoretical modelling and experimental testing the grid line depth of a polarisation selection grid is required to be at minimum 30 times the skin depth for the polarisation selection grid to function at the -25 dB level.
- Derivation of a new method to accurately calculate the optimised thickness of a radome for minimum transmission loss reducing time overheads by 3 orders of magnitude.
- Successful recovery of sum and difference patterns if one feed element of the twist reflector monopulse antenna system fails.

A novel extension to current AC calibration process and best technique for phase stable measurements are presented. The new calibration process and measurement procedures are shown to be suitable for multi-channel antenna systems. Therefore the work included in this thesis allows for the correct measurement procedure for a TRMAS, verified by hardware measurements.

The derivation of an AT for a 3 axis positioner has been presented. It has been verified by simulation and hardware test that the cuts produced are in the true T frame and are suitable for testing a TRMAS, i.e. the $\Delta AZ/\Sigma$ has been shown to reduce to 0.

The optimisation of a PSG has been conducted in full field simulations and hardware test. To manufacture a functioning PSG from a metal deposition process it has been found that the *GLD* has to be 30 times the skin depth for the PSG to function at the -25 dB cross-polar isolation level. This is contrary to current understanding, where 5 times the skin depth was thought to be sufficient.

A new method to optimise the thickness of a radome for a TRMAS has been presented, which reduces the time overhead by 3 orders of magnitude and the computer memory by 2 orders of magnitude from using a full EM simulation for thickness calculation without compromising accuracy. By using a combination of a custom written 2DRTM code and a HFSS unit cell simulation the thickness of the radome can be optimised to be the same as using a full TRMAS and radome HFSS simulation. The resultant thickness of this work has been verified by AC measurement.

Removal of the comparator has been verified, thus allowing advantages of lower size and mass requirements. Digital monopulse enables further processing of the raw signals. Equations have been presented to demonstrate that with the removal of the comparator the TRMAS is still able to function if one of the feed elements has been damaged.

8.2 FURTHER WORK

Further improvements may be implemented to the hardware test processes.

Additional hardware can be designed and manufactured to aid the accuracy of the calibration procedure. Rather than a single cable being used as the calibration path between the SGH and the hardware test set up for TRMAS testing a series of RF splitters could be used. This would enable the use of semi-rigid coaxial cables, so test hardware would be developed that did not have to be moved between each channel measurement thus removing errors due to cable connection and disconnection. This would also reduce the calibration process time from 1 hour to 20 minutes.

If more accuracy is required for the TRMAS measurement then a further addition to the AT could be included from the findings of [88] which describes how the fields are reflected from a twist reflector. However, as shown the procedure in this thesis leaves a small error of $\Delta AZ/\Sigma = 0.178$ at maximum, so gains from this addition to the AT would therefore be small.

Further work may be carried out on the optimisation of the composite parts of a TRMAS.

To further improve the performance of the PSG the surface finish and edge definition of the GL could be investigated. These are functions of the metal deposition and GL manufacture process. It is clear that these will have an effect on the reflectivity of the metal and its performance as a PSG. Simulations could be constructed to assess the impact, but the impact of these defects is not thought to be significant as deviations are less than $\lambda/32$. Looking to the future it may be possible to manufacture the entire PSG using rapid prototype technologies.

Often with composite radomes, which are produced on a male mould tool the outside of the radome is machined to shape, the machined surfaces have to be sealed to prevent moisture ingress. This sealing layer may have an impact on the RF performance of the unit. If the thickness and RF properties of the sealing layer material are known they can be added into the HFSS unit cell model so its impact on the performance of the radome will be taken into account in the design stage. The impact of such a thin layer of resin

(approximately 0.5 mm) is not expected to have a significant effect as it is less than $\lambda/32$. It is more likely that the material that could build up on the external surface of the radome would be influential on the RF performance and could be investigated [89].

The simulations could be extended to look at producing a variable thickness [56] or variable dielectric constant [53] radome.

In the software combination of signals to form a monopulse beam if adjacent feed elements fail then you would only be able to recover the AZ or EL position in one measurement. Therefore a failure mechanism that allowed two signals to be analysed, with a small movement between them, may allow the TRMAS to continue functioning. With digital monopulse it is possible recover and analyse the phase of the feed elements, which will give beam squint information.

8.3 PUBLISHED PAPERS AND PATENTS

PUBLISHED	PUBLICATION	TITLE	AUTHORS
2016	Institute of Engineering and Technology, Microwaves, Antennas and Propagation	Efficient Design of a Radome for Minimised Transmission Loss	T. L. Sheret C. G. Parini B. Allen
2016	European Conference on Antennas and Propagation	Phase Stable Multi-Channel Antenna Measurements on a Moving Positioner	T. L. Sheret B. Allen C. G. Parini
2016	Institute of Engineering and Technology, Microwaves, Antennas and Propagation	Monopulse Sum and Difference Signals with Compensation for a Failed Feed Element	T. L. Sheret B. Allen C. G. Parini
2015	GP Patent GB1505562.7	Resilient Sum and Difference Signals	T. L. Sheret
2014	Automated RF and Microwave Measurement Society Conference	Calibration of an Anechoic Chamber for Measurement of a Multi-Channel Antenna	T. L. Sheret B. Allen
2014	Loughborough Antenna and Propagation Conference	Axis Transform to Characterise a Monopulse Twist Reflector Antenna and Radome in an Anechoic Chamber	T. L. Sheret B. Allen
2013	Applied Radio Systems Research - Smart Wireless Communications Conference	Simulation and Measurement of the Effect of Track Thickness for the Design of a PSG	T. L. Sheret B. Allen B. Gilhespy

Table 8-A: Published papers and patents.

BIBLIOGRAPHY

[1] Y. Rahmat-Samii and R. Haupt, "Reflector antenna developments: A perspective on the past, present and future," *IEEE Antennas and Propagation Magazine*, vol. 57, no. 2, pp. 85–95, April 2015.

[2] P. Hannan, "Microwave antennas derived from the cassegrain telescope," *Antennas and Propagation, IRE Transactions on*, vol. 9, no. 2, pp. 140–153, 1961.

[3] R. Martin and L. Schwartzman, "A monopulse cassegrainian antenna," in *IRE International Convention Record*, vol. 8, 1960, pp. 96–102.

[4] P. Wood, *Reflector Antenna Analysis and Design*, ser. IEE Electromagnetic Waves Series. Peter Peregrinus Press, 1980. [Online]. Available: http://books.google.co.uk/books?id=0CgIAQAAIAAJ

[5] O. Dahlsjo, "Antenna research and development at ericsson," *Antennas and Propagation Magazine, IEEE*, vol. 34, no. 2, pp. 7–17, April 1992.

[6] L. Josefsson, "A broad-band twist reflector," *Antennas and Propagation, IEEE Transactions on*, vol. 19, no. 4, pp. 552–554, 1971.

[7] D. Howard and D. Cross, "Mirror antenna dual-band lightweight mirror design," *Antennas and Propagation, IEEE Transactions on*, vol. 33, no. 3, pp. 286–294, 1985.

[8] Y. T. Lo and S. W. Lee, *Antenna Handbook: Theory, Applications, and Design.*

[9] T. L. Sheret, B. Allen, and B. Gilhespy, "Simulation and measurement of the effect of track thickness for the design of a polarisation selective grid," in *3rd Conference on Applied Radio Systems Research and Smart Wireless Communicatins*, 2013, pp. 1–4.

[10] J. Hanfling, G. Jerinic, and L. Lewis, "Twist reflector design using e-type and h-type modes," *Antennas and Propagation, IEEE Transactions on*, vol. 29, no. 4, pp. 622–629, 1981.

[11] K. Hwang, "Optimisation of broadband twist reflector for ku-band application," *Electronics Letters*, vol. 44, no. 3, pp. 210–211, 2008.

[12] S. S. H. Naqvi and N. C. Gallagher, "Analysis of a strip-grating twist reflector," *Journal of the Optical Society of America*, vol. 7, no. 9, pp. 1723–1729, 1990.

[13] W. Gregorwich, "Polarization selective reflectors for spacecraft applications," in *Aerospace Applications Conference, 1990. Digest., 1990 IEEE*, feb 1990, pp. 61 –71.

[14] E. Garcia, C. Delgado, I. Gonzalez, J. Almagro, K. van 't Klooster, and F. Catedra, "Analizing large reflectors antennas built with complex knitted meshes," in *Antennas and Propagation (APSURSI), 2011 IEEE International Symposium on*, July 2011, pp. 934–937.

[15] J. Lecourtier, "Signal-channel evaluation network for monopulse radar receiver," Patent US 3 560 974, 02 02, 1971.

[16] B. Mahafza, *Introduction to Radar Analysis*, ser. Electrical Engineering Radar Signal Processing. Taylor & Francis, 1998. [Online]. Available: https://books.google.co.uk/books?id=HnbERplIrX0C

[17] K. Lee and R.-S. Chu, "Design and analysis of a multimode feed horn for a monopulse feed," *Antennas and Propagation, IEEE Transactions on*, vol. 36, no. 2, pp. 171–181, 1988.

[18] S. M. Sherman, "Monopulse principles and techniques, artech house," *Inc., Dedham, MA*, 1984.

[19] Y. K. Singh and A. Chakrabarty, "Design and sensitivity analysis of highly compact comparator for ku-band monopulse radar," in *Radar Symposium, 2006. IRS 2006. International*, 2006, pp. 1–4.

[20] H. Kumar, G. Kumar, Y. Verma, and P. K. Mishra, "Compact waveguide monopulse comparator at ka-band for monopulse tracking," in *2016 IEEE International Symposium on Antennas and Propagation (APSURSI)*, June 2016, pp. 1357–1358.

[21] S. Cornbleet, "Monopulse combining network," *Electronics Letters*, vol. 1, no. 6, pp. 158–, 1965.

[22] L. Z. You and W. Dou, "Design and optimization of planar waveguide magic tee at w-band," in *Microwave and Millimeter Wave Technology, 2007. ICMMT '07. International Conference on*, 2007, pp. 1–4.

[23] A. Rudge, *The Handbook of antenna design*, ser. IEE electromagnetic waves series. P. Peregrinus on behalf of the Institution of Electrical Engineers, 1983, no. v. 2.

[24] A. Renuka and V. Borkar, "Computer-aided analysis for tangent ogive airborne radome using physical optics method," in *Microwave Conference Proceedings, 2005. APMC 2005. Asia-Pacific Conference Proceedings*, vol. 5, Dec 2005, pp. 4 pp.–.

[25] C. Kuan-Kim, C. Po-Rong, and H. Fang, "Radome design by simulated annealing technique," in *Antennas and Propagation Society International Symposium, 1992. AP-S. 1992 Digest. Held in Conjuction with: URSI Radio Science Meeting and Nuclear EMP Meeting., IEEE*, 1992, pp. 1401–1404 vol.3.

[26] E. L. Fleeman, "Technologies for future precision strike missile systems," *NATO Lecture Series*, vol. 221, 2001.

[27] C. G. Parini, S. Gregson, J. McCormick, and D. J. van Rensburg, *Theory and Practice of Modern Antenna Range Measurements.*

[28] W. H. Emerson, "Anechoic chamber," Patent US 3 308 463, 03 07, 1967.

[29] W. H. Emerson, "Emerson anechoic chamber," Patent US 3 273 150, 09 13, 1966.

[30] Health and S. Executive, "Electromagnetic fields at work: A guide to the Control of Electromagnetic Fields at Work Regulations 2016," *Health and Safety Executive*, 2016.

[31] B. K. Chung and H. T. Chuah, "Modeling of rf absorber for application in the design of anechoic chambertechnologies for future precision strike missile systems," *Progress In Electromagnetics Research*, vol. 43, pp. 273–285, 2003.

[32] T. Sheret and B. Allen, "Axis transform to characterise a monopulse twist reflector antenna and radome in an anechoic chamber," in *Antennas and Propagation Conference (LAPC), 2014 Loughborough*, Nov 2014, pp. 612–616.

[33] M. Gillette, "Rf anechoic chamber design using ray tracing," in *Antennas and Propagation Society International Symposium, 1977*, vol. 15, 1977, pp. 246–249.

[34] M. Barron, "Specifying and procuring a 10 meter semi-anechoic emc chamber," in *Electromagnetic Compatibility, 2000. IEEE International Symposium on*, vol. 1, 2000, pp. 231–236 vol.1.

[35] Institute of Electrical and Electronics Engineers. Antenna Standards Committee, *IEEE standard test procedures for antennas*, ser. Ieeee Std 149-1979 Series. Institute of Electrical and Electronics Engineers : distributed in cooperation with Wiley-Interscience, 1979.

[36] A. Yaghjian, "An overview of near-field antenna measurements," *Antennas and Propagation, IEEE Transactions on*, vol. 34, no. 1, pp. 30–45, Jan 1986.

[37] EMSCAN Corpration, *RFxpert Training Manual*, 2012. [Online]. Available: http://www.emcan.com/downloads/RFxpert/Technical_Resources/RFxpert_Training_Manual.pdf

[38] T. L. Sheret and B. Allen, "Calibration of an anechoic chamber for measurement of a multi-channel antenna," in *Automated RF and Microwave Measurement Society*, 2014. [Online]. Available: http://www.armms.org/conference/?conference=60

[39] T. L. Sheret, B. Allen, and C. G. Parini, "Phase stable multi-channel antenna measurements on a moving positioner," in *European Conference on Antenna and Propagation*, 2016, pp. 1–4.

[40] G. R. Grado, "A solution to the euler angle transformation equations," *Electronic Computers, IRE Transactions on*, vol. EC-9, no. 3, pp. 362–369, Sept 1960.

[41] P. Clarricoats, C. Parini, and M. Rizk, "Novel radome design for reduced return-loss," in *Antennas and Propagation Society International Symposium, 1982*, vol. 20, May 1982, pp. 112–115.

[42] H. Burger, "Use of euler-rotation angles for generating antenna patterns," *Antennas and Propagation Magazine, IEEE*, vol. 37, no. 2, pp. 56–63, Apr 1995.

[43] T. Milligan, "More applications of euler rotation angles," *Antennas and Propagation Magazine, IEEE*, vol. 41, no. 4, pp. 78–83, Sep 1999.

[44] W. Mumford, "Some technical aspects of microwave radiation hazards," *Proceedings of the IRE*, vol. 49, no. 2, pp. 427–447, 1961.

[45] R. Neri and T. Maclean, "Receiving and transmitting properties of small grid paraboloid by moment method," *Electrical Engineers, Proceedings of the Institution of*, vol. 126, no. 12, pp. 1209 –1219, december 1979.

[46] C. Dragone, "New grids for improved polarization diplexing of microwaves in reflector antennas," *Antennas and Propagation, IEEE Transactions on*, vol. 26, no. 3, pp. 459 – 463, may 1978.

[47] M.-C. Wu, C.-P. Chiu, and S.-J. Chung, "Development of a novel 38.5 ghz planar cassegrain antenna," in *Microwave Conference, 2001. APMC 2001. 2001 Asia-Pacific*, vol. 3, 2001, pp. 1366 –1369 vol.3.

[48] K. Nakamura and M. Ando, "A full-wave analysis of offset reflector antennas with polarization grids," *Antennas and Propagation, IEEE Transactions on*, vol. 36, no. 2, pp. 164 –170, feb 1988.

[49] G. Brooker, "Development of a w-band scanning conscan antenna based on the twist-reflector concept," in *Microwave and Millimeter Wave Technology, 2000, 2nd International Conference on. ICMMT 2000*, 2000, pp. 436–439.

[50] P. F. Mariner, "Lens, mirror or like elements for high frequency radio aerials," Patent US 2 900 706, 08 25, 1959.

[51] L. Li, M. Leong, I. Zhou, T. Yeo, and P. Kooi, "Improved analysis of antenna radiation from a circular aperture covered by a dielectric hemispherical radome shell," *Microwaves, Antennas and Propagation, IEE Proceedings*, vol. 147, no. 2, pp. 144–150, Apr 2000.

[52] J. Wang, G. Guo, H. Zheng, and E. Li, "Characteristic analysis of nose radome by aperture-integration and surface-integration method," in *Microwave and Millimeter Wave Circuits and System Technology (MMWCST), 2012 International Workshop on*, April 2012, pp. 1–4.

[53] R. Nair, M. Suprava, and R. Jha, "Graded dielectric inhomogeneous streamlined radome for airborne applications," *Electronics Letters*, vol. 51, no. 11, pp. 862–863, 2015.

[54] MATLAB, *version 8.1 (R2013a)*. Natick, Massachusetts: The MathWorks Inc., 2013.

[55] HFSS, "Version 13.0.2," *Ansoft Corporation LLC, 22 West Station, Square Suite 200, Pittsburgh, PA*, pp. 15 219–1119, 2011.

[56] R. Nair and R. Jha, "Electromagnetic performance analysis of a novel monolithic radome for airborne applications," *Antennas and Propagation, IEEE Transactions on*, vol. 57, no. 11, pp. 3664–3668, Nov 2009.

[57] K. Chang, "Antenna angle error correction to radome curvature," in *Antennas and Propagation Society International Symposium, 1995. AP-S. Digest*, vol. 3, June 1995, pp. 1426–1429 vol.3.

[58] C. Gibson, M. Bonebright, and S. Weisbrod, "Design of an 89 ghz radome," in *Radar Conference, 1998. RADARCON 98. Proceedings of the 1998 IEEE*, 1998, pp. 373–378.

[59] R. Johnson and H. Jasik, *Antenna Engineering Handbook*, ser. Electronics: Electrical engineering. McGraw-Hill Professional Publishing, 1993. [Online]. Available: http://books.google.co.uk/books?id=xTSNJhVlHGgC

[60] W. Qureshi, L. Hill, M. Scott, and R. Lewis, "Use of a gaussian beam range and reflectivity arch for characterisation of radome panels for a naval application," in *Antennas and Propagation, 2003. (ICAP 2003). Twelfth International Conference on (Conf. Publ. No. 491)*, vol. 1, March 2003, pp. 405–408 vol.1.

[61] B. Audone, A. Delogu, and P. Moriondo, "Radome design and measurements," *Instrumentation and Measurement, IEEE Transactions on*, vol. 37, no. 2, pp. 292–295, 1988.

[62] T. L. Sheret, C. G. Parini, and B. Allen, "Efficient design of a radome for minimised transmission loss," in *IET Microwaves, Antennas And Propagation*, 2016, pp. 1–4.

[63] T. Sheret, C. Parini, and B. Allen, "Monopulse sum and difference signals with compensation for a failed feed element," *IET Microwaves, Antennas Propagation*, vol. 10, no. 6, pp. 645–650, 2016.

[64] A. Morabito and P. Rocca, "Optimal synthesis of sum and difference patterns with arbitrary sidelobes subject to common excitations constraints," *Antennas and Wireless Propagation Letters, IEEE*, vol. 9, pp. 623–626, 2010.

[65] R. Mailloux, "Array failure correction with a digitally beamformed array," *Antennas and Propagation, IEEE Transactions on*, vol. 44, no. 12, pp. 1543–1550, Dec 1996.

[66] W. Keizer, "Element failure correction for a large monopulse phased array antenna with active amplitude weighting," *Antennas and Propagation, IEEE Transactions on*, vol. 55, no. 8, pp. 2211–2218, Aug 2007.

[67] O. Bucci, T. Isernia, and A. Morabito, "An effective deterministic procedure for the synthesis of shaped beams by means of uniform-amplitude linear sparse arrays," *Antennas and Propagation, IEEE Transactions on*, vol. 61, no. 1, pp. 169–175, Jan 2013.

[68] G. Oliveri, P. Rocca, and A. Massa, "Reliable diagnosis of large linear arrays - a bayesian compressive sensing approach," *Antennas and Propagation, IEEE Transactions on*, vol. 60, no. 10, pp. 4627–4636, Oct 2012.

[69] N. Anselmi, L. Manica, P. Rocca, and A. Massa, "Tolerance analysis of reconfigurable monopulse linear antenna arrays using interval arithmetic," in *Antennas and Propagation (EuCAP), 2014 8th European Conference on*, April 2014, pp. 1509–1512.

[70] D. Y. Huang and K. Boyle, *Antennas: From Theory to Practice*. Wiley, 2008.

[71] T. Teshirogi and T. Yoneyama, *Modern Millimeter-wave Technologies*, ser. Wave Summit Series. Ohmsha, 2001.

[72] G. Hejc, W. Schafer, A. Seidel, M.-P. Hess, J. Kehrer, and G. Santarelli, "Frequency dependency of phase stability of rf cables," in *Frequency Control Symposium, 2007 Joint with the 21st European Frequency and Time Forum. IEEE International*, May 2007, pp. 1309–1311.

[73] J. Hollis, T. Lyon, and L. Clayton, *Microwave Antenna Measurements.* Scientific-Atlanta, 1985. [Online]. Available: https://books.google.co.uk/books?id=MJm3cQAACAAJ

[74] G. Piovan and F. Bullo, "On coordinate-free rotation decomposition: Euler angles about arbitrary axes," *Robotics, IEEE Transactions on*, vol. 28, no. 3, pp. 728–733, June 2012.

[75] R. L. Pio, "Euler angle transformations," *Automatic Control, IEEE Transactions on*, vol. 11, no. 4, pp. 707–715, Oct 1966.

[76] I.-Y. Tarn, Y.-S. Wang, and S.-J. Chung, "A dual-mode millimeter-wave folded microstrip reflectarray antenna," *Antennas and Propagation, IEEE Transactions on*, vol. 56, no. 6, pp. 1510 –1517, june 2008.

[77] M. Ando and K. Takei, "Reflection and transmission coefficients of a thin strip grating for antenna application," *Antennas and Propagation, IEEE Transactions on*, vol. 35, no. 4, pp. 367 – 371, apr 1987.

[78] R. Scharstein, "Mutual coupling in a slotted phased array, infinite in e-plane and finite in h-plane," *Antennas and Propagation, IEEE Transactions on*, vol. 38, no. 8, pp. 1186–1191, 1990.

[79] M. Inam, M. Ismail, A. Zain, and M. Mughal, "Analysis of reflectarrays printed above variable substrate thicknesses," in *Applied Electromagnetics (APACE), 2010 IEEE Asia-Pacific Conference on*, nov. 2010, pp. 1 –4.

[80] H. Wheeler, "Formulas for the skin effect," *Proceedings of the IRE*, vol. 30, no. 9, pp. 412–424, 1942.

[81] S. Wentworth, M. Baginski, D. Faircloth, S. Rao, and L. Riggs, "Calculating effective skin depth for thin conductive sheets," in *Antennas and Propagation Society International Symposium 2006, IEEE*, july 2006, pp. 4845 –4848.

[82] R. Maaskant, D. J. Bekers, M. J. Arts, W. A. van Cappellen, and M. V. Ivashina, "Evaluation of the radiation efficiency and the noise temperature of low-loss antennas," *IEEE Antennas and Wireless Propagation Letters*, vol. 8, pp. 1166–1170, 2009.

[83] P. S. Heckbert, "derivation of refraction formulas," *Academic Press*, 1989.

[84] R. Schoenberg, "Optimization with the quasi-newton method," *Aptech Systems*, 2001.

[85] P. J. B. Clarricoats and R. Elliot, "Multimode corrugated waveguide feed for monopulse radar," *Microwaves, Optics and Antennas, IEE Proceedings H*, vol. 128, no. 2, pp. 102–110, 1981.

[86] Z.-W. Yu, G.-M. Wang, and C. xin Zhang, "A broadband planar monopulse antenna array of c-band," *Antennas and Wireless Propagation Letters, IEEE*, vol. 8, pp. 1325–1328, 2009.

[87] S. J. Orfanidis, *Electromagnetic waves and antennas*, ser. New Brunswick, NJ: Rutgers University, 2014.

[88] V. Borkar, R. Ethiraj, and V. Pandharipande, "Reflected fields from twist reflector in twist reflector scanning antenna configuration," *Electronics Letters*, vol. 29, no. 16, pp. 1397 –1398, aug. 1993.

[89] H. Burger, "Calculating the effects of non-uniform ice accumulation on radome performance by ray trace analysis," in *Antennas and Propagation (APSURSI), 2011 IEEE International Symposium on*, July 2011, pp. 313–316.